Department of Applied Physics

Large scattering lengths and long-range interactions in ultracold atomic gases

Risto Sarjonen

Aalto University

DOCTORAL DISSERTATIONS

Aalto University publication series
DOCTORAL DISSERTATIONS 34/2015

Large scattering lengths and long-range interactions in ultracold atomic gases

Risto Sarjonen

A doctoral dissertation completed for the degree of Doctor of Science (Technology) to be defended, with the permission of the Aalto University School of Science, at a public examination held at the lecture hall Y124 of the school on 27th March 2015 at 12 o'clock.

Aalto University
School of Science
Department of Applied Physics
Quantum Dynamics

Supervising professor
Prof. Päivi Törmä

Thesis advisor
Prof. Päivi Törmä

Preliminary examiners
Dr. Francesco Massel, University of Jyväskylä, Finland
Prof. Jonas Larson, University of Stockholm, Sweden

Opponent
Prof. Thomas Busch, OIST Graduate University, Japan

Aalto University publication series
DOCTORAL DISSERTATIONS 34/2015

ISBN 978-952-60-6121-4 (printed)
ISBN 978-952-60-6122-1 (pdf)
ISSN-L 1799-4934
ISSN 1799-4934 (printed)
ISSN 1799-4942 (pdf)
http://urn.fi/URN:ISBN:978-952-60-6122-1

Unigrafia Oy
Helsinki 2015

Finland

441 697
Printed matter

Author
Risto Sarjonen

Name of the doctoral dissertation
Large scattering lengths and long-range interactions in ultracold atomic gases

Publisher School of Science

Unit Department of Applied Physics

Series Aalto University publication series DOCTORAL DISSERTATIONS 34/2015

Field of research Computational Physics

Manuscript submitted 9 January 2015 **Date of the defence** 27 March 2015

Permission to publish granted (date) 24 February 2015 **Language** English

☐ **Monograph** ☒ **Article dissertation (summary + original articles)**

Abstract

This thesis studies bosonic and fermionic quantum gases. In the first part, a variational many-body theory is used to explain a Bragg scattering experiment carried out on a bosonic quantum gas [S.B. Papp et al. Bragg Spectroscopy of a Strongly Interacting ^{85}Rb Bose-Einstein Condensate. *Phys. Rev. Lett. 101, 135301 (2008)*]. A key feature in the experiment was the use of a Feshbach resonance, which made large values of the scattering length accessible. Due to the large values of the scattering length, existing models such as the Beliaev model could not be used to explain the observations, and therefore the experiment was a particularly interesting one to analyze. In our first approach, we constructed ad hoc potentials that fitted the observed excitation spectrum, and later we improved our approach by using T-matrix formalism to describe the Feshbach resonant system. All in all, the phenomenological model we developed fits the observed excitation spectrum and yields correct molecular Feshbach resonance state energies in certain cases.

The second part of this thesis studies fermionic quantum gases. We focus on studying a gas of spin-1/2 particles confined to a spin-dependent optical lattice. The lattice geometry is such that the up-spin component is loaded in a honeycomb lattice, and the down-spin component is confined to the underlying triangular lattice. We considered attractive on-site and nearest-neighbor interactions, and formulated the nearest-neighbor interaction term in such a way that it takes into account the possibility of spontaneous time-reversal symmetry breaking. Furthermore, we took into account the possibility of Fulde-Ferrell-Larkin-Ovchinnikov (FFLO) phase, which breaks spatial symmetry. Within a mean-field approximation, we showed that the FFLO state is the ground state of the system in many instances. In addition, we found out that the system spontaneously breaks time-reversal symmetry if the nearest-neighbor interaction strength is large. Due to the time-reversal symmetry breaking, the system has topologically non-trivial phases characterized by nonzero Chern numbers. Finally, there were also cases where the time-reversal symmetry was broken in the FFLO phase, and thus we found a phase where spatial and time-reversal symmetries are simultaneously broken.

Keywords quantum gases, Bose-Einstein condensate, Feshbach resonance, optical lattice, superfluidity, FFLO, topological phases

ISBN (printed) 978-952-60-6121-4 **ISBN (pdf)** 978-952-60-6122-1

ISSN-L 1799-4934 **ISSN (printed)** 1799-4934 **ISSN (pdf)** 1799-4942

Location of publisher Helsinki **Location of printing** Helsinki **Year** 2015

Pages 164 **urn** http://urn.fi/URN:ISBN:978-952-60-6122-1

A? Aalto-yliopisto

Tiivistelmä

Aalto-yliopisto, PL 11000, 00076 Aalto www.aalto.fi

Tekijä
Risto Sarjonen

Väitöskirjan nimi
Large scattering lengths and long-range interactions in ultracold atomic gases

Julkaisija Perustieteiden korkeakoulu

Yksikkö Teknillisen fysiikan laitos

Sarja Aalto University publication series DOCTORAL DISSERTATIONS 34/2015

Tutkimusala Laskennallinen fysiikka

Käsikirjoituksen pvm 09.01.2015 **Väitöspäivä** 27.03.2015

Julkaisuluvan myöntämispäivä 24.02.2015 **Kieli** Englanti

☐ **Monografia** ☒ **Yhdistelmäväitöskirja (yhteenveto-osa + erillisartikkelit)**

Tiivistelmä

Tässä väitöskirjassa käsitellään bosonisia ja fermionisia kvanttikaasuja. Työn ensimmäisessä osassa mallinnetaan eräässä Bose-kaasussa tehdyn Braggin sirontakokeen tulokset variaatiolaskentaan perustuvan monen kappaleen teorian avulla. Kokeessa sirontapituus pystyttiin säätämään suureksi Feshbach-resonanssin avulla ja tämän takia olemassa olevia malleja ei voitu käyttää tulosten selittämiseen. Tämä teki kokeesta erityisen kiinnostavan tutkimuskohteen. Ensin kehitimme joukon ad hoc -potentiaaleja, joilla sovitimme havaitun eksitaatiospektrin. Myöhemmin hyödynsimme T-matriisiformalismia Feshbach-resonanssin kuvaamisessa ja tällöin pystyimme mallintamaan myös sidottujen tilojen energioita. Yhteenvetona mallista voidaan todeta, että se mallintaa havaitun eksitaatiospektrin ja antaa oikean sidotun tilan energian joissain tapauksissa.

Tämän työn toisessa osassa tutkitaan fermionisia kvanttikaasuja. Erityisesti tutkimme spin-riippuvaan optiseen hilaan vangittuja spin-1/2 hiukkasia. Hilageometriassa ylös-spin komponentti liikkuu hunajakennohilassa, mutta alas-spin komponentti on rajoitettu hunajakennohilan alihilaan, nimittäin kolmiohilaan. Sisällytimme malliimme attraktiivisen kontaktivuorovaikutuksen ja lähinaapurivuorovaikutuksen ja muotoilimme lähinaapurivuorovaikutusta kuvaavan termin siten, että se ottaa huomioon spontaanin ajankääntösymmetrian rikkoutumisen mahdollisuuden. Lisäksi otimme huomioon Fulde-Ferrell-Larkin-Ovchinnikov (FFLO) faasin mahdollisuuden. Keskiarvotetun kentän approksimaation puitteissa osoitimme, että FFLO tila on systeemin perustila useissa tapauksissa. Lisäksi osoitimme, että ajankääntösymmetria rikkoutuu spontaanisti, jos lähinaapurivuorovaikutus on riittävän voimakas. Lopuksi näytimme myös, että ajankääntösymmetria rikkoutuu joissain tapauksissa myös FFLO faasissa. Toisin sanoen löysimme faasin, jossa ajankääntösymmetria ja spatiaalinen symmetria rikkoutuvat yhtä aikaa.

Avainsanat kvanttikaasut, Bosen-Einsteinin kondensaatti, Feshbach-resonanssi, optinen hila, suprajuoksevuus, FFLO, topologiset faasit

ISBN (painettu) 978-952-60-6121-4 **ISBN (pdf)** 978-952-60-6122-1

ISSN-L 1799-4934 **ISSN (painettu)** 1799-4934 **ISSN (pdf)** 1799-4942

Julkaisupaikka Helsinki **Painopaikka** Helsinki **Vuosi** 2015

Sivumäärä 164 **urn** http://urn.fi/URN:ISBN:978-952-60-6122-1

Preface

I began my doctoral studies at the University of Oulu in 2007. During my time at the University of Oulu, my work was financially supported by the Finnish Cultural Foundation and the Finnish Academy of Science and Letters. However, later I transferred to the Aalto University, where I worked in Professor Päivi Törmä's research group. I thank Törmä for accepting me into her group, supervising my work and providing me with financial support.

Helsinki, February 25, 2015,

Risto Sarjonen

Contents

Preface i

Contents iii

List of Publications vii

Author's Contribution ix

1. Overview of ultracold quantum gases 1

1.1 Introduction 1

1.2 Angular momentum and spin 2

1.3 Distinguishable and indistinguishable particles 3

1.4 Transition from classical ideal gas to quantum gas 4

1.5 Introduction to optical lattices 6

1.6 Two-channel model of Feshbach resonance 7

2. Bosonic quantum gases 11

2.1 T-matrix formalism of Feshbach resonance 11

2.1.1 Phase shift and bound state energy 16

2.2 Variational many-body theory 17

2.3 Marchenko inversion 19

2.4 Review of Publications I-III 21

2.4.1 Motivation to potential scaling 21

2.4.2 Potential scaling with scattering length 22

2.4.3 Summary of Publication I 25

2.4.4 Summary of Publications II and III 26

2.5 A note on molecular Feshbach resonance state energies . . . 29

3. Fermionic quantum gases 31

3.1 Extended Fermi-Hubbard model 31

3.1.1 Fermi-Hubbard model . . . 31
3.1.2 Extended Fermi-Hubbard model . . . 32
3.2 BCS theory . . . 33
3.3 FFLO state . . . 36
3.4 Two-dimensional lattices . . . 37
3.4.1 Bravais lattices . . . 37
3.4.2 Primitive cell . . . 39
3.4.3 Reciprocal lattice . . . 39
3.4.4 Wave function in a periodic potential . . . 41
3.4.5 Honeycomb lattice . . . 44
3.5 Topological phases . . . 45
3.5.1 Hall conductivity and Chern numbers . . . 45
3.5.2 Time-Reversal Symmetry . . . 48
3.5.3 Ways to break time-reversal symmetry . . . 49
3.6 Note on Figure 3 of Ref. [1] . . . 50
3.7 Summary of Publication IV . . . 50
3.7.1 Deriving the grand potential . . . 51
3.7.2 Main results of Publication IV . . . 53

4. Summary **55**

Appendices **61**

A. Honeycomb-triangular lattice **61**
A.1 Preliminary results . . . 61
A.1.1 About notation . . . 61
A.1.2 Fourier transformation . . . 61
A.2 Noninteracting Hamiltonian in momentum space . . . 62
A.3 On-site interaction term in momentum space . . . 65
A.4 Nearest-neighbor interaction term $\mathcal{H}_{\mathrm{nn}}$ . . . 68
A.4.1 Nearest-neighbor interaction term in the mean-field approximation . . . 68
A.4.2 Mean-field Hamiltonian $\mathcal{H}_{\mathrm{nn}}^{\mathrm{MF}}$ in momentum space . . . 69
A.5 Full mean-field Hamiltonian in momentum space . . . 72

B. Triangular lattice **73**
B.1 Preliminary results . . . 73
B.1.1 Defining the full Hamiltonian . . . 73
B.2 Noninteracting Hamiltonian in momentum space . . . 74
B.3 On-site interaction term in momentum space . . . 76

B.4 Nearest-neighbor interaction term in momentum space . . . 76
B.5 Full mean-field Hamiltonian in momentum space 77
B.6 Deriving grand potential and particle number equations . . 78
B.6.1 Deriving grand potential 78
B.6.2 Equations for down- and up-spin particle numbers . . 79

Bibliography **81**

Publications **89**

List of Publications

This thesis consists of an overview and of the following publications which are referred to in the text by their Roman numerals.

I R. Sarjonen, M. Saarela and F. Mazzanti. Scaling of the interaction in BECs at large scattering lengths. *Eur. Phys. J. D*, 65, 25-32, October 2011.

II R. Sarjonen, M. Saarela and F. Mazzanti. Elementary excitations and universal interaction in Bose-Einstein condensates at large scattering lengths. *Phys. Rev. A*, 84, 041602, October 2011.

III R. Sarjonen, M. Saarela and F. Mazzanti. The Effective Two-Particle Interaction of Cold Atoms as Derived from Bragg Scattering. *J. Low Temp. Phys*, 169, 400-422, September 2012.

IV R. Sarjonen and P. Törmä. Topological States with Broken Translational and Time-Reversal Symmetries in a Honeycomb-Lattice. *ArXiv: 1409.6563*, January 2015.

Author's Contribution

Publication I: "Scaling of the interaction in BECs at large scattering lengths"

The author developed the step-well potential, which is the best of the discussed ad-hoc potentials. Furthermore, the author carried out some of the numerical calculations.

Publication II: "Elementary excitations and universal interaction in Bose-Einstein condensates at large scattering lengths"

It was the author's idea to employ inverse scattering theory, or Marchenko inversion, which provides the crucial link between T-matrix formalism and variational many-body theory. The author also carried out the numerical implementation of the Marchenko inversion, and calculated some of the other results presented in the paper.

Publication III: "The Effective Two-Particle Interaction of Cold Atoms as Derived from Bragg Scattering"

The author calculated some of the the numerical results and wrote the appendix about Marchenko inversion.

Publication IV: "Topological States with Broken Translational and Time-Reversal Symmetries in a Honeycomb-Lattice"

The author carried out all the calculations and was the main writer of the manuscript.

1. Overview of ultracold quantum gases

1.1 Introduction

Ultracold quantum gases are basically samples of atoms that have been prepared to a very low density and cooled down to temperatures near absolute zero. Therefore the wave nature of the atoms is manifestly present. Consequently, quantum mechanical effects, such as Bose-Einstein condensation and fermionic superfluidity, can be observed.

In experiments, quantum gases are trapped in magnetic or optical traps, with optical lattices being a well-known example of the latter trap type. In optical lattices, the properties of the gas, such as the interactions between particles, can be controlled. This high level of controllability allows for a fundamentally different approach compared to the one taken in other condensed matter systems. That is, using optical lattices one can construct an experimental system corresponding to some theoretical model, e.g. Hubbard model, whereas in other condensed matter physics experimentally observed phenomena motivate theoretical developments.

In this chapter, we will review some fundamental concepts related to ultracold quantum gases. In section 1.2 we will discuss spin, because it determines whether particles are bosons or fermions. Then we will move on to discuss the difference between distinguishable and indistinguishable particles and the transition from classical ideal gas to quantum gas. Finally, in sections 1.5 and 1.6 we will discuss optical lattices and Feshbach resonance, the latter being an important tool for tuning the interactions between particles in an ultracold quantum gas.

1.2 Angular momentum and spin

In classical mechanics, the angular momentum of a particle is defined as

$$\mathbf{L} = \mathbf{r} \times \mathbf{p}, \tag{1.1}$$

where $\mathbf{r}$ and $\mathbf{p}$ are the position and momentum vectors of the particle relative to the origin O of an inertial frame of reference. In quantum mechanics, the analogous quantity is called orbital angular momentum, and the operators corresponding to the Cartesian components of $\mathbf{L}$ are

$$\hat{L}_x = \hat{y}\hat{p}_z - \hat{z}\hat{p}_y, \tag{1.2}$$

$$\hat{L}_y = \hat{z}\hat{p}_x - \hat{x}\hat{p}_z, \tag{1.3}$$

$$\hat{L}_z = \hat{x}\hat{p}_y - \hat{y}\hat{p}_x. \tag{1.4}$$

Subsequently, the operator corresponding to the squared magnitude of angular momentum is

$$\hat{L}^2 = \hat{L}_x^2 + \hat{L}_y^2 + \hat{L}_z^2. \tag{1.5}$$

The preceding angular momentum operators satisfy the commutation relations

$$[\hat{L}_\alpha, \hat{L}_\beta] = i\hbar\epsilon_{\alpha\beta\gamma}\hat{L}_\gamma, \tag{1.6}$$

$$[\hat{L}^2, \hat{L}_\alpha] = 0, \tag{1.7}$$

where $\alpha, \beta, \gamma \in \{x, y, z\}$ and $\epsilon_{\alpha\beta\gamma}$ is the Levi-Civita symbol.

Orbital angular momentum is quantized. To be more precise, the eigenvalues of $\hat{L}^2$ are of the form $l(l+1)\hbar^2$, where the orbital quantum number $l \in \{0, 1, 2, \cdots\}$. On the other hand, the eigenvalues of operators L_α are $m_l\hbar$, where the magnetic quantum number $m_l \in \{-l, -l+1, \cdots, l\}$.

In addition to orbital angular momentum, elementary particles, composite particles and atomic nuclei may have an intrinsic angular momentum called spin, which has no direct counterpart in classical mechanics. This intrinsic angular momentum, or spin, can be detected e.g. in the famous Stern-Gerlach experiment. Let us now say that $\hat{S}^2$ is the operator corresponding to the squared magnitude of spin, and $\hat{S}_x$, $\hat{S}_y$, $\hat{S}_z$ are the operators corresponding to the three Cartesian components of spin. In analogy with orbital angular momentum, the spin operators satisfy the

commutation relations

$$[\hat{S}_\alpha, \hat{S}_\beta] = i\hbar\epsilon_{\alpha\beta\gamma}\hat{S}_\gamma, \tag{1.8}$$

$$[\hat{S}^2, \hat{S}_\alpha] = 0. \tag{1.9}$$

Like orbital angular momentum, spin is also quantized. The eigenvalues of $\hat{S}^2$ are of the form $s(s+1)\hbar^2$, where the spin quantum number $s \in \{0, \frac{1}{2}, 1, \frac{3}{2}, \cdots\}$. That is, the spin quantum number may obtain integer and half-integer values. Subsequently, the eigenvalues of operators S_α are $m_s\hbar$, where the spin quantum number $m_s \in \{-s, -s+1, \cdots, s\}$. Particles with integer spin are called bosons, and particles with half-integer spin are called fermions.

1.3 Distinguishable and indistinguishable particles

In classical mechanics, all particles are distinguishable. In other words, it is (implicitly) assumed that particles can always be distinguished from one another by some experiment. However, if we have a set of particles whose all internal states are the same, then there is no way to distinguish one particle from another on the grounds of their intrinsic properties. Consequently, particles having the same internal states are called identical particles, and two physical situations differing only by an interchange of identical particles are indistinguishable. Thus, any physical Hamiltonian must be invariant under permutation of identical particles, and two quantum mechanical states that differ only by a permutation of identical particles cannot be distinguished by any observation whatsoever [2].

Motivated by the preceding remarks, the theory of nonrelativistic quantum mechanics has the symmetrization postulate, which states that

- Particles whose spin is a half-integer multiple of $\hbar$ have only antisymmetric states. (These particles are called fermions.)

- Particles whose spin is an integer multiple of $\hbar$ have only symmetric states. (These particles are called bosons.)

- Particles cannot have partially symmetric states.

However, within relativistic quantum mechanics it suffices to postulate that particles cannot have partially symmetric states, because the connection between the spin of a particle and the symmetry of the allowed states is given by the spin-statistics connection [3, 4]. Moreover, there is strong empirical evidence suggesting that the symmetrization postulate and spin-statistics connection are sound. For example, part (a) of the symmetrization postulate implies that in a system of identical fermions two or more particles cannot have precisely the same internal state. That is, part (a) implies the Pauli exclusion principle. Since the exclusion principle forms the basis of atomic structure and atomic spectra, part (a) is strongly supported by experiments. On the other hand, multiple bosons can occupy the same single-particle state because their wave function is symmetric. Since this is the key prerequisite for Bose-Einstein condensation, part (b) is also well-supported by empirical evidence. Moreover, since all particles are either bosons or fermions, it is now logical to say that partially symmetric states do not exist. Note, however, that some quasiparticles that are not elementary particles may have fractional statistics. For example, see the discussion on anyons in Ref. [5].

1.4 Transition from classical ideal gas to quantum gas

Traditionally, one of the most important subjects of study in statistical physics is the ideal gas. In the ideal gas model, the interactions between particles are assumed to be absent. Physically, this assumption is allowed if the interaction between particles is small irrespective of the distance between them, or the gas is sufficiently rarified. In the latter case, which is the more important, the rarefaction causes the average distance between particles to be large compared to the range of the interaction. Thus, a sufficiently rarefied gas behaves like an ideal gas. It is well-known that the speed distribution of particles in a classical ideal gas is given by the Maxwell distribution [6]

$$f(v) = \left(\frac{m}{2\pi k_{\mathrm{B}} T}\right)^{3/2} 4\pi v^2 e^{-mv^2/(2k_{\mathrm{B}}T)}, \tag{1.10}$$

where T is temperature and k_{B} is the Boltzmann constant.

In a classical ideal gas the constituents of the gas are treated entirely as distinguishable particles [7]. Thus, their wave nature is not considered. However, particles in a real gas are actually wave packets, and the wave

nature manifests in experiments if temperature is low enough. That is because the wave packets start to spread when temperature decreases, and when they begin to overlap with each other, quantum effects must be taken into account [8].

The spatial extension of a wave packet is determined by the de Broglie wavelength $\lambda = h/p_0$, where h is the Planck constant and p_0 is the average momentum. In order to determine the temperature dependence of λ, we calculate the thermal average of the de Broglie wavelength by using the Maxwell speed distribution (1.10). We obtain

$$\langle \lambda \rangle = \frac{h}{m} \int_0^\infty \frac{f(v)}{v}\, dv = \sqrt{\frac{2h^2}{\pi m k_{\mathrm{B}} T}}. \tag{1.11}$$

On the other hand, the average distance between particles is

$$d = n^{-1/3}, \tag{1.12}$$

where n is the number density of particles. Thus, quantum mechanical effects start to become important when

$$d \lesssim \langle \lambda \rangle \quad \text{or} \quad k_{\mathrm{B}} T \lesssim \frac{2h^2 n^{2/3}}{\pi m}. \tag{1.13}$$

That is, when Eq. (1.13) is satisfied, the Pauli exclusion principle must be taken into account and the distribution of fermionic particles must be described with Fermi-Dirac statistics. Similarly, in a bosonic gas Bose-Einstein condensation sets in when Eq. (1.13) is satisfied [9].

In conclusion, we note that the usual point of reference in the literature is the thermal de Broglie wavelength defined as [8, 9, 10]

$$\lambda_{\mathrm{T}} = \frac{h}{\sqrt{2\pi m k_{\mathrm{B}} T}}. \tag{1.14}$$

The numerical factors in Eq. (1.14) have been chosen to give a neater appearance for certain formulas [8, 10]. However, the fact that $\langle \lambda \rangle$ and λ_{T} differ by a factor of 2 is not significant, because Eq. (1.13) is only an approximation.

1.5 Introduction to optical lattices

When several laser beams are overlapped with each other, the individual electric fields interfere and create an intensity and polarization pattern [11, 12]. On the other hand, when neutral atoms are subjected to an electric field, the positively charged nucleus and negatively charged electrons are pulled away from each other. That is, the electric field induces a polarization into the atom. The induced dipole moment, in turn, interacts with the electric field and a force is exerted on the atom. Usually, this force is described in terms of the underlying potential, called optical dipole potential. Consequently, for cold atoms, the interference pattern resulting from overlapping laser beams can serve as a periodic potential. Due to the strong analogy of such systems with conventional solids, the term optical lattice has been coined for this artificial crystal created by light. The resulting lattice geometry is, of course, determined by the overall geometry of the intersecting laser beams.

In the early 1990s, traps were mainly considered as a tool for laser cooling [11]. Ground-state cooling was finally achieved in 1995 in harmonic traps with the realization of Bose-Einstein condensation [13, 14, 15]. This exotic state of matter appears when trapped bosonic atoms are cooled below a critical temperature, where a macroscopic fraction of the ensemble occupies the lowest energy single-particle energy state. This quantum degenerate state of atoms can be described by a single, macroscopic wave function called order parameter. One of the prominent features of an interacting Bose-Einstein condensate is its superfluidity, which has been confirmed by the observation of interference [16] and vortices [17, 18].

Advances in experimental techniques and the ground-breaking discovery of Bose-Einstein condensation caused ultracold atomic gases in optical lattices to become a research field of its own. One important experiment in this field was the observation of superfluid to Mott insulator transition in a three-dimensional optical lattice [19]. This experiment makes use of the fact that the tunneling rate of atoms between neighboring sites (potential wells) depends on the height of the barrier. Consequently, tunneling rate is reduced when the lattice potential is made deeper. For ultracold bosons, this leads to a phase transition from a delocalized superfluid state to an insulating state where the atoms are localized at the individual lattice sites.

In modern quantum gas setups, degenerate bosonic gases[20, 19], fer-

mionic gases[21, 22], Bose-Bose and Bose-Fermi mixtures [23, 24, 25] and molecules [26, 27] of different species can be loaded in optical lattices of various dimensionalities. There is also a wide selection of methods that can be used to control and study these systems. For example, tunneling rates can be adjusted by changing the depth of the lattice, and the strength of the on-site interaction can be controlled with Feshbach resonances [28]. In the recent years, it has also become possible to realize spin-dependent confinement [29, 30, 31, 11], and this has led to theoretical proposals of new concepts, such as mixed-geometry pairing [1]. Another recent advance is the possibility to realize long-range interactions between particles trapped in an optical lattice.

Fermionic dipolar molecules, such as ^{40}K^{87}Rb, provide one way to realize long-range interactions [32, 33, 34]. The long-range interactions can be controlled by changing the geometry of the trapping [35], whereas the on-site interaction can be tuned by using Feshbach resonances. Consequently, dipolar molecules allow on-site and long-range interactions to be controlled independently of each other [35], and therefore they are well-suited for emulating the extended Fermi-Hubbard model [36, 37, 38, 39, 40]. Another way to realize long-range interactions is to use Bose-Fermi mixtures like ^{40}K and ^{87}Rb, where the bosonic component induces attractive nearest-neighbor (NN) interactions between the fermions [41, 42, 43, 44]. The NN interaction can be adjusted by using its dependence on the depth of the lattice [44]. Since the on-site interaction can be controlled independently of the NN interaction by using Feshbach resonances, Bose-Fermi mixtures allow versatile emulation of the extended Fermi-Hubbard model.

1.6 Two-channel model of Feshbach resonance

Each alkali atom has one valence electron. Consequently, if we neglect hyperfine interaction, the coupled spin state of two alkali atoms corresponds to the coupled spins of the two valence electrons. Thus, the spin state of the two colliding alkali atoms is either a singlet state $|\mathrm{S}\rangle$ or a triplet state $|\mathrm{T}\rangle$. If the electrons form a singlet bond, i.e. they have opposing spins, they are allowed to be on top of each other. On the other hand, if the electrons form a triplet bond, i.e. they have the same spin, they are subject to Pauli repulsion. Consequently, the singlet potential is generally much deeper than the triplet potential [45].

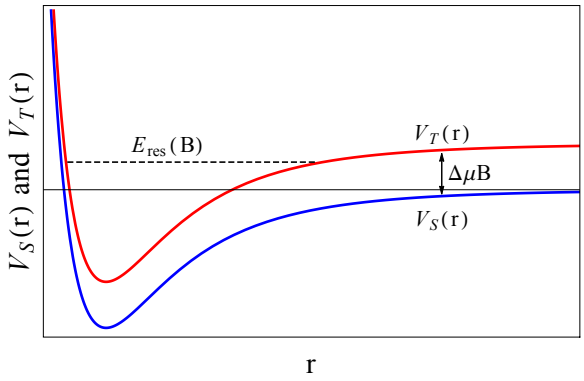

Figure 1.1. Schematic illustration of the singlet and triplet potentials $V_{\mathrm{S}}(\mathbf{r})$ and $V_{\mathrm{T}}(\mathbf{r})$. Also shown is $E_{\mathrm{res}}(B)$, i.e. the magnetic-field dependent energy of the resonance state $\phi_{\mathrm{res}}(\mathbf{r})$.

In reality, every atom has also a nucleus with spin $\mathbf{I}$ that interacts with the spin $\mathbf{S}$ of the valence electron. This hyperfine interaction is described by the Hamiltonian

$$\hat{H}_{\mathrm{hf}} = \frac{\alpha_{\mathrm{hf}}}{\hbar^2}\hat{\mathbf{I}}\cdot\hat{\mathbf{S}}, \tag{1.15}$$

where α_{hf} is the hyperfine constant. The hyperfine interaction couples the singlet and triplet states if the atoms are close enough to each other, and we denote the coupling matrix element with $V_{\mathrm{hf}}(\mathbf{r}) = \langle \mathrm{S}|\hat{H}_{\mathrm{hf}}|\mathrm{T}\rangle$.

In order to write down the two-channel Schrödinger equation for the system, we say that $\hat{S} = |\mathrm{S}\rangle\langle\mathrm{S}|$ and $\hat{T} = |\mathrm{T}\rangle\langle\mathrm{T}|$. That is, $\hat{S}$ and $\hat{T}$ are projection operators to the singlet and triplet subspaces, respectively. We note that $\hat{S} + \hat{T} = 1$ because we assume that $|\mathrm{S}\rangle$ and $|\mathrm{T}\rangle$ are the only allowed spin configurations. On the other hand, the wave function of the system can be written as

$$|\psi\rangle = \psi_{\mathrm{S}}(\mathbf{r})|\mathrm{S}\rangle + \psi_{\mathrm{T}}(\mathbf{r})|\mathrm{T}\rangle, \tag{1.16}$$

where $\psi_{\mathrm{S}}(\mathbf{r})$ and $\psi_{\mathrm{T}}(\mathbf{r})$ are the spatial wave functions corresponding to the singlet and triplet states, respectively. By multiplying the Schrödinger equation $H|\psi\rangle = E|\psi\rangle$ from the left by $\langle\mathrm{T}|$ and $\langle\mathrm{S}|$, we obtain the coupled equations

$$(E - H_{\mathrm{TT}})\psi_{\mathrm{T}}(\mathbf{r}) = H_{\mathrm{TS}}\psi_{\mathrm{S}}(\mathbf{r}), \tag{1.17}$$

$$(E - H_{\mathrm{SS}})\psi_{\mathrm{S}}(\mathbf{r}) = H_{\mathrm{ST}}\psi_{\mathrm{T}}(\mathbf{r}), \tag{1.18}$$

where $H_{\mathrm{SS}} = \langle\mathrm{S}|H|\mathrm{S}\rangle$, $H_{\mathrm{TT}} = \langle\mathrm{T}|H|\mathrm{T}\rangle$, $H_{\mathrm{ST}} = \langle\mathrm{S}|H|\mathrm{T}\rangle$ and $H_{\mathrm{TS}} = \langle\mathrm{T}|H|\mathrm{S}\rangle$.

Equations (1.17) and (1.18) can be written as a matrix equation

$$\begin{pmatrix} -\frac{\hbar^2\nabla^2}{m} + V_{\mathrm{T}}(\mathbf{r}) - E & V_{\mathrm{hf}}(\mathbf{r}) \\ V_{\mathrm{hf}}(\mathbf{r}) & -\frac{\hbar^2\nabla^2}{m} + V_{\mathrm{S}}(\mathbf{r}) - E \end{pmatrix} \begin{pmatrix} \psi_{\mathrm{T}}(\mathbf{r}) \\ \psi_{\mathrm{S}}(\mathbf{r}) \end{pmatrix} = 0, \tag{1.19}$$

where we have also written out the Hamiltonians. The potentials $V_{\mathrm{T}}(\mathbf{r})$ and $V_{\mathrm{S}}(\mathbf{r})$ are associated with triplet and singlet states, respectively, and m is twice the reduced mass of the atom pair. For the sake of simplicity, it can be assumed that

$$V_{\mathrm{T}}(\mathbf{r}) = V(\mathbf{r}) + \Delta\mu B, \tag{1.20}$$

$$V_{\mathrm{S}}(\mathbf{r}) = V(\mathbf{r}), \tag{1.21}$$

where the interatomic potential $V(\mathbf{r})$ could be taken to be e.g. a Lennard-Jones type potential. The energy difference of triplet and singlet potentials results from the Zeeman shift $\Delta\mu B$, where $\Delta\mu$ is the difference of magnetic moments between triplet and singlet states, and B is the external magnetic field. The shape of the coupling potential $V_{\mathrm{hf}}(\mathbf{r})$ remains largely unknown, but it is known to be a short-ranged. Thus, it can be modeled with any reasonable short-ranged function, e.g. a short-ranged Gaussian function [46, 47].

The long-range behavior of the lth partial-wave radial wave function is $R_l(r) \to \sin(kr - \pi l/2 + \delta_l(k))/(kr)$, where $\delta_l(k)$ is the scattering phase shift caused by the scattering potential [2]. In the following, we consider low-energy s-wave scattering and suppress the index $l = 0$. That is, we define $\delta(k) = \delta_0(k)$. The scattering length is defined as $a(B) = -\lim_{k\to 0} k^{-1} \tan\delta(k)$, where the magnetic field dependence appears due to the Feshbach resonance. On the other hand, a Feshbach resonance is based on the existence of a bound state that is nearly degenerate with the scattering continuum. That is, we assume that $V_{\mathrm{T}}(\mathbf{r})$ supports a bound state $\phi_{\mathrm{res}}(\mathbf{r})$ with energy $E_{\mathrm{res}} = \Delta\mu(B - B_{\mathrm{res}})$. Consequently, by varying B the scattering length can be tuned according to the relation [47]

$$a(B) = a_{\mathrm{bg}} \left(1 - \frac{\Delta B}{B - B_0}\right), \tag{1.22}$$

where a_{bg} is the scattering length far away from the resonance, ΔB characterizes the width of the resonance, and B_0 is the resonance location. Additionally, the coupled system supports a bound state whose binding

energy near the resonance is

$$E_{\mathrm{b}}(B) = \frac{\hbar^2}{ma^2(B)}. \tag{1.23}$$

2. Bosonic quantum gases

Traditionally, the quantum Bose fluid that was mostly used to test many-body theories was liquid ^{4}He. It provided a clean environment to study ground state properties and excitation spectrum, and a variational many-body theory was developed to explain the observations [48, 49]. We will briefly review this variational theory in section 2.2.

Nowadays, ultracold bosonic atoms confined to magnetic or optical traps provide a highly controllable testing ground for many-body theories. To name a famous example, sodium atoms confined to a magneto-optical trap were used to detect Bose-Einstein condensation [16, 50].

In section 2.1 we will have a look at Feshbach resonance, which can be used to tune interactions between particles confined to a trap or optical lattice. In section 2.2 we will briefly review the variational many-body theory, and in section 2.3 we will have a look at the Marchenko inversion. Marchenko inversion is a method from inverse scattering theory, and in Publications II and III we used it to establish a connection between variational many-body theory and T-matrix formalism of Feshbach resonance. Finally, in section 2.4 we will summarize the main results from publications I, II and III. In those publications, we described the behavior of a strongly interacting atomic Bose gas with a many-body model that originates from the study of liquid helium ^{4}He.

2.1 T-matrix formalism of Feshbach resonance

Feshbach resonance [51] is often described in terms of a fairly simple two-channel model, which has one open and one closed channel. We denote the subspaces containing open and closed channels by P and Q, respectively. A schematic representation of the open and closed channel potentials has been given in Fig. 1.1. As the names suggest, the long-range

asymptotic value of the open channel potential is below the scattering energy E, whereas the long-range asymptotic value of the closed channel potential is above the scattering energy E.

In bra-ket notation, Eqs. (1.17) and (1.18) now read

$$(E - H_{PP})|\Psi_P\rangle = H_{PQ}|\Psi_Q\rangle, \tag{2.1}$$

$$(E - H_{QQ})|\Psi_Q\rangle = H_{QP}|\Psi_P\rangle. \tag{2.2}$$

The formal solution of Eq. (2.2) is [9]

$$|\Psi_Q\rangle = (E - H_{QQ} + i\epsilon)^{-1} H_{QP}|\Psi_P\rangle, \tag{2.3}$$

where the positive infinitesimal imaginary part ϵ in the denominator ensures that the scattered wave has only outgoing terms. Substituting Eq. (2.3) into Eq. (2.1), one obtains

$$(E - H_{PP} - H'_{PP})|\Psi_P\rangle = 0, \tag{2.4}$$

where

$$H'_{PP} = H_{PQ}(E - H_{QQ} + i\epsilon)^{-1} H_{QP}. \tag{2.5}$$

Let us now employ the resolution of identity $I = \sum_{\mathbf{k}} |\psi_k\rangle\langle\psi_k|$, where the sum goes over bound and continuum eigenstates of H_{QQ}. Since we assume that one bound state $|\phi_{\text{res}}\rangle$ is near-degenerate with the scattering threshold, the dominating contribution comes from that term, and the rest of the terms can be neglected. Thus we obtain

$$H'_{PP} = \frac{H_{PQ}|\phi_{\text{res}}\rangle\langle\phi_{\text{res}}|H_{QP}}{E - E_{\text{res}}}. \tag{2.6}$$

Now one can identify the effective open channel potential from Eqs. (2.4) and (2.6). It reads

$$U(E) = V_{PP} + \frac{H_{PQ}|\phi_{\text{res}}\rangle\langle\phi_{\text{res}}|H_{QP}}{E - E_{\text{res}}}, \tag{2.7}$$

where V_{PP} is the potential appearing in the Hamiltonian H_{PP}. The T-matrix corresponding to interaction $U(E)$ satisfies the Lippmann-Schwinger equation

$$T(E) = U(E) + U(E)G_0T(E), \tag{2.8}$$

where G_0 is the free particle Green function. The Green's function can be written as

$$G_0 = \frac{1}{E - H_0 + i\epsilon} = \frac{1}{(2\pi)^3} \int d^3p \frac{|\mathbf{p}\rangle\langle\mathbf{p}|}{E - \frac{\hbar^2 p^2}{m} + i\epsilon}, \tag{2.9}$$

where the plane wave normalization

$$\langle \mathbf{p}|\mathbf{p}'\rangle = (2\pi)^3 \delta(\mathbf{p} - \mathbf{p}'). \tag{2.10}$$

was assumed. By using Eqs. (2.8) and (2.9), one can write down the momentum space matrix element

$$\langle \mathbf{k}|T(E)|\mathbf{k}'\rangle = \langle \mathbf{k}|U(E)|\mathbf{k}'\rangle + \frac{1}{(2\pi)^3} \int \frac{\langle \mathbf{k}|U(E)|\mathbf{p}\rangle\langle \mathbf{p}|T(E)|\mathbf{k}'\rangle}{E - \frac{\hbar^2 p^2}{m} + i\epsilon} \, d^3p. \tag{2.11}$$

For many applications it is convenient to work in a single partial wave channel. In that case, one may perform the angular integrals in (2.11) explicitly. One obtains [52]

$$\langle k|T(E)|k'\rangle = \langle k|U(E)|k'\rangle + \frac{2}{\pi} \int \frac{\langle k|U(E)|p\rangle\langle p|T(E)|k'\rangle}{E - \frac{\hbar^2 p^2}{m} + i\epsilon} \, p^2 dp, \tag{2.12}$$

where the states $|k\rangle$ are spherical Bessel functions $j_l(kr)$ in position representation and satisfy the relation

$$\langle k|k'\rangle = \frac{\pi}{2} \frac{1}{k^2} \delta(k - k'). \tag{2.13}$$

We wish to analytically solve for the T-matrix, and therefore we have to make a couple of simplifying assumptions in the following. First, we substitute a separable ansatz

$$\langle p|T(E)|k'\rangle = f(p)\tau(E, k') \tag{2.14}$$

into Eq. (2.12). For the on-shell T-matrix having $k' = k$ and $E = \hbar^2 k^2/m$ one obtains

$$f(k)\tau(E, k) = \langle k|U(E)|k\rangle + \frac{2}{\pi} \int \frac{\langle k|U(E)|p\rangle f(p)\tau(E, k)}{E - \frac{\hbar^2 p^2}{m} + i\epsilon} \, p^2 dp. \tag{2.15}$$

Solving for $\tau(E, k)$ algebraically, one obtains

$$\tau(E, k) = \frac{\langle k|U(E)|k\rangle}{f(k) - \frac{2}{\pi} \int \frac{\langle k|U(E)|p\rangle f(p)}{E - \frac{\hbar^2 p^2}{m} + i\epsilon} \, p^2 dp}. \tag{2.16}$$

From Eq. (2.7) one obtains

$$\langle k|U(E)|p\rangle = \langle k|V_{PP}|p\rangle + \frac{\langle k|H_{PQ}|\phi_{\rm res}\rangle\langle\phi_{\rm res}|H_{QP}|p\rangle}{E - E_{\rm res}}. \tag{2.17}$$

Let us now say that

$$\langle k|H_{PQ}|\phi_{\rm res}\rangle \;\; = \;\; h_0 f(k), \tag{2.18}$$

where h_0 is a constant and $f(k)$ is called a cutoff function. Since one is interested in low-energy scattering, V_{PP} can be approximated with a separable potential. Thus, one can write

$$\langle k|V_{PP}|p\rangle \;\; = \;\; \lambda_0 f(k) f(p), \tag{2.19}$$

where λ_0 is constant and $f(k)$ is the same cutoff function as in Eq. (2.18). Note that we used the same cutoff function $f(k)$ in Eqs. (2.18) and (2.19) for the sake of simplicity [53]. By using Eqs. (2.18) and (2.19), one casts Eq. (2.17) into form

$$\langle k|U(E)|p\rangle = \left(\lambda_0 + \frac{h_0^2}{E - E_{\rm res}}\right) f(k) f(p). \tag{2.20}$$

By substituting Eq. (2.20) into Eq. (2.16), one obtains

$$\tau(E,k) = \frac{f(k)}{\left(\lambda_0 + \dfrac{h_0^2}{E - E_{\rm res}}\right)^{-1} - \dfrac{2}{\pi}\displaystyle\int \frac{f^2(p)}{E - \frac{\hbar^2 p^2}{m} + i\epsilon}\, p^2 dp}. \tag{2.21}$$

By multiplying both sides by $f(k)$ and using Eq. (2.14), one obtains

$$\langle k|T(E)|k\rangle = \frac{f^2(k)}{\left(\lambda_0 + \dfrac{h_0^2}{E - E_{\rm res}}\right)^{-1} - \dfrac{2}{\pi}\displaystyle\int \frac{f^2(p)}{E - \frac{\hbar^2 p^2}{m} + i\epsilon}\, p^2 dp}. \tag{2.22}$$

The scattering phase shift $\delta(k)$ can be solved from the scattering amplitude

$$f_s(k) = \frac{1}{k}\exp[i\delta(k)]\sin\delta(k) = \frac{1}{k\cot\delta(k) - ik}. \tag{2.23}$$

On the other hand, the on-shell T-matrix $\langle k|T(E)|k\rangle$ and scattering amplitude $f_s(k)$ and are related by [Eq. V(17) in Ref. [52]]

$$\langle k|T(E)|k\rangle = -\frac{\hbar^2}{m} f_s(k). \tag{2.24}$$

Because $k \cot \delta(k) = -1/a(B) + O(k^2)$, one obtains

$$\lim_{k\to 0} \langle k|T(E)|k\rangle = \frac{\hbar^2 a(B)}{m} \tag{2.25}$$

with $a(B)$ being defined in Eq. (1.22). Fixing $f(0) = 1$ and using Eqs. (2.22) and (2.25), one obtains the $E \to 0$ limit

$$\left(\lambda_0 - \frac{h_0^2}{E_{\rm res}}\right)^{-1} + \frac{2m}{\pi\hbar^2}\int f^2(p)\, dp = \frac{m}{\hbar^2}\frac{1}{a(B)}. \tag{2.26}$$

The parameters λ_0, h_0 and $E_{\rm res}$ are not physically accessible whereas $a_{\rm bg}$, ΔB, $\Delta\mu$ and B_0 are. Therefore λ_0, h_0 and $E_{\rm res}$ must be expressed in terms of $a_{\rm bg}$, ΔB, $\Delta\mu$ and B_0 in such a way that one obtains the correct scattering length $a(B)$ defined in Eq. (1.22). The renormalization relations read [54]

$$\lambda_0 = \Gamma\bar{\lambda}_0, \tag{2.27}$$

$$h_0 = \Gamma\bar{h}_0, \tag{2.28}$$

$$E_{\rm res} = \bar{E}_{\rm res} + \alpha\Gamma\bar{h}_0^2, \tag{2.29}$$

where $\Gamma = 1/(1-\alpha\bar{\lambda}_0)$. Employing the renormalization relations, one obtains

$$\begin{aligned}
\frac{1}{\lambda_0 - \dfrac{h_0^2}{E_{\rm res}}} &= \frac{1}{\Gamma\bar{\lambda}_0 - \dfrac{\Gamma^2\bar{h}_0^2}{\bar{E}_{\rm res} + \alpha\Gamma\bar{h}_0^2}} \\
&= \frac{\bar{E}_{\rm res} + \alpha\Gamma\bar{h}_0^2}{\Gamma\bar{\lambda}_0(\bar{E}_{\rm res} + \alpha\Gamma\bar{h}_0^2) - \Gamma^2\bar{h}_0^2} \\
&= \frac{\bar{E}_{\rm res} + \alpha\Gamma\bar{h}_0^2}{\Gamma\bar{\lambda}_0\bar{E}_{\rm res} + \Gamma^2\underbrace{(\alpha\bar{\lambda}_0 - 1)}_{=-1/\Gamma}\bar{h}_0^2} \\
&= \frac{\bar{E}_{\rm res}/\Gamma + \alpha\bar{h}_0^2}{\bar{\lambda}_0\bar{E}_{\rm res} - \bar{h}_0^2} \qquad ||1/\Gamma = 1 - \alpha\bar{\lambda}_0 \\
&= \frac{\bar{E}_{\rm res} + \alpha(\bar{h}_0^2 - \bar{\lambda}_0\bar{E}_{\rm res})}{\bar{\lambda}_0\bar{E}_{\rm res} - \bar{h}_0^2} \\
&= \frac{\bar{E}_{\rm res}}{\bar{\lambda}_0\bar{E}_{\rm res} - \bar{h}_0^2} - \alpha.
\end{aligned} \tag{2.30}$$

Equations (2.26) and (2.30) imply that

$$\alpha = \frac{2m}{\pi\hbar^2}\int f^2(p)\, dp \tag{2.31}$$

and

$$\bar{\lambda}_0 = \frac{\hbar^2 a_{\rm bg}}{m}, \tag{2.32}$$

$$\bar{h}_0^2 = \Delta B \Delta\mu \frac{\hbar^2 a_{\rm bg}}{m}, \tag{2.33}$$

$$\bar{E}_{\rm res} = \Delta\mu(B - B_0). \tag{2.34}$$

Thus Eq. (2.22) becomes

$$\langle k|T(E)|k\rangle = \frac{\hbar^2}{m} \frac{f^2(k)}{a_{\rm bg}^{-1}\left(1 + \frac{\Delta\mu\Delta B}{\frac{\hbar^2k^2}{m} - \Delta\mu(B-B_0)}\right)^{-1} - \frac{2}{\pi}k^2 \int \frac{f^2(p)}{\frac{\hbar^2k^2}{m} - \frac{\hbar^2p^2}{m} + i\epsilon}\, dp}, \tag{2.35}$$

where we have written out $E = \hbar^2k^2/m$.

2.1.1 Phase shift and bound state energy

According to Eqs. (2.23) and (2.24), the phase shift $\delta(k)$ can be calculated from the effective range function

$$k\cot\delta(k) = -\frac{a_{\rm bg}^{-1}\left(1 + \frac{\Delta\mu\Delta B}{\frac{\hbar^2k^2}{m} - \Delta\mu(B-B_0)}\right)^{-1} - \frac{2}{\pi}k^2\mathcal{P}\int \frac{f^2(p)}{\frac{\hbar^2k^2}{m} - \frac{\hbar^2p^2}{m}}\, dp}{f^2(k)}, \tag{2.36}$$

where $\mathcal{P}$ denotes the Cauchy principal value integral. On the other hand, the bound state energy is determined by the pole $k = i\kappa$ of the on-shell T-matrix $\langle k|T(E)|k\rangle$. That is, binding energy $E_{\rm b} = \hbar^2\kappa^2/m$ with κ being determined by the condition

$$a_{\rm bg}^{-1}\left(1 - \frac{\Delta\mu\Delta B}{\frac{\hbar^2\kappa^2}{m} + \Delta\mu(B - B_0)}\right)^{-1} = \frac{2}{\pi}\kappa^2 \int \frac{f^2(p)}{\frac{\hbar^2\kappa^2}{m} + \frac{\hbar^2p^2}{m}}\, dp. \tag{2.37}$$

Knowing the binding energy $E_{\rm b} = \hbar^2\kappa^2/m$ from experiments or full coupled-channels calculations, we can actually use Eq. (2.37) to determine an ansatz for the cutoff function $f(p)$. Subsequently, we can calculate the phase shift $\delta(k)$ from Eq. (2.36), and determine the corresponding local potential by using inverse scattering theory (Marchenko inversion). The local potential can be used in the variational many-body theory to calculate the excitation spectrum (Feynman spectrum) $\epsilon_{\rm F}(k)$, which, in turn, can be compared with the experimentally determined spectrum.

2.2 Variational many-body theory

Let us next review the variational many-body theory that we used in Publications I-III to calculate the excitation spectrum of an atomic Bose gas. For that purpose, we consider a system of N spinless bosons of mass m with pairwise interaction in a volume Ω. The Hamiltonian of the system is (see e.g. [55])

$$H = -\frac{\hbar^2}{2m}\sum_{j=1}^{N}\nabla_j^2 + \sum_{\langle i,j\rangle} V(r_{ij}), \tag{2.38}$$

where the sum $\sum_{\langle i,j\rangle}$ goes over distinct particle pairs and r_{ij} is the distance between particles i and j. For the ground state wave function, one uses an ansatz which is a product of two-body correlation factors $f_c(r_{ij})$. That is, one uses an ansatz

$$\Psi_0 = \prod_{\langle i,j\rangle}^{N} f_c(r_{ij}). \tag{2.39}$$

On physical grounds, one expects that the correlation factor $f_c(r)$ goes to unity as r goes to infinity, because particles far away from each other do not interact with each other in any way. Anyway, the optimal Jastrow correlation factor $f_c(r)$ is obtained by minimizing, without restrictions, the expectation value of the Hamiltonian (2.38), giving the ground state energy

$$E[f_c] = \frac{\langle\Psi_0|H|\Psi_0\rangle}{\langle\Psi_0|\Psi_0\rangle}. \tag{2.40}$$

This is accomplished by solving the Euler-Lagrange equation [56, 55]

$$\frac{\delta E[f_c]}{\delta f_c(r)} = 0. \tag{2.41}$$

The energy can also be expressed in terms of the radial distribution function

$$g(r_{12}) = \frac{N(N-1)}{\rho^2}\frac{\int d\mathbf{r}_3 d\mathbf{r}_4\cdots d\mathbf{r}_N|\Psi_0|^2}{\int d\mathbf{r}_1 d\mathbf{r}_2 d\mathbf{r}_3 d\mathbf{r}_4\cdots d\mathbf{r}_N|\Psi_0|^2} \tag{2.42}$$

or the static structure function

$$S(k) = 1 + \rho\int d\mathbf{r} e^{i\mathbf{k}\cdot\mathbf{r}}[g(r)-1], \tag{2.43}$$

where $\rho = N/V$ is the number density of particles. Variation of $E[S]$ leads to the equations [57]

$$S(k) = \frac{t(k)}{\sqrt{t^2(k) + 2V_{\rm ph}(k)t(k)}}, \tag{2.44}$$

with $t(k) = \hbar^2 k^2/(2m)$ and $V_{\rm ph}(k)$ the so-called particle-hole potential. In coordinate space

$$V_{\rm ph}(r) = g(r)V(r) + \frac{\hbar^2}{m}|\nabla\sqrt{g(r)}|^2 + [g(r) - 1]\omega_{\rm ind}(r), \tag{2.45}$$

where the momentum space induced interaction

$$\omega_{\rm ind}(k) = -\frac{1}{2}t(k)\frac{[2S(k) + 1][S(k) - 1]^2}{S^2(k)}. \tag{2.46}$$

Equation (2.43) implies that $g(r) - 1$ is an inverse Fourier transformation of $S(k) - 1$. That is,

$$g(r) = 1 + \frac{1}{2\pi^2\rho r}\int_0^\infty k(S(k) - 1)\sin(kr)\,dk. \tag{2.47}$$

Equations (2.43)-(2.47) form a set of equations called hypernetted chain (HNC) equations. They can be solved iteratively, and the initial guess is to set the particle-hole potential equal to the Fourier transform of the two-body potential. That is, one starts by setting $V_{\rm ph}(k) = V(k)$ and calculates $S(k)$ from Eq. (2.44). Subsequently, one calculates $\omega_{\rm ind}(k)$ and $g(r)$ from Eqs. (2.46) and (2.47). Finally, one calculates $V_{\rm ph}(r)$ from Eq. (2.45), and substitutes its Fourier transformation $V_{\rm ph}(k)$ to Eq. (2.44).

In 1954 Feynman proposed a specific ansatz for the excited-state wave function, namely $\Psi_{\mathbf{k}} = \rho_{\mathbf{k}}\Psi_0$. Here Ψ_0 is the ground-state wave function and $\rho_{\mathbf{k}} = \sum_j \exp(i\mathbf{k}\cdot\mathbf{r}_j)$ is a density fluctuation operator, where $\mathbf{r}_j$ is the position vector of the jth atom. This ansatz leads to the dispersion relation [58, 49]

$$\epsilon_{\rm F}(k) = \frac{\hbar^2 k^2}{2mS(k)}, \tag{2.48}$$

where the subindex F stands for Feynman. It is easy to see that the Feynman spectrum $\epsilon_{\rm F}(k)$ is easy to calculate after $S(k)$ has been determined.

2.3 Marchenko inversion

One can determine the s-wave phase shift $\delta(k)$ from the on-shell T-matrix $\langle k|T(k)|k\rangle$. However, the two-body potential $V(r)$ needed for the HNC equations is unknown. Consequently, we need to employ inverse scattering theory in order to find $V(r)$.

The Levinson theorem [59] says that a bound state causes a π phase shift. That is, $\lim_{k\to\infty}\delta(k) - \delta(0) = n\pi$, where n is the number of bound states. In addition, Levinson has shown that if there are no bound states, a given phase shift $\delta(k)$ determines a unique potential within the class of potentials satisfying [59, 60]

$$\int_0^\infty r|V(r)|\,dr \;<\; \infty, \tag{2.49}$$

$$\int_0^\infty r^2|V(r)|\,dr \;<\; \infty. \tag{2.50}$$

For fixed angular momentum, there are two fundamental inversion equations of interest, namely Gel'fand-Levitan and Marchenko [61, 62]. The Marchenko equation reads

$$K(r,s) + F(r,s) + \int_r^\infty K(r,t)F(t,s)\,dt = 0, \tag{2.51}$$

where $F(r,s)$ and $K(r,s)$ are called the input and output kernel, respectively. The input kernel is defined in terms of the S-matrix $S_l(k) = \exp[2i\delta_l(k)]$. [Note that S-matrix $S_l(k)$ and static structure function $S(k)$ are different quantities.]. For s-wave scattering, the input kernel is given by

$$F(r,s) = \frac{1}{2\pi}\int_{-\infty}^\infty h_0^+(kr)\,[1 - S_0(k)]\,h_0^+(ks)\,dk, \tag{2.52}$$

where $h_0^+(\cdot)$ are outgoing s-wave Riccati-Hankel functions. After solving the ouput kernel $K(r,s)$ from the Marchenko equation, the energy independent local potential $V(r)$ is obtained via the relation

$$V(r) = -2\frac{d}{dr}K(r,r). \tag{2.53}$$

We solve the Marchenko equation using the method from Ref. [61], and let us next summarize that method as in Publication III. First we fit the phase shift with a rational function

$$\delta(k) = \frac{\sum_{n=1}^{N/2} a_{2n-1}k^{2n-1}}{1 + \sum_{n=1}^{N/2} b_{2n}k^{2n}}, \tag{2.54}$$

where $N \in \{2, 4, 6, \cdots\}$. Next, we cast the S-matrix $S_l(k) = \exp[2i\delta_l(k)]$ into rational form. We do that by employing the Padé approximation

$$e^z = \frac{\sum_{l=0}^{L} a_l z^l}{\sum_{l=0}^{L} a_l (-z)^l} = 1 - \sum_{l=1}^{L} \frac{E_l}{z - \epsilon_l}, \tag{2.55}$$

where $a_l = (2L - l)!/(l!(L - l)!)$ and E_l are constants. The constants $\{\epsilon_1, \cdots, \epsilon_L\}$ are roots of the polynomial appearing in the denominator, and it is easy to see that they appear in conjugate pairs. Applying the Padé approximation to $S_l(k) = \exp[2i\delta_l(k)]$, we obtain

$$S_0(k) = \frac{\sum_{l=0}^{L} a_l [2i\delta(k)]^l}{\sum_{l=0}^{L} a_l [-2i\delta(k)]^l} = 1 - \sum_{m=1}^{M} \frac{S_m}{k - \sigma_m}, \tag{2.56}$$

where σ_m are roots of the denominator. That is, roots of the equations $2i\delta(k) = \epsilon_l$, where $l \in \{1, \cdots, L\}$. Since $\delta(k)$ is now a rational function, these equations are easy to solve. Moreover, since the order of $\delta(k)$ is N, the total number of roots σ_m is $M = L \times N$.

From Eq. (2.56) it follows that the S-matrix can be written as a rational polynomial

$$S_0(k) = \frac{\prod_{i=1}^{M} (k + \sigma_i)}{\prod_{i=1}^{M} (k - \sigma_i)}. \tag{2.57}$$

By matching Eq. (2.56) to (2.57) at $k = \sigma_m$, we obtain the pole strengths

$$S_m = -2\sigma_m \prod_{\substack{i=1 \\ i \neq m}}^{M} \frac{\sigma_m + \sigma_i}{\sigma_m - \sigma_i}. \tag{2.58}$$

By using Eq. (2.57), we cast the input kernel (2.52) into form

$$\begin{aligned} F(r, s) &= \frac{1}{2\pi} \int_{-\infty}^{\infty} h_0^+(kr) \left[\sum_{m=1}^{M} \frac{S_m}{k - \sigma_m} \right] h_0^+(ks)\, dk \\ &= i \sum_{m}^{(+)} S_m h_0^+(\sigma_m r) h_0^+(\sigma_m s), \end{aligned} \tag{2.59}$$

where $\sum_m^{(+)}$ means summation over the poles located in the upper half of the complex plane. For the output kernel we use the ansatz

$$K(r, s) = \sum_{m}^{(+)} \Psi(m, r) h_0^+(\sigma_m s). \tag{2.60}$$

By substituting Eqs. (2.59) and (2.60) into the Marchenko equation (2.51),

we obtain

$$\sum_m^{(+)} h_0^+(\sigma_m s)\left[\Psi(m,r) + iS_m h_0^+(\sigma_m r) + iS_m \sum_n^{(+)} M_{m,n}(r)\Psi(n,r)\right] = 0, \quad (2.61)$$

where

$$M_{m,n}(r) = \int_r^\infty h_0^+(\sigma_m t) h_0^+(\sigma_n t)\, dt. \quad (2.62)$$

The linear independence of the Riccati-Hankel functions $h_0^+(\sigma_m s)$ implies a system of $M/2$ linear equations for the $\Psi(n,r)$. The system of equations reads

$$\sum_n^{(+)} \left[\delta_{mn} + iS_m M_{m,n}(r)\right] \Psi(n,r) = -iS_m h_0^+(\sigma_m r), \quad (2.63)$$

where m goes over all the $M/2$ values for which σ_m lies in the upper half of the complex plane. It is easy to solve the values $\Psi(n,r)$ for any fixed r. After solving the functions $\Psi(n,r)$, we obtain the output kernel $K(r,s)$ by using Eq. (2.60). Subsequently, the potential $V(r)$ can be calculated by using Eq. (2.53).

2.4 Review of Publications I-III

In Publications I-III we analyzed a Bragg scattering experiment reported in Ref. [63]. In Publication I, we fit the observed excitation spectrum with ad-hoc potentials, but that approach did not take into account the presence of the molecular Feshbach resonance state. In Publications II and III we improved our model by using a T-matrix formalism for the Feshbach resonance, which allowed us to calculate the energy of the molecular Feshbach resonance state.

2.4.1 Motivation to potential scaling

Let us consider zero-energy s-wave scattering from a spherically symmetric potential

$$V(r) = \frac{\hbar^2}{m(\alpha a_0)^2} v(r/(\alpha a_0)), \quad (2.64)$$

where $\alpha > 0$ is a dimensionless parameter and $a_0 > 0$ is a constant with the dimension of length. The function $v : [0,\infty) \to \mathbb{R}$ gives the form of

$V(r)$ and the role of the dimensionless parameter α is to scale the range and strength of the potential $V(r)$ so that they are proportional to α and $1/\alpha^2$, respectively.

The time-independent Schrödinger equation reads

$$-\frac{\hbar^2\nabla_r^2\psi(r)}{m}+\frac{\hbar^2 v(r/(\alpha a_0))}{m(\alpha a_0)^2}\psi(r)=0. \tag{2.65}$$

In order to cast Eq. (2.65) into different form, we define $R=r/(\alpha a_0)$ and $\tilde{\psi}(R)=\psi(r)$. Subsequently, we obtain

$$-\nabla_R^2\tilde{\psi}(R)+v(R)\tilde{\psi}(R)=0. \tag{2.66}$$

The long-range asymptotic behavior of the scattering wave function is [2]

$$\tilde{\psi}(R)\sim 1-\frac{\tilde{a}}{R}, \tag{2.67}$$

where $\tilde{a}$ is a constant. Since $\psi(r)=\tilde{\psi}(r/(\alpha a_0))$, we obtain

$$\psi(r)\sim 1-\frac{\alpha a_0\tilde{a}}{r}. \tag{2.68}$$

Thus, the scattering length of potential $V(r)$ is $a=\alpha a_0\tilde{a}$. That is, the scattering length of $V(r)$ is directly proportional to α.

2.4.2 Potential scaling with scattering length

Let us say that $V_0(r)$ is a fixed potential whose scattering length we denote by a_0. We define a new function $v(\cdot)$ by saying that

$$v(r/a_0)=V_0(r)/\frac{\hbar^2}{ma_0^2}. \tag{2.69}$$

Let us say that $\alpha>0$ and define a new potential

$$U(r)=\frac{\hbar^2}{m(\alpha a_0)^2}v(r/(\alpha a_0)). \tag{2.70}$$

We note that $U(r)$ is of the form (2.64). Thus, the scattering length a of potential $U(r)$ is directly proportional to the parameter α. On the other hand, by using Eq. (2.69) we obtain

$$U(r)=\frac{1}{\alpha^2}V_0(r/\alpha). \tag{2.71}$$

From Eq. (2.71) it is clear that $a = a_0$ when $\alpha = 1$. Consequently, $a = \alpha a_0$ and we can write

$$U(r) = \frac{\hbar^2}{ma^2} v(r/a). \tag{2.72}$$

To recapitulate, we started from a fixed potential $V_0(r)$ whose scattering length we denoted by a_0. Subsequently, we constructed a potential $U(r)$ that has the same form as $V_0(r)$, but whose scattering length a is an adjustable parameter. Moreover, the range and strength of the new potential $U(r)$ scale as a and $1/a^2$, respectively.

Example: step-well potential
Let us say that

$$V(r) = \begin{cases} V_1, & r \leq r_1 \\ -V_2, & r_1 < r \leq r_2 \\ 0 & r > r_2, \end{cases} \tag{2.73}$$

where the constants r_1 and r_2 have the dimension of length and constants V_1 and V_2 have the dimension of energy. Furthermore, we assume that $0 < r_1 < r_2$ and $V_1, V_2 > 0$. We call a potential of the form $V(r)$ a *step-well potential*. A schematic illustration of a step-well potential is given in Fig. (2.1).

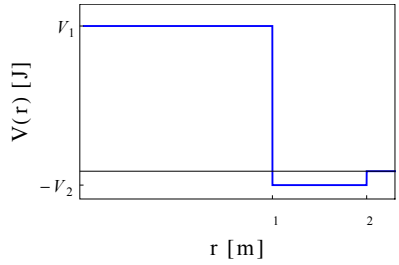

Figure 2.1. Schematic representation of a step-well potential.

In Publication I we used a step-well potential having the scaling property described in section 2.4.2. First, we defined a fixed step-well potential whose scattering length we will now denote by a_0. With the help of the scattering length a_0 that potential could be written as

$$V(r) = \begin{cases} 0.0554\frac{\hbar^2}{ma_0^2}, & r \leq 4.685a_0 \\ -0.0053\frac{\hbar^2}{ma_0^2}, & 4.685a_0 < r \leq 7.028a_0 \\ 0 & r > 7.028a_0. \end{cases} \tag{2.74}$$

Subsequently, we constructed the potential $v(r/a_0)$ in accordance with Eq. (2.69). We obtained

$$v(r/a_0) = \begin{cases} 0.0554, & r/a_0 \leq 4.685 \\ -0.0053, & 4.685 < r/a_0 \leq 7.028 \\ 0 & r/a_0 > 7.028. \end{cases} \tag{2.75}$$

That is,

$$v(r/a_0) = \begin{cases} 0.0554, & r \leq 4.685 a_0 \\ -0.0053, & 4.685 a_0 < r \leq 7.028 a_0 \\ 0 & r > 7.028 a_0. \end{cases} \tag{2.76}$$

The potential $v(r/a_0)$ defined in Eq. (2.76) is shown in Fig. 2.2.

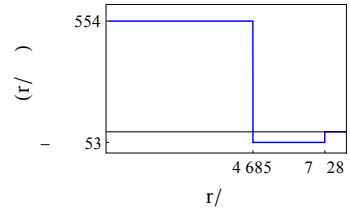

Figure 2.2. Potential $v(r/a_0)$ calculated from a certain step-well potential $V(r)$.

Finally, we formed the potential $U(r)$ according to Eq. (2.72). The resulting potential

$$U(r) = \begin{cases} 0.0554 \frac{\hbar^2}{ma^2}, & r \leq 4.685 a \\ -0.0053 \frac{\hbar^2}{ma^2}, & 4.685 a < r \leq 7.028 a \\ 0 & r > 7.028 a. \end{cases} \tag{2.77}$$

is shown in Fig. 2.3.

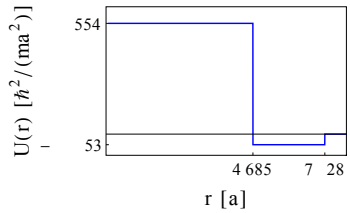

Figure 2.3. Potential $U(r)$ defined in Eq. (2.77). We note that the range and strength of $U(r)$ scale as a and $1/a^2$, respectively. Furthermore, the scattering length of $U(r)$ is a.

2.4.3 Summary of Publication I

The motivation for Publications I, II and III is a Bragg spectroscopy measurement reported in Ref. [63]. In their experiment, Papp et al. studied a ^{85}Rb Bose-Einstein condensate, which is a strongly interacting bosonic superfluid. Traditionally, experimental studies of bosonic superfluids have been carried out on liquid helium, but a gas of Bose-condensed atoms has the advantage that the interparticle interactions can be tuned via Feshbach resonance. In other words, the scattering length a can be tuned by using the Feshbach resonance.

In the experiment, Bragg pulses caused excitations of energy $\hbar\omega(k)$ with momentum $\hbar k$ above a BEC of homogeneous density n. Subsequently, the question was how to explain the observed excitation spectrum, because existing models relied on the smallness of a and k. To be more precise, existing models relied on the smallness of the following three parameters: (1) $\sqrt{8\pi n a^3} << 1$, so that interactions can be treated within the mean-field approximation; (2) $ka << 1$, so that the two-body scattering amplitude is momentum independent; (3) $1/(k\xi) << 1$, where $\xi = \hbar/(2m\mu)^{1/2}$ is the healing length. This limit corresponds to the excitation being cleanly in the free-particle regime. However, the experiment had pushed into a regime where $\sqrt{8\pi n a^3} \approx 0.4$ and $1/(k\xi) \approx 0.5$ and $ka \approx 0.8$. Thus, existing theoretical models could not be used to explain the results.

Variational many-body theory has been successfully used to describe the traditional bosonic superfluid, namely liquid ^{4}He [49, 64, 48]. The only inputs needed to calculate the Feynman spectrum $\epsilon_{\rm F}(k)$ are the two-body interaction $V(r)$ and the mass m of the bosons. Thus, if we knew the two-body interaction between the bosons, we could calculate the Feynman spectrum $\epsilon_{\rm F}(k)$ and compare the result with the observed energies $\hbar\omega(k)$. However, the complication arises from the fact that the two-body interaction is now inherently spin-dependent due to the Feshbach resonance, whereas we would like to construct a simple model where the two-body potential entering the variational many-body theory would be spin-independent.

In order to circumvent the problem, we decided to represent the spin-dependent two-body interaction with an effective spin-independent potential. In Publication I we used ad-hoc potentials with the scaling property discussed in section 2.4.2. For example, we used the step-well potential given in Eq. (2.77).

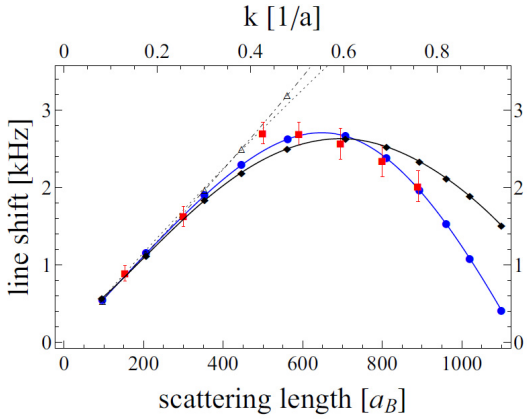

Figure 2.4. (Reprinted with permission from Publication I.) Line shift $\hbar\Delta(k) = \epsilon_{\mathrm{F}}(k) - \hbar^2k^2/2m$ as a function of scattering length at the value $k = 4\pi/(780\,\mathrm{nm})$ used in the experiment. Red squares indicate the experimental results, blue dots correspond to the step-well potential (2.77) and black squares indicate a soft-sphere result. Also shown are hard-core (triangles) and pseudopotential (dotted) results.

Red squares in Fig. 2.4 show the line shift $\hbar\Delta(k) = \hbar\omega(k) - \hbar^2k^2/2m$ as a function of scattering length at the value $k = 4\pi/(780\,\mathrm{nm})$ used in the experiment. That is, the line shift $\hbar\Delta(k)$ is the measured excitation energy $\hbar\omega(k)$ minus free particle energy $\hbar^2k^2/m$. For the theoretical curves, this means that $\hbar\Delta(k) = \epsilon_{\mathrm{F}}(k) - \hbar^2k^2/2m$. For example, triangles indicate the result for a hard-core potential, and we note that a hard-core potential fails to predict the downward bending of the line shift. Similarly, the dotted pseudopotential $(4\pi a\hbar^2/m)\delta(\mathbf{r})$ fails at large scattering lengths. On the other hand, the blue line shows the line shift for the step-well potential given in Eq. (2.77). We immediately note that the step-well potential predicts the downward bending of the line shift at large scattering lengths. Moreover, the diamonds correspond to a soft-sphere potential that has the same scaling property as the step-well potential, and the soft-sphere potential also predicts the downward bending of the line shift. Thus, potentials with the scaling property are able to predict the downward bending of the line shift at large scattering lengths, whereas traditionally used potentials like hard-core potential or pseudopotential fail even qualitatively at large scattering lengths.

2.4.4 Summary of Publications II and III

In Publication I, we were able to predict the downward bending of the line shift by using ad-hoc potentials with the scaling property. However, there was no way to predict the energy of the molecular state with these

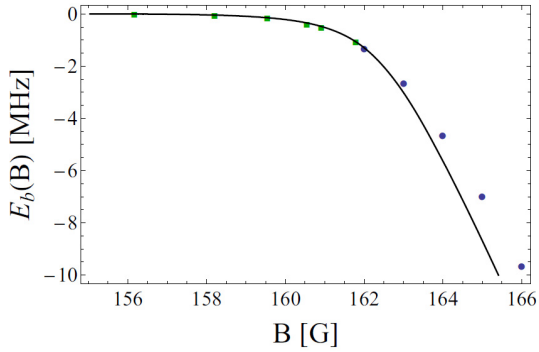

Figure 2.5. (Reprinted with permission from Publication I.) Bound state energy of the ^{85}Rb molecular Feshbach resonance state. Solid line corresponds to the result $E = -E_{\rm B}$ calculated from Eq. (2.37) with the step-function cutoff given in Eq. (2.78). Squares indicate experimental results from Ref. [65] and solid circles indicate full coupled-channel results from Ref. [66].

potentials. Therefore we decided to employ the T-matrix formalism of Feshbach-resonance discussed in section 2.1. Traditionally, one has used simple cutoff functions like the step function, and they predict e.g. the energy of the molecular state with good accuracy. For example, the solid molecular energy curve in Fig. 2.5 corresponds to the cutoff function

$$f(k) = \begin{cases} 1 & \text{if} \quad k \leq K \\ 0 & \text{if} \quad k > K, \end{cases} \tag{2.78}$$

where $K = 1/(110\, a_B)$. We note that the solid curve is in good agreement with the experimental results and the full coupled-channel calculations. However, as shown in Publication I, a simple cutoff function like (2.78) does not predict the downward bending of the line shift.

In Publications II and III we constructed a cutoff function $f(k)$ that has a scaling property similar to the ad-hoc potentials of Publication I. That is, we introduced a cutoff function of the form

$$f(k) = [1 - (1 - ca k^2)] \exp(-k^2 a^2/\bar{K}^2), \tag{2.79}$$

where c and $\bar{K}$ are constants and a is the scattering length. Letting $\bar{k}$ be a dimensionless variable, we immediately see that

$$f(\bar{k}/a) = [1 - (1 - (c/a)\bar{k}^2)] \exp(-\bar{k}^2/\bar{K}^2). \tag{2.80}$$

That is, the range of the momentum space cutoff function is proportional to $1/a$. To be more precise, the c/a-term contains explicit scattering length dependence, but it vanishes when a is large. Since $E_{\rm B} = \hbar^2/(ma^2)$ at large

a, Eq. (2.37) reduces to an integral condition

$$\frac{2}{\pi}\int_0^\infty \frac{f^2(\bar{k}/a)\,d\bar{k}}{1+\bar{k}^2} = 1 \tag{2.81}$$

at the limit $a \to \infty$. From this integral condition it follows that $\bar{K} = 2.586$.

The purpose of the parameter c is to be a phenomenological fitting parameter that accounts for the nonuniversal behavior of the molecular bound state energy at lower values of a. In Figure 1 of Publication II the parameter c has been fitted to experimentally and theoretically determined molecular bound state energies of ^{85}Rb, ^{87}Rb, and ^{23}Na, and our results are in good agreement with the reference results. For ^{85}Rb we found the best bound state energy fit with $c = 60a_B$. Therefore c/a is small at $a > 500a_B$, which is the regime where the downward bending of the line shift is observed in the Bragg scattering measurement [63].

Figure 2.6a shows the phase shift calculated from Eq. (2.36) with the cutoff function (2.79). The black dashed curve in Fig. 2.6a gives the phase shift for ^{85}Rb at $a = 1050a_B$, and the red curve gives the phase shift at the limit $a \to \infty$. Figure 2.6b shows the potentials corresponding to phase shift curves in Fig. 2.6a. The potentials were determined by using the Marchenko inversion. We note that the black dashed potential curve corresponding to ^{85}Rb at $a = 1050a_B$ is close to the universal potential curve depicted with red.

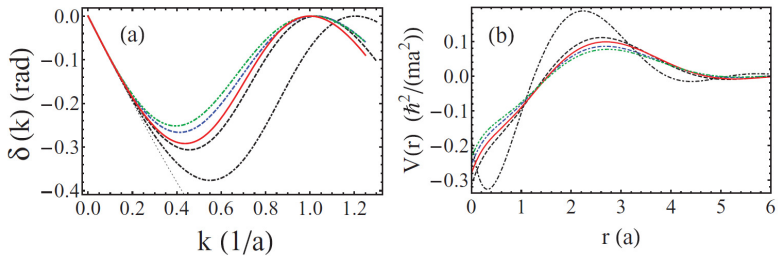

Figure 2.6. (Reprinted with permission from Publication II.) a) The black dashed curve indicates the phase shift for ^{85}Rb at $a = 1050a_B$, and the red curve is the universal phase shift obtained at the limit $a \to \infty$. Also shown are ^{87}Rb (blue double-dash-dotted curve) and ^{23}Na (green dash-double-dotted curve) results at $|B - B_0|/\Delta B = 0.3$. The dotted curve is the contact interaction result, and the black dash-dotted curve is the ^{85}Rb result at $|B - B_0|/\Delta B = 0.3$. The phase shifts were calculated from Eq. (2.36) with the cutoff function (2.79). b) Potentials corresponding to the phase shift curves depicted in subfigure a. At the limit $a \to \infty$ all the potential curves converge to the universal curve depicted in red.

Figure 2.7 is similar to Fig. 2.4. However, the black circles in Fig. 2.7 stand for the ^{85}Rb results obtained with the cutoff function 2.79. That is, first we calculated the phase shift $\delta(k)$ for all relevant values of a from

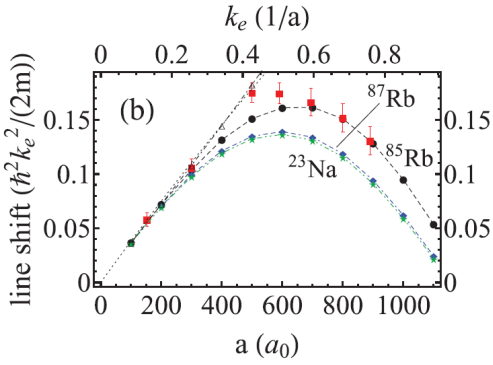

Figure 2.7. (Reprinted with permission from Publication II.) Line shift as a function of scattering length. Red squares indicate the experimental results [63], and black circles stand for the theoretical ^{85}Rb result obtained with the cutoff function 2.79. The green and blue curves are the corresponding results for ^{23}Na and ^{87}Rb, respectively. Also shown are hard-sphere (dash-dotted curve) and pseudopotential (dotted curve) results.

Eq. (2.36). After that, we determined the corresponding potentials $V(r)$ by using the Marchenko inversion. Finally, we used those potentials $V(r)$ in the variational many-body theory to calculate the line shifts. We see that our theoretical prediction for ^{85}Rb is in good agreement with the experimental results. In particular, our model predicts the downward bending of the line shift at large scattering lengths.

2.5 A note on molecular Feshbach resonance state energies

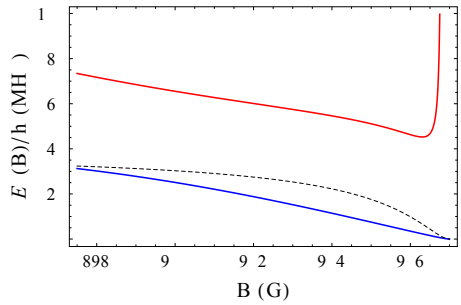

Figure 2.8. Blue and red line indicate the binding energies of ^{23}Na molecular Feshbach resonance states near $B_0 = 907\,\mathrm{G}$ resonance. The curves have been calculated from Eq. (2.37). Dashed line indicates the universal result $E_\mathrm{B} = \hbar^2/(ma(B)^2)$. Note the unphysical diverging behavior of the deeply bound molecular state.

I calculated the molecular state binding energies for ^{23}Na near the $B_0 = 907\,\mathrm{G}$ resonance with the parameter values given in Ref. [67]. There turned out to be two molecular states as shown in Fig. 2.8. Generally speaking, the existence of two molecular states is not a problem, and such

situations are discussed e.g. in Ref. [68]. However, as Fig. 2.8 shows, the binding energy of the second molecular state diverges when $B \to 906.8\,\mathrm{G}$. Furthermore, when $906.8\,\mathrm{G} < B < B_0 = 907\,\mathrm{G}$, the second molecular state does not exist. This diverging and vanishing behavior of the molecular binding energy is caused by the scaling property of the cutoff function and it is clearly unphysical. Moreover, this problem appears in the universal region where the model is supposed to be valid. However, the molecular energies for ^{85}Rb are well-behaved.

3. Fermionic quantum gases

Fermions, such as protons, electrons and neutrons, compose all of the matter around us, and therefore phenomena arising from the quantum degeneracy of fermions are ubiquitous. For example, the Pauli exclusion principle is a central piece of modern condensed matter theory. However, naturally occurring Fermi systems are usually dense and strongly interacting, and their properties are hard to control.

The achievement of Fermi degeneracy in an ultracold gas of ^{40}K atoms [21] opened a new chapter in the study of fermionic quantum systems. This experiment by DeMarco and Jin made it possible to study a low-density fermion system allowing a high level of control over the interparticle interactions. For example, Feshbach resonances could be used to tune the interactions between particles. Moreover, fermions in an optical lattice allow one to realize a highly tunable version of the (extended) Fermi-Hubbard Hamiltonian. Thus, owing to the high level of controllability, fermions in optical lattices can be used to study a variety of open problems in condensed matter physics, e.g. high temperature superconductivity.

3.1 Extended Fermi-Hubbard model

3.1.1 Fermi-Hubbard model

For deep enough lattice potentials, the atomic motion is determined by tunneling between adjacent sites. In the lowest band, direct tunneling to next-nearest-neighbors is typically suppressed by an order of magnitude when compared to tunneling between neighboring sites [69, 70]. In most experiments, the Fermi gas is prepared in a mixture of two spin states. Since particles of opposing spin can reside at the same lattice site, their

collisions give rise to an on-site interaction. With all atoms prepared in the lowest band, this concept leads to the Hubbard Hamiltonian. For a two-component Fermi gas in an optical lattice, the Hubbard Hamiltonian reads

$$H_{\mathrm{FH}} = -t \sum_{\langle i,j\rangle\sigma} (c^{\dagger}_{i\sigma} c_{j\sigma} + \mathrm{h.c.}) + U \sum_{i} \hat{n}_{i,\uparrow}\hat{n}_{i,\downarrow} + \sum_{i\sigma} \epsilon_i \hat{n}_{i,\sigma}. \tag{3.1}$$

The first term contains the kinetic energy and is proportional to the tunneling matrix element t between adjacent lattice sites, and $\langle i,j\rangle$ denotes neighboring sites. The operators $c^{\dagger}_{i\sigma}$ and $c_{i\sigma}$ are, respectively, fermionic creation and annihilation operators for a particle with spin $\sigma \in \{\uparrow,\downarrow\}$ at site i. The occupation number operator is given by $\hat{n}_{i,\sigma} = c^{\dagger}_{i\sigma} c_{i\sigma}$. The second term in Eq. (3.1) describes the interaction energy in the system, and is determined by the on-site interaction U. The last term takes into account the possible presence of an additional atom trap, which is usually harmonic. The corresponding energy offset of the lattice site with index i is given by ϵ_i.

3.1.2 Extended Fermi-Hubbard model

In analogy with the on-site interaction term in Eq. (3.1), we write down a nearest-neighbor interaction term

$$H_{\mathrm{nn}} \;=\; -V \sum_{\sigma} \sum_{\langle m,n\rangle} c^{\dagger}_{m,\sigma} c_{m,\sigma} c^{\dagger}_{n,-\sigma} c_{n,-\sigma}, \tag{3.2}$$

which accounts for spin-singlet pairing between distinct nearest-neighbors $\langle m,n\rangle$. Subsequently, the extended Fermi-Hubbard Hamiltonian

$$H = H_{\mathrm{FH}} + H_{\mathrm{nn}}. \tag{3.3}$$

Nearest-neighbor interaction H_{nn} in mean-field approximation
Using fermionic anticommutation relations, one easily obtains

$$H_{\mathrm{nn}} = -V \sum_{\sigma} \sum_{\langle m,n\rangle} c^{\dagger}_{m,\sigma} c^{\dagger}_{n,-\sigma} c_{n,-\sigma} c_{m,\sigma}. \tag{3.4}$$

In the mean-field approximation of the on-site interaction term we will neglect the Hartree shifts because they can be incorporated into the chemical potentials and on-site energy modulation terms [71]. In the same

spirit, we will neglect the Hartee shifts in the mean-field approximation of the nearest-neighbor interaction term. Thus, we obtain

$$H_{\rm nn}^{\rm MF} = -V \sum_{\sigma} \sum_{\langle m,n \rangle} \langle c_{n,-\sigma} c_{m,\sigma} \rangle c_{m,\sigma}^{\dagger} c_{n,-\sigma}^{\dagger} + \text{h.c.} - |\langle c_{n,-\sigma} c_{m,\sigma} \rangle|^2. \tag{3.5}$$

Since we consider spin-singlet pairing, we assume that the order parameter $\langle c_{n\uparrow} c_{m\downarrow} \rangle = -\langle c_{n\downarrow} c_{m\uparrow} \rangle$. Thus, we obtain

$$H_{\rm nn}^{\rm MF} = -V \sum_{\langle m,n \rangle} \langle c_{n\downarrow} c_{m\uparrow} \rangle (c_{m\uparrow}^{\dagger} c_{n\downarrow}^{\dagger} - c_{m\downarrow}^{\dagger} c_{n\uparrow}^{\dagger}) + \text{h.c.} - 2|\langle c_{n\downarrow} c_{m\uparrow} \rangle|^2. \tag{3.6}$$

With the help of the spin-singlet creation operator

$$\hat{h}_{mn}^{\dagger} = (\hat{c}_{m\uparrow}^{\dagger} \hat{c}_{n\downarrow}^{\dagger} - \hat{c}_{m\downarrow}^{\dagger} \hat{c}_{n\uparrow}^{\dagger})/\sqrt{2} \tag{3.7}$$

we cast Eq. (3.6) into the form

$$H_{\rm nn}^{\rm MF} = -V \sum_{\langle m,n \rangle} \sqrt{2} \langle c_{n\downarrow} c_{m\uparrow} \rangle \hat{h}_{mn}^{\dagger} + \sqrt{2} \langle c_{n\downarrow} c_{m\uparrow} \rangle^* \hat{h}_{mn} - 2|\langle c_{n\downarrow} c_{m\uparrow} \rangle|^2, \tag{3.8}$$

where $*$ denotes complex conjugation. In conclusion, we note that nearest-neighbor interaction of this type has been discussed, for instance, in Ref. [72]. Furthermore, see e.g. Refs. [43, 44] for a model that assumes spin-singlet pairing and is similar to the one in Publication IV.

3.2 BCS theory

The Bardeen-Cooper-Schrieffer theory is the first microscopic theory of superconductivity [73]. It was developed in 1957, and it describes superconductivity as an effect caused by Cooper pairs. Since the theory successfully explains the properties of conventional superconductors, John Bardeen, Leon Neil Cooper and Robert Schrieffer were awarded the Nobel Prize in Physics in 1972. Let us next present the standard formulation of the BCS theory in an infinite one-dimensional lattice (see, for instance, Ref. [74]).

We start from a Fermi-Hubbard Hamiltonian, which now contains a chemical potential term μ. The chemical potential term describes the energy cost of adding one particle into the system, and it is needed to fix the average number of particles because the mean-field approximation made in the BCS theory breaks the conservation of particle number. Thus, the

Fermi-Hubbard Hamiltonian reads

$$H = -t\sum_{j\sigma}(\hat{c}^\dagger_{j\sigma}\hat{c}_{j+1,\sigma} + \text{h.c.}) - \mu\sum_j(\hat{n}_{j\uparrow} + \hat{n}_{j\downarrow}) - U\sum_j \hat{n}_{j\uparrow}\hat{n}_{j\downarrow}. \tag{3.9}$$

Next, let us diagonalize the Fermi-Hubbard Hamiltonian in order to find out the excitation spectrum (eigenvalues and eigenvectors). Excluding the interaction term, the Hamiltonian is easy to diagonalize. However, the interaction term poses a problem because it is quartic. To be more precise, a simple two-site system can be easily solved analytically, but even supercomputers cannot exactly diagonalize Fermi-Hubbard Hamiltonians that have a large number of lattice sites, not to mention lattices with a macroscopic number of sites. Indeed, one is usually interested in superfluids that have a macroscopic number of particles and lattice sites, and therefore one has to approximate the interaction term in some way that makes it computationally less cumbersome. There are two approximations in BCS, and the first one is the mean-field approximation of the interaction term. That is, the first approximation is

$$\begin{aligned} H_{\text{os}} &= -U\sum_j \hat{c}^\dagger_{j\uparrow}\hat{c}_{j\uparrow}\hat{c}^\dagger_{j\downarrow}\hat{c}_{j\downarrow} \\ &= \sum_j -U\langle\hat{c}^\dagger_{j\uparrow}\hat{c}^\dagger_{j\downarrow}\rangle\hat{c}_{j\downarrow}\hat{c}_{j\uparrow} - U\langle\hat{c}_{j\downarrow}\hat{c}_{j\uparrow}\rangle\hat{c}^\dagger_{j\uparrow}\hat{c}^\dagger_{j\downarrow} + U\langle\hat{c}^\dagger_{j\uparrow}\hat{c}^\dagger_{j\downarrow}\rangle\langle\hat{c}_{j\downarrow}\hat{c}_{j\uparrow}\rangle, \end{aligned} \tag{3.10}$$

where one has neglected the Hartree $\langle\hat{c}^\dagger_{j\sigma}\hat{c}_{j\sigma}\rangle$ and Fock $\langle\hat{c}^\dagger_{j,\sigma}\hat{c}_{j,-\sigma}\rangle$ terms. Furthermore, one has introduced the BCS mean-field order parameter $\Delta_j = U\langle\hat{c}^\dagger_{j\uparrow}\hat{c}^\dagger_{j\downarrow}\rangle$, which is assumed to be real-valued. Subsequently, the total Hamiltonian becomes

$$\begin{aligned} H^{\text{MF}} &= -t\sum_j(\hat{c}^\dagger_{j\sigma}\hat{c}_{j+1,\sigma} + \text{h.c.}) - \mu\sum_j(\hat{n}_{j\uparrow} + \hat{n}_{j\downarrow}) \\ &\quad - \sum_j \Delta_j\hat{c}_{j\downarrow}\hat{c}_{j\uparrow} + \Delta^*_j\hat{c}^\dagger_{j\uparrow}\hat{c}^\dagger_{j\downarrow} + \sum_j\frac{\Delta_j^2}{U}. \end{aligned} \tag{3.11}$$

The Hamiltonian H^{MF} is analytically diagonalizable. However, in order to gain more physical insight, one Fourier transforms H^{MF} to the momentum space, and diagonalizes it there. One defines the inverse Fourier trans-

form as

$$\hat{c}_{j\sigma} = \frac{1}{\sqrt{M}} \sum_k e^{ikj} \hat{c}_{k\sigma}, \tag{3.12}$$

$$\hat{c}^\dagger_{j\sigma} = \frac{1}{\sqrt{M}} \sum_k e^{-ikj} \hat{c}^\dagger_{k\sigma}, \tag{3.13}$$

where M is the total number of lattice sites. Furthermore, when one transforms from r-space to k-space, one will also need the relation

$$\sum_j e^{-i(k-k')j} = L\delta_{k,k'}. \tag{3.14}$$

Transforming the chemical potential term, one obtains

$$-\mu \sum_j (\hat{n}_{j\uparrow} + \hat{n}_{j\downarrow}) = -\mu \sum_k (\hat{c}^\dagger_{k\uparrow}\hat{c}_{k\uparrow} + \hat{c}^\dagger_{k\downarrow}\hat{c}_{k\downarrow}). \tag{3.15}$$

For the hopping term one obtains

$$\begin{aligned} -t \sum_j \hat{c}^\dagger_{j\sigma}\hat{c}_{j+1,\sigma} &= -\frac{t}{M} \sum_{j,k,k'} \exp\left[i(j(k'-k)+k')\right] \hat{c}^\dagger_{k\sigma}\hat{c}_{k'\sigma} \\ &= -t \sum_k \exp\left[ik\right] \hat{c}^\dagger_{k\sigma}\hat{c}_{k\sigma}. \end{aligned} \tag{3.16}$$

Thus

$$-t \sum_{j\sigma} \hat{c}^\dagger_{j\sigma}\hat{c}_{j+1,\sigma} + \text{h.c.} = -2t \sum_{k\sigma} \cos(k) \hat{c}^\dagger_{k\sigma}\hat{c}_{k\sigma}. \tag{3.17}$$

Finally, for the interaction term one obtains

$$\begin{aligned} \sum_j \Delta_j \hat{c}_{j\downarrow}\hat{c}_{j\uparrow} &= \frac{1}{L} \sum_{j,k,k'} \Delta_j \exp\left[ij(k+k')\right] \hat{c}_{k\downarrow}\hat{c}_{k'\uparrow} \\ &= \Delta \sum_k \hat{c}_{k\downarrow}\hat{c}_{-k\uparrow}, \end{aligned} \tag{3.18}$$

where it is assumed that the order parameter $\Delta_i = \Delta$ is a constant, which is the second fundamental BCS assumption. The Hamiltonian in momentum space thus reads

$$\begin{aligned} H &= \sum_{k\sigma} [-2t(\cos(k)-1) - \tilde{\mu}] \hat{c}^\dagger_{k\sigma}\hat{c}_{k\sigma} \\ &\quad + \sum_k -\Delta \hat{c}_{k\downarrow}\hat{c}_{-k\uparrow} - \Delta^* \hat{c}^\dagger_{-k\uparrow}\hat{c}^\dagger_{k\downarrow} + \frac{\Delta^2}{U}, \end{aligned} \tag{3.19}$$

where one has defined $\tilde{\mu} = \mu + 2t$. This was done because the lattice dis-

persion $-2t(1-\cos(k))$ becomes proportional to the free space dispersion $\hbar^2k^2/(2m)$ in the limit of small momentum.

By diagonalizing the Hamiltonian (3.19), one obtains the eigenvalues E_k and $-E_k$, where

$$E_k = \sqrt{(\xi_k - \mu) + \Delta^2}. \tag{3.20}$$

Here $\xi_k = 2J(1-\cos k)$ and Δ is self-consistently determined from the so-called gap equation. One immediately notes that the minimum value E_k can have is Δ. In fact, to create an excitation in the system, a minimum energy of 2Δ is needed. This is the origin of superconductivity in BCS theory: if thermal energy $k_{\mathrm{B}}T << 2\Delta$, there are no dissipative single particle excitations at all. In such a situation, electricity can be conducted without resistance or fluid can flow without friction.

3.3 FFLO state

Two independent articles in 1960s, one by by Peter Fulde and Richard A. Ferrell [75] and the other by Anatoly Larkin and Yuri Ovchinnikov [76], predicted the existence of an imbalanced superfluid whose constituents have nonzero center-of-mass momentum. Here the term imbalanced means that the number of up-spin particles $N_\uparrow$ is not equal to the number of down-spin particles $N_\downarrow$. This superfluid phase is called Fulde-Ferrell-Larkin-Ovchinnikov (FFLO) phase after its inventors.

In contrast to the BCS theory, the order parameter in the FFLO state is not a constant. Instead, it is assumed to have an oscillating position dependence. We, however, consider an FF ansatz whose phase is position dependent but the overall amplitude is not. That is, we consider an ansatz

$$U\langle \hat{c}^\dagger_{j\uparrow}\hat{c}^\dagger_{j\downarrow}\rangle = \Delta \exp(2i\mathbf{x}_j \cdot \mathbf{q}), \tag{3.21}$$

where Δ is the amplitude of the order parameter, $\mathbf{x}_j$ is the position vector of lattice site j and $2\mathbf{q}$ is the Cooper pair center-of-mass momentum. Nevertheless, an FF ground state can be taken as an indicator of a more general FFLO state because in known cases LO states have lower energies than FF states. By employing Eq. (3.21) and Fourier transformation,

we obtain

$$\begin{aligned}\sum_j U\langle\hat{c}^\dagger_{j\uparrow}\hat{c}^\dagger_{j\downarrow}\rangle\hat{c}_{j\downarrow}\hat{c}_{j\uparrow} &= \sum_j \Delta\exp(2i\mathbf{x}_j\cdot\mathbf{q})\hat{c}_{j\downarrow}\hat{c}_{j\uparrow} \\ &= \sum_{\mathbf{k}} \Delta\hat{c}_{\mathbf{k}+2\mathbf{q}\downarrow}\hat{c}_{-\mathbf{k}\uparrow}. \end{aligned} \tag{3.22}$$

Physically, Eq. (3.22) means that the condensate constituents in FFLO phase have momenta $\mathbf{k}+2\mathbf{q}$ and $-\mathbf{k}$. That is, Cooper pairs in FFLO phase have center-of-mass momentum $2\mathbf{q}$. In addition to the change in the order parameter, spin-dependent chemical potentials ($\mu_\uparrow$ and $\mu_\downarrow$) must be introduced because the number of up-spin and down-spin particles is different ($N_\uparrow \neq N_\downarrow$). Anyhow, with these changes one can repeat the BCS analysis, and arrive at the mean-field FFLO theory. Simply, the FFLO state is an extension of the BCS state because it accounts for imbalance and Cooper pairing between nonopposite momenta.

Extensive studies of the FFLO state were triggered by the discovery of an interesting superconducting phase in the heavy fermion superconductor $CeCoIn_5$ [77, 78]. Possible FFLO states have also been discovered in some organic materials [79, 80]. Indeed, realizing the FFLO state has been a major goal since the creation of the first Fermi condensates, but unambiguous experimental evidence is still lacking [81]. Nevertheless, several methods have been proposed for the experimental detection of FFLO phase [82, 83, 84, 85, 81, 86]. Considering how ubiquitous phenomenon FFLO is in modern physics, its experimental observation even in a highly controlled environment such as an optical lattice could shed light on a number of open questions, e.g. high temperature superconductivity.

3.4 Two-dimensional lattices

3.4.1 Bravais lattices

Qualitatively speaking, a lattice is an arrangement of points that repeats over and over again [87]. In the simplest case, this means that the neighborhood of every point is the same. Such a simple lattice is called a Bravais lattice, and in two dimensions it is formally defined as a collection of points

$$\mathbf{R} = n_1\mathbf{a}_1 + n_2\mathbf{a}_2, \tag{3.23}$$

where n_1 and n_2 are integers and linearly independent vectors $\mathbf{a}_1$ and $\mathbf{a}_2$ are called primitive vectors. For each Bravais lattice, it is easy to see that the choice of primitive vectors is not unique, and usually the most convenient choice makes them as simple as possible or has some handy symmetry to them.

In two dimensions, there are a total of five Bravais lattices, which are enumerated below. The symmetries of all five lattices are given, and one notes that any Bravais lattice remains unchanged if all points are reflected about the origin. That is, all Bravais lattices possess the inversion symmetry $\mathbf{R} \to -\mathbf{R}$.

Square Lattice is spanned by the primitive vectors $\mathbf{a}_1 = a\begin{pmatrix}1 & 0\end{pmatrix}$ and $\mathbf{a}_2 = a\begin{pmatrix}0 & 1\end{pmatrix}$, where $a > 0$ is the lattice constant. Square lattice is symmetric under reflection about the x and y axes, and with respect to 90^o rotations.

Rectangular Lattice is obtained by compressing a square lattice along one axis. Thus, it is spanned by the primitive vectors $\mathbf{a}_1 = a_1\begin{pmatrix}1 & 0\end{pmatrix}$ and $\mathbf{a}_2 = a_2\begin{pmatrix}0 & 1\end{pmatrix}$, where $a_1, a_2 > 0$ are the lattice constants. Due to the compression, a rectangular lattice does not have the 90^o rotation symmetry.

Triangular Lattice is also known as the hexagonal lattice. It is spanned by the primitive vectors $\mathbf{a}_1 = a\begin{pmatrix}\sqrt{3}/2 & 1/2\end{pmatrix}$ and $\mathbf{a}_2 = a\begin{pmatrix}\sqrt{3}/2 & -1/2\end{pmatrix}$, where $a > 0$ is the lattice constant. It is invariant under reflections about the x and y axes, and with respect to 60^o rotations.

Centered Rectangular Lattice is obtained by compressing a triangular lattice. Thus, it is spanned by the primitive vectors $\mathbf{a}_1 = \begin{pmatrix}a_x & a_y\end{pmatrix}$ and $\mathbf{a}_2 = \begin{pmatrix}a_x & -a_y\end{pmatrix}$, where $a_x, a_y > 0$ are the lattice constants. Due to the compression, a centered rectangular lattice does not have the 60^o rotation symmetry.

Oblique lattice results from an arbitrary choice of primitive vectors $\mathbf{a}_1$ and $\mathbf{a}_2$ with no special symmetry. However, an oblique lattice still possesses the inversion symmetry $\mathbf{R} \to -\mathbf{R}$.

3.4.2 Primitive cell

Lattices are created by periodically repeating the same structural unit. The repeated structural unit is called a unit cell, and a unit cell having the smallest possible area is called a primitive unit cell [88]. However, primitive cells are not unique, and therefore it is valuable to have a standard way of constructing the primitive cell. Furthermore, it is valuable to have the primitive cell invariant under all symmetry operations that leave the lattice invariant. Such a construction is provided by the Wigner-Seitz unit cell, which is built by associating with each lattice point all of the space which is closer to it than any other lattice point [see Fig. 3.1(b)].

Clearly, a Wigner-Seitz unit cell is invariant under any transformation that leaves the lattice invariant, and therefore such a unit cell displays all the symmetries of the lattice. In practice, one constructs the Wigner-Seitz unit cell by finding perpendicular bisectors to all lattice vectors emerging from a given lattice point, and determining the area enclosed by them.

3.4.3 Reciprocal lattice

The reciprocal lattice is of fundamental importance in studies of periodic structures. For example, it is used in the theory of crystal diffraction, and in the study of functions having the periodicity of a Bravais lattice. In order to formally define reciprocal lattice, one considers a set of points $\mathbf{R}$ constituting a Bravais lattice, and a plane wave $e^{i\mathbf{k}\cdot\mathbf{r}}$. Obviously, for a general k the plane wave will not have the periodicity of the Bravais lattice. However, for certain special choices of k the plane wave $e^{i\mathbf{k}\cdot\mathbf{r}}$ will exhibit the periodicity of the Bravais lattice. The set of all wave vectors $\mathbf{K}$ that yield a plane wave with the periodicity of a given Bravais lattice is known as its reciprocal lattice. Analytically, $\mathbf{K}$ belongs to the reciprocal lattice of a given Bravais lattice $\mathbf{R}$ if [89]

$$e^{i\mathbf{K}\cdot(\mathbf{r}+\mathbf{R})} = e^{i\mathbf{K}\cdot\mathbf{r}} \tag{3.24}$$

for any $\mathbf{r}$, and for all $\mathbf{R}$ in the Bravais lattice. Cancelling out the common factor $e^{i\mathbf{K}\cdot\mathbf{r}}$, one can characterize the reciprocal lattice as a set of wave vectors $\mathbf{K}$ satisfying

$$e^{i\mathbf{K}\cdot\mathbf{R}} = 1 \tag{3.25}$$

for all $\mathbf{R}$ in a Bravais lattice.

Let us consider a Bravais lattice spanned by the three primitive vectors $\mathbf{a}_1$, $\mathbf{a}_2$ and $\mathbf{a}_3$. If the lattice is two-dimensional, one sets $\mathbf{a}_3$ perpendicular to the lattice plane. In order to construct the reciprocal lattice, one defines vectors

$$\begin{aligned}\mathbf{b}_1 &= 2\pi\frac{\mathbf{a}_2\times\mathbf{a}_3}{\mathbf{a}_1\cdot(\mathbf{a}_2\times\mathbf{a}_3)}\\ \mathbf{b}_2 &= 2\pi\frac{\mathbf{a}_3\times\mathbf{a}_1}{\mathbf{a}_2\cdot(\mathbf{a}_3\times\mathbf{a}_1)}\\ \mathbf{b}_3 &= 2\pi\frac{\mathbf{a}_1\times\mathbf{a}_2}{\mathbf{a}_3\cdot(\mathbf{a}_1\times\mathbf{a}_2)}.\end{aligned} \tag{3.26}$$

It is easy to see that $\mathbf{a}_i\cdot\mathbf{b}_j = 2\pi\delta_{ij}$, where δ_{ij} is the Kronecker delta symbol. In addition, any vector $\mathbf{k}$ can now be written as

$$\mathbf{k} = k_1\mathbf{b}_1 + k_2\mathbf{b}_2 + k_3\mathbf{b}_3, \tag{3.27}$$

where $k_i \in \mathbb{R}$. On the other hand, any vector belonging to the direct lattice can be written as

$$\mathbf{R} = n_1\mathbf{a}_1 + n_2\mathbf{a}_2 + n_3\mathbf{a}_3. \tag{3.28}$$

Thus

$$\mathbf{k}\cdot\mathbf{R} = 2\pi(k_1n_1 + k_2n_2 + k_3n_3). \tag{3.29}$$

For $e^{i\mathbf{k}\cdot\mathbf{R}}$ to be unity for all $\mathbf{R}$, the product $\mathbf{k}\cdot\mathbf{R}$ must be an integer multiple of 2π for all n_1, n_2 and n_3. This requires the coefficients k_i to be integers. Thus, the reciprocal lattice vectors are linear combinations of the vectors $\mathbf{b}_1$, $\mathbf{b}_2$ and $\mathbf{b}_3$ with integer coefficients. That is, the vectors $\mathbf{b}_1$, $\mathbf{b}_2$ and $\mathbf{b}_3$ are the primitive vectors of the reciprocal lattice.

Brillouin zone

The Wigner-Seitz primitive cell of the reciprocal lattice is known as the first Brillouin zone. For example, let us consider a triangular lattice spanned by the primitive vectors

$$\begin{aligned}\mathbf{a}_1 &= \begin{pmatrix}\sqrt{3}/2 & 1/2\end{pmatrix},\\ \mathbf{a}_2 &= \begin{pmatrix}\sqrt{3}/2 & -1/2\end{pmatrix}.\end{aligned} \tag{3.30}$$

The primitive vectors of the reciprocal lattice are given by Eq. (3.26). One obtains

$$\begin{aligned} \mathbf{b}_1 &= \left(2\pi/\sqrt{3} \quad 2\pi\right), \\ \mathbf{b}_2 &= \left(2\pi/\sqrt{3} \quad -2\pi\right). \end{aligned} \tag{3.31}$$

It is now easy to show that one would obtain $\mathbf{b}_1$ and $\mathbf{b}_2$ from $\mathbf{a}_1$ and $\mathbf{a}_2$ by rotating them by $\pi/6$ and scaling them with a factor $4\pi/\sqrt{3}$. Thus, the reciprocal lattice of a triangular lattice is a triangular lattice.

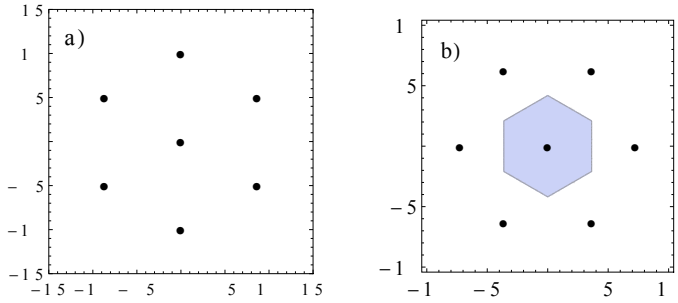

Figure 3.1. a) Triangular lattice spanned by primitive vectors (3.30). b) Reciprocal lattice spanned by primitive vectors (3.31). Also shown is the first Brillouin zone.

Figure 3.1(a) shows the triangular lattice spanned by primitive vectors (3.30), and Fig. 3.1(b) shows the corresponding reciprocal lattice spanned by primitive vectors (3.31). In addition, Fig. 3.1(b) shows the first Brillouin zone depicted in blue.

3.4.4 Wave function in a periodic potential

Let us consider a particle in a periodic potential $V(\mathbf{r})$, where $V(\mathbf{r}+\mathbf{R}) = V(\mathbf{r})$ for all $\mathbf{R}$ in a Bravais lattice. In passing, one notes that such a periodic potential could be provided e.g. by an optical lattice. Anyhow, according to the Bloch theorem, the energy eigenstates $\psi_{n\mathbf{k}}(\mathbf{r})$ of the particle can be labeled with a band index n and a crystal momentum $\mathbf{k}$ so that

$$\psi_{n\mathbf{k}}(\mathbf{r}+\mathbf{R}) = e^{i\mathbf{k}\cdot\mathbf{R}}\psi_{n\mathbf{k}}(\mathbf{r}), \tag{3.32}$$

for all $\mathbf{R}$ in the Bravais lattice [87, 89].

In theoretical considerations one usually assumes that a Bravais lattice is of infinite size. However, in numerical implementations one has to use lattices of finite size. Therefore one has to come up with some boundary

conditions for the wave function $\psi_{n\mathbf{k}}(\mathbf{r})$. Generally speaking, if one considers particles confined to a ring of circumference L, it is natural to impose the boundary condition $\psi(x+L) = \psi(x)$. Furthermore, if one considers particles confined to a cube with edge length L, one usually emphasizes the inconsequence of the surface by disposing of it altogether. That is done by imagining that each face of the cube is joined to its opposing face, so that a particle coming to the surface is not reflected back, but re-enters the cube from the opposite side. In equation form, these periodic boundary conditions read

$$\begin{aligned} \psi(x+L,y,z) &= \psi(x,y,z) \\ \psi(x,y+L,z) &= \psi(x,y,z) \\ \psi(x,y,z+L) &= \psi(x,y,z), \end{aligned} \tag{3.33}$$

where one assumes that $x, y, z \in [-L/2, L/2]$ i.e. x, y and z are inside or on the surface of the cube.

However, unless the Bravais lattice is cubic or square, it is no longer convenient to work in a cubic volume of side L. Nevertheless, one would still like to emphasize the inconsequence of the finite lattice size by a boundary condition analogous to (3.33). Therefore one generalizes (3.33) to the Born-von Karman boundary condition

$$\psi(\mathbf{r} + N_j\mathbf{a}_j) = \psi(\mathbf{r}), \quad j = 1,2,3, \tag{3.34}$$

where $\mathbf{a}_j$ are the three primitive vectors and N_j is the number of lattice points in the direction $\mathbf{a}_j$. Since N_j is the number of lattice points in the direction $\mathbf{a}_j$, the total number of lattice points is $N = N_1N_2N_3$.

From the Bloch theorem (3.32) one obtains

$$\psi_{n\mathbf{k}}(\mathbf{r} + N_j\mathbf{a}_j) = e^{i\mathbf{k}\cdot N_j\mathbf{a}_j}\psi_{n\mathbf{k}}(\mathbf{r}) \quad j = 1,2,3. \tag{3.35}$$

Imposing the boundary condition (3.34), one obtains

$$e^{i\mathbf{k}\cdot N_j\mathbf{a}_j} = 1 \quad j = 1,2,3. \tag{3.36}$$

As one writes $\mathbf{k} = x_1\mathbf{b}_1 + x_2\mathbf{b}_2 + x_3\mathbf{b}_3$, Eq. (3.36) becomes

$$e^{i2\pi\cdot N_j x_j} = 1. \tag{3.37}$$

Consequently, one must have

$$x_j = \frac{m_j}{N_j}, \tag{3.38}$$

where m_j is integer valued. Therefore the general form for allowed Bloch wave vectors is

$$\mathbf{k} = \sum_{j=1}^{d} \frac{m_j}{N_j} \mathbf{b}_j, \tag{3.39}$$

where d is the dimensionality of the system and $m_j \in \mathbb{Z}$. For example, the allowed k-values for a triangular lattice having $N_1 = N_2 = 6$ are shown in Fig. 3.2. Moreover, it follows from Eq. (3.39) that in a two-dimensional case the area taken by a single k-value is $|(\mathbf{b}_1/N_1) \times (\mathbf{b}_2/N_2)|$. Similarly, in a three dimensional case the volume $V_\mathbf{k}$ occupied by a single value of k is the volume of a parallelepiped with edges $\mathbf{b}_j/N_j$. That is,

$$V_\mathbf{k} = \frac{\mathbf{b}_1}{N_1} \cdot \left(\frac{\mathbf{b}_2}{N_2} \times \frac{\mathbf{b}_3}{N_3} \right) = \frac{1}{N} \mathbf{b}_1 \cdot (\mathbf{b}_2 \times \mathbf{b}_3) \,. \tag{3.40}$$

Since $\mathbf{b}_1 \cdot (\mathbf{b}_2 \times \mathbf{b}_3)$ is the volume of a reciprocal lattice primitive cell, Eq. (3.40) implies that the number of wave vectors in a primitive cell of the reciprocal lattice is equal to the number of sites in the crystal.

According to the Bloch theorem, the crystal momentum k indicates how an energy eigenstate $\psi_{n\mathbf{k}}(\mathbf{r})$ changes under a translation by some Bravais lattice vector $\mathbf{R} = n_1\mathbf{a}_1 + n_2\mathbf{a}_2 + n_3\mathbf{a}_3$. In order to study what values of k are distinct, one assumes that $\mathbf{K} = n_1'\mathbf{b}_1 + n_2'\mathbf{b}_2 + n_3'\mathbf{b}_3$ is a reciprocal lattice vector. Employing Eq. (3.32), one obtains

$$\begin{aligned} \psi_{n\mathbf{k}+\mathbf{K}}(\mathbf{r}+\mathbf{R}) &= e^{i(\mathbf{k}+\mathbf{K})\cdot\mathbf{R}} \psi_{n\mathbf{k}+\mathbf{K}}(\mathbf{r}) \\ &= \underbrace{e^{i\mathbf{K}\cdot\mathbf{R}}}_{=1} e^{i\mathbf{k}\cdot\mathbf{R}} \psi_{n\mathbf{k}+\mathbf{K}}(\mathbf{r}). \end{aligned} \tag{3.41}$$

Thus, energy eigenstates characterized by crystal momentums k and $\mathbf{k}+\mathbf{K}$ behave in the same way under a translation by a Bravais lattice vector $\mathbf{R}$. Therefore crystal momentums that differ by a reciprocal lattice vector are considered the same. Consequently, it suffices to consider values of k belonging to the first Brillouin zone.

Values of k *for a triangular lattice*

Let us consider a triangular lattice spanned by the primitive vectors (3.30). The primitive vectors of the reciprocal lattice are then given by Eq. (3.31).

Subsequently, the allowed values of crystal momentum $\mathbf{k}$ are of the form Eq. (3.39) with $d = 2$. For example, with $N_1 = N_2 = 6$ the $N = N_1 N_2 = 36$ values of $\mathbf{k}$ belonging to the first Brillouin zone are depicted in Fig. 3.2.

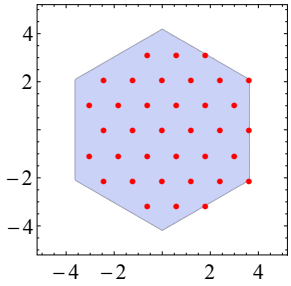

Figure 3.2. Allowed values of $\mathbf{k}$ for a triangular lattice of size $N_1 = N_2 = 6$.

Note that the values of $\mathbf{k}$ lying on the opposite edges of Brillouin zone are related to each other via a translation by $\mathbf{b}_1$, $\mathbf{b}_2$ or $\mathbf{b}_1 + \mathbf{b}_2$. Therefore one excludes $\mathbf{k}$-points with nonpositive x-component in order to avoid double counting. Since the double counting has now been avoided, the number of $\mathbf{k}$-points in Fig. 3.2 is equal to the number of sites in the direct lattice, namely $N = N_1 N_2 = 36$.

3.4.5 Honeycomb lattice

One recalls that the neighborhoods of all points must be the identical in order for a structure to qualify as a Bravais lattice. However, there are many lattices in nature that are not Bravais lattices, but are lattices with a basis. This type of lattices are constructed by starting with a Bravais lattice, and then replacing each lattice point with a set of points.

For example, a honeycomb lattice is a lattice with basis. The underlying lattice is a triangular lattice, and let us now say that the primitive vectors are

$$\begin{aligned} \mathbf{a}_1 &= a\begin{pmatrix}\sqrt{3}/2 & 1/2\end{pmatrix}, \\ \mathbf{a}_2 &= a\begin{pmatrix}\sqrt{3}/2 & -1/2\end{pmatrix}. \end{aligned} \tag{3.42}$$

Subsequently, a honeycomb lattice is constructed by replacing each point with the set of points

$$v_1 = a\begin{pmatrix}0 & 0\end{pmatrix}, \tag{3.43}$$

$$v_2 = a\begin{pmatrix}0 & 1/\sqrt{3}\end{pmatrix}. \tag{3.44}$$

However, in a certain sense a honeycomb lattice can be considered a Bravais lattice. That is, a honeycomb lattice can be viewed as a triangular lattice with the lattice points replaced by identical unit cells, which each contain two particles [90]. Consequently, triangular and honeycomb lattices have the same reciprocal lattice.

3.5 Topological phases

3.5.1 Hall conductivity and Chern numbers

Topological phases have attracted quite a lot scientific attention in the recent years [91, 92, 93, 94, 95]. In lower dimensions, i.e. one and two dimensions, topological quantum numbers are known to play a crucial role in characterizing various phase transitions. A typical example is the integer quantum Hall transition, where quantized Hall conductances are given by Chern numbers associated with the Berry connection [96, 97].

Quantization of Hall conductivity
In order to study the integer quantum Hall effect, we consider a two-dimensional lattice described by a momentum space Hamiltonian $H(\mathbf{k})$. When the Fermi energy lies in a gap, the Hall conductance is given by

$$\sigma_{xy} = -\frac{e^2}{h} \sum_n c_n, \tag{3.45}$$

where c_n denotes the Chern number of the nth Bloch band, and the sum over n is restricted to the bands below the Fermi energy. The Chern number assigned to the nth band is defined by

$$c_n = \frac{1}{2\pi i} \int_{\mathrm{BZ}} F_{xy}(\mathbf{k})\, dk_x dk_y, \tag{3.46}$$

where the field strength

$$F_{xy}(\mathbf{k}) = \frac{\partial A_y(\mathbf{k})}{\partial k_x} - \frac{\partial A_x(\mathbf{k})}{\partial k_y} \tag{3.47}$$

is defined in terms of the Berry connection

$$A_j(\mathbf{k}) = \langle n(\mathbf{k}) | \frac{\partial}{\partial k_j} | n(\mathbf{k}) \rangle, \quad j \in \{x, y\}. \tag{3.48}$$

Here $|n(\mathbf{k})\rangle$ is the nth Bloch band eigenfunction so that $H(\mathbf{k})|n(\mathbf{k})\rangle = E_n(\mathbf{k})|n(\mathbf{k})\rangle$. It is well-known that the Chern numbers c_n are integers, but let us still prove that next.

Let us define

$$\mathbf{A}(\mathbf{k}) = \begin{pmatrix} A_x(\mathbf{k}) & A_y(\mathbf{k}) & 0 \end{pmatrix}. \tag{3.49}$$

Subsequently, we can rewrite Eq. (3.46) as

$$c_n = \frac{1}{2\pi i} \int_{\mathrm{BZ}} \nabla \times \mathbf{A}(\mathbf{k}) \cdot d\mathbf{\Sigma}. \tag{3.50}$$

By employing the Stokes theorem, it can be shown that the Chern numbers c_n vanish if $\mathbf{A}(\mathbf{k})$ is globally well-defined over the Brillouin zone. That is, if the eigenfunctions $|n(\mathbf{k})\rangle$ can be chosen to have a smooth gauge over the whole Brillouin zone, the Chern numbers c_n vanish.

Let us now assume that the eigenfunctions $|n(\mathbf{k})\rangle$ cannot be chosen to have smooth gauge over the whole Brillouin zone. However, let us assume that the Brillouin zone can be divided into two separate regions R_1 and R_2 so that the eigenfunctions $|n(\mathbf{k})\rangle$ can be gauge smoothed within each of those patches. We denote the gauge smoothed eigenfunctions in regions R_1 and R_2 by

$$|\psi_{1n}(\mathbf{k})\rangle = e^{if(\mathbf{k})}|n(\mathbf{k})\rangle, \tag{3.51}$$

$$|\psi_{2n}(\mathbf{k})\rangle = e^{ig(\mathbf{k})}|n(\mathbf{k})\rangle, \tag{3.52}$$

respectively. At the boundary between the two regions, the two wave functions are related by

$$|\psi_{2n}(\mathbf{k})\rangle = e^{i(g(\mathbf{k})-f(\mathbf{k}))}|\psi_{1n}(\mathbf{k})\rangle = e^{i\chi(\mathbf{k})}|\psi_{1n}(\mathbf{k})\rangle. \tag{3.53}$$

Let us denote the function $\mathbf{A}(\mathbf{k})$ defined in regions R_1 and R_2 by $\mathbf{A}_1(\mathbf{k})$ and $\mathbf{A}_2(\mathbf{k})$, respectively. Subsequently, by using Eqs. (3.48), (3.49) and (3.53), we obtain

$$\mathbf{A}_2(\mathbf{k}) = \mathbf{A}_1(\mathbf{k}) + i\nabla\chi(\mathbf{k}) \tag{3.54}$$

at the boundary of regions R_1 and R_2. Let us then use Eq. (3.50) and the

fact that $R_1 + R_2 = \text{BZ}$. We obtain

$$\begin{aligned} c_n &= \frac{1}{2\pi i}\left(\int_{R_1} \nabla \times \mathbf{A}_1(\mathbf{k}) \cdot d\mathbf{\Sigma} + \int_{R_2} \nabla \times \mathbf{A}_2(\mathbf{k}) \cdot d\mathbf{\Sigma}\right) \\ &= \frac{1}{2\pi i}\left(\int_{\text{BZ}-R_2} \nabla \times \mathbf{A}_1(\mathbf{k}) \cdot d\mathbf{\Sigma} + \int_{R_2} \nabla \times \mathbf{A}_2(\mathbf{k}) \cdot d\mathbf{\Sigma}\right). \quad (3.55) \end{aligned}$$

The functions $\mathbf{A}_1(\mathbf{k})$ and $\mathbf{A}_2(\mathbf{k})$ are well-behaved in the patches R_1 and R_2, respectively. Therefore, by employing the Stokes' theorem, we obtain

$$c_n = \frac{1}{2\pi i}\left(\int_{\partial(\text{BZ}-R_2)} \mathbf{A}_1(\mathbf{k}) \cdot d\mathbf{k} + \int_{\partial R_2} \mathbf{A}_2(\mathbf{k}) \cdot d\mathbf{k}\right), \quad (3.56)$$

where ∂R_2 means the boundary of region R_2. Since it can be shown that

$$\int_{\partial(\text{BZ}-R_2)} \mathbf{A}_1(\mathbf{k}) \cdot d\mathbf{k} = -\int_{\partial R_2} \mathbf{A}_1(\mathbf{k}) \cdot d\mathbf{k}, \quad (3.57)$$

we obtain

$$c_n = \frac{1}{2\pi i}\int_{\partial R_2} (\mathbf{A}_2(\mathbf{k}) - \mathbf{A}_1(\mathbf{k})) \cdot d\mathbf{k}. \quad (3.58)$$

Using Eq. (3.54), we obtain

$$c_n = \frac{1}{2\pi}\int_{\partial R_2} \nabla\chi(\mathbf{k}) \cdot d\mathbf{k}. \quad (3.59)$$

Let us say that boundary ∂R_2 is parameterized by $\mathbf{K}(\theta)$ with $\theta \in [0, 2\pi)$. Subsequently, we obtain

$$\int_{\partial R_2} \nabla\chi(\mathbf{k}) \cdot d\mathbf{k} = \lim_{\theta\to 2\pi} \chi\left(\mathbf{K}(\theta)\right) - \chi\left(\mathbf{K}(0)\right). \quad (3.60)$$

The wave functions $|\psi_{1n}(\mathbf{k})\rangle$ and $|\psi_{2n}(\mathbf{k})\rangle$ must be single-valued. Thus $\lim_{\theta\to 2\pi} |\psi_{jn}\left(\mathbf{K}(\theta)\right)\rangle = |\psi_{jn}\left(\mathbf{K}(0)\right)\rangle$, where $j \in \{1, 2\}$. Consequently, Eq. (3.53) implies that $\lim_{\theta\to 2\pi} \chi\left(\mathbf{K}(\theta)\right) = \chi\left(\mathbf{K}(0)\right) + 2\pi m$, where $m \in \mathbb{Z}$. Substituting this into Eq. (3.60), we obtain

$$\int_{\partial R_2} \nabla\chi(\mathbf{k}) \cdot d\mathbf{k} = 2\pi m. \quad (3.61)$$

Substituting Eq. (3.61) into Eq. (3.59), we obtain $c_n = m \in \mathbb{Z}$. That is, the Chern numbers c_n indeed are integers and the Hall conductivity given by Eq. (3.45) is an integer multiple of $-e^2/h$.

Numerical method for calculating Chern numbers

In the numerical calculations of Publication IV, we used the method from Ref. [98] to calculate the Chern numbers. In order to summarize that method, we consider a two-dimensional lattice described by a momentum space Hamiltonian $H(\mathbf{k})$. We denote the reciprocal lattice vectors by $\mathbf{b}_1$ and $\mathbf{b}_2$, and the directional derivatives along $\mathbf{b}_1$ and $\mathbf{b}_2$ by ∂_1 and ∂_2, respectively. Furthermore, we denote the Brillouin zone k-points depicted in Fig. 3.2 by $\mathbf{k}_l$ and assume that $|n(\mathbf{k})\rangle$ is the nth Bloch band eigenstate so that $H(\mathbf{k})|n(\mathbf{k})\rangle = E_n(\mathbf{k})|n(\mathbf{k})\rangle$. One defines a link variable from the wave functions of the nth band as

$$U_\mu(\mathbf{k}) = \langle n(\mathbf{k}_l)|n(\mathbf{k}_l + \hat{\mathbf{b}}_\mu)\rangle / \mathcal{N}_\mu(\mathbf{k}_l), \tag{3.62}$$

where $\mathcal{N}_\mu(\mathbf{k}_l) = |\langle n(\mathbf{k}_l)|n(\mathbf{k}_l + \hat{\mathbf{b}}_\mu)\rangle|$ and $\hat{\mathbf{b}}_\mu$ is a vector that connects two adjacent k-points in the direction of $\mathbf{b}_\mu$. From the link variable (3.62) one defines a lattice field strength

$$\tilde{F}_{12}(\mathbf{k}_l) = \ln U_1(\mathbf{k}_l) U_2(\mathbf{k}_l + \hat{\mathbf{b}}_1) U_1(\mathbf{k}_l + \hat{\mathbf{b}}_2)^{-1} U_2(\mathbf{k}_l)^{-1} \tag{3.63}$$

with the additional restriction $-i\pi < \tilde{F}_{12}(\mathbf{k}_l) \leq i\pi$. That is, the field strength $\tilde{F}_{12}(\mathbf{k}_l)$ is defined in the principal branch of the logarithm. Moreover, it can be shown that $\tilde{F}_{12}(\mathbf{k}_l)$ does not depend on the gauge choice of Bloch eigenstates $|n(\mathbf{k}_l)\rangle$. Finally, one defines the lattice Chern number for the nth band as

$$\tilde{c}_n = \frac{1}{2\pi i} \sum_l \tilde{F}_{12}(\mathbf{k}_l). \tag{3.64}$$

It can be shown that $\tilde{c}_n \to c_n$ when the number of k-points increases. Since both $\tilde{c}_n$ and c_n are integers, this means that $\tilde{c}_n = c_n$ for a sufficiently dense k-point grid.

3.5.2 Time-Reversal Symmetry

The most important discrete symmetry for experimentally realizable systems is time-reversal [99]. Time reversal is a transformation T that reverses the arrow of time. That is,

$$T : t \to -t. \tag{3.65}$$

Since time-reversal symmetry is a fundamental property, systems behave quite differently depending on whether they are symmetric under time reversal or not. For example, systems that posses time-reversal symmetry cannot exhibit the Hall effects (excluding the spin Hall effect). Mathematically, one says that a system is symmetric under time reversal if the Hamiltonian H commutes with T. That is, if

$$[H, T] = 0. \tag{3.66}$$

The time reversal operator changes only the arrow of time. As such, it leaves the position operator $\hat{x}$ unchanged. However, time-reversal operator flips the sign of the momentum operator $\hat{p}$ because it is proportional to the velocity, which is a time-derivative of a time-reversal invariant quantity (the position operator). Thus

$$T\hat{x}T^{-1} = \hat{x} \quad \text{and} \quad T\hat{p}T^{-1} = -\hat{p}. \tag{3.67}$$

Similarly, time-reversal flips the sign of spin operator $\mathbf{S}$, because angular momentum is itself a momentum. Thus

$$T\mathbf{S}T^{-1} = -\mathbf{S}. \tag{3.68}$$

Subsequently, T leaves the on-site creation operators unchanged for spinless particles. That is,

$$T\hat{c}_j T^{-1} = \hat{c}_j, \tag{3.69}$$

where one can add any orbital indices to c_j as long as the index is not spin. On the other hand, for spin-1/2 particles one has

$$T\hat{c}_{j\uparrow}T^{-1} = \hat{c}_{j\downarrow} \quad \text{and} \quad T\hat{c}_{j\downarrow}T^{-1} = -\hat{c}_{j\uparrow}. \tag{3.70}$$

3.5.3 Ways to break time-reversal symmetry

A well-known way to break time-reversal symmetry is to introduce an external magnetic field. However, since the publication of the Haldane model [100], there has been great interest in lattice models where time-reversal symmetry is broken without the help of an external magnetic field. In the original Haldane model the time-reversal symmetry is broken by complex tunneling amplitudes, whereas in Publication IV an attractive

nearest-neighbor interaction gives rise to spontaneous time-reversal symmetry breaking. It was long-believed that the Haldane model would be a mere theoretical tool, but recently it has been realized experimentally by using an ultracold atomic gas in an optical lattice. In the experiment, the complex valued tunneling amplitude arises from the fact that the tunneling is laser assisted [101, 102].

Interparticle interactions may also give rise to time-reversal symmetry breaking. For example, chiral superconductors feature pairing gaps that wind in phase around the Fermi surface in multiples of 2π, thus breaking time-reversal symmetry. Chiral superconductivity, as exotic superconductivity in general, is an active research topic, and it has properties that are very useful in nanoscience applications [103].

3.6 Note on Figure 3 of Ref. [1]

Figure 3 of Ref. [1] is not quantitatively correct. Correct version is given in Fig. 3.3. However, Fig. 3.3 and Fig. 3 of Ref. [1] show the same qualitative behavior for the gapless phase. That is, the gapless phase becomes less robust when $\tilde{\epsilon}$ increases. On the other hand, by comparing Fig. 3.3 with Fig. 2a of Ref. [1] we see that the gapped phase is not insensitive to $\tilde{\epsilon}$ but becomes more robust when $\tilde{\epsilon}$ is increased.

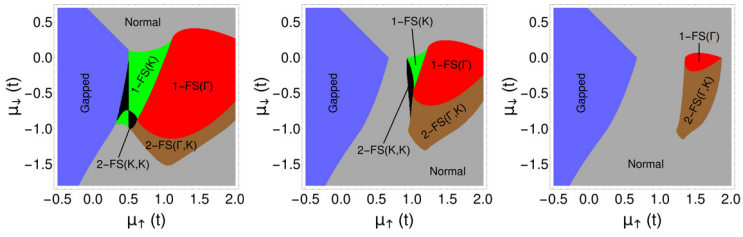

(a) Parameter $\tilde{\epsilon} = 1.0$. (b) Parameter $\tilde{\epsilon} = 1.4$. (c) Parameter $\tilde{\epsilon} = 1.8$.

Figure 3.3. Correct versions of phase diagrams presented in Fig. 3 of Ref. [1].

3.7 Summary of Publication IV

In Publication IV we consider spin-1/2 fermions loaded in a honeycomb-triangular lattice. The up-spin component is free to move in the whole honeycomb lattice, but the down-spin component is confined to the underlying triangular lattice A (see Fig. 3.4). We assume that there is an attractive on-site and nearest-neighbor interaction between particles of opposite

spin, and we study the resulting phase diagram of the system. In particular, we study whether an FFLO phase appears in the diagram. Furthermore, we investigate whether the long-range interaction gives rise to spontaneous time-reversal symmetry breaking and topological phases.

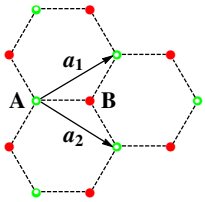

Figure 3.4. Honeycomb-triangular lattice. Up-spin component is free to move in the whole honeycomb lattice comprising sublattices A and B, but the down-spin component is confined to the triangular sublattice A. Vectors $\mathbf{a}_1$ and $\mathbf{a}_2$ are the primitive vectors of sublattice A.

3.7.1 Deriving the grand potential

In Publication IV and its Supplemental Material the full mean-field Hamiltonian

$$\mathcal{H}_{\text{MF}} = \sum_{\mathbf{k}} \tilde{\Psi}_{\mathbf{k}}^{\dagger} H_{\mathbf{k}} \tilde{\Psi}_{\mathbf{k}} + \frac{3|\Delta_1|^2}{V} + \frac{\Delta_0^2}{U} + \xi_{-\mathbf{k}}^{(3)}, \tag{3.71}$$

where $H_{\mathbf{k}}$ is a 3×3-matrix, $\tilde{\Psi}_{\mathbf{k}}$ is the basis, Δ_1 is the amplitude of the nearest-neighbor order parameter, V is the strength of the nearest-neighbor interaction, Δ_0 is the amplitude of the on-site order parameter, U is the strength of the on-site interaction, and $\xi_{-\mathbf{k}}^{(3)}$ is the dispersion relation of the down-spin band in a non-interacting system. Let us say that $\bar{U}$ is a matrix that diagonalizes $H_{\mathbf{k}}$. That is, let us say that $\bar{U}$ is such a matrix that $D = \bar{U}^{\dagger} H_{\mathbf{k}} \bar{U}$ is diagonal. It is well-known that the diagonal elements of D are the eigenvalues of $H_{\mathbf{k}}$ which we denote by $E_1(\mathbf{k})$, $E_2(\mathbf{k})$ and $E_3(\mathbf{k})$. Subsequently, Bogoliubov transformation yields

$$\mathcal{H}_{\text{MF}} = \sum_{\mathbf{k}} \frac{3|\Delta_1|^2}{V} + \frac{\Delta_0^2}{U} + \xi_{-\mathbf{k}}^{(3)} + \sum_{\mathbf{k}} \sum_{\alpha=1}^{3} E_{\alpha}(\mathbf{k}) \hat{\gamma}_{\alpha\mathbf{k}}^{\dagger} \hat{\gamma}_{\alpha\mathbf{k}} \tag{3.72}$$

with the quasiparticle basis $\begin{pmatrix} \hat{\gamma}_{1\mathbf{k}} & \hat{\gamma}_{2\mathbf{k}} & \hat{\gamma}_{3\mathbf{k}} \end{pmatrix} = \bar{U}^{\dagger} \tilde{\Psi}_{\mathbf{k}}$.

The grand canonical partition function [104]

$$Z = \operatorname{Tr} e^{-\beta \mathcal{H}_{\text{MF}}}. \tag{3.73}$$

By using fermionic anticommutation relations, it is easy to show that the quasiparticle number operators $\hat{n}_{\alpha\mathbf{k}} = \hat{\gamma}^{\dagger}_{\alpha\mathbf{k}}\hat{\gamma}_{\alpha\mathbf{k}}$ commute with each other. Therefore their common eigenstates $|\gamma\rangle$ form a complete basis. Let us denote the number of type $\alpha \in \{1,2,3\}$ quasiparticles with wave vector $\mathbf{k}$ in state γ by $n_\alpha(\mathbf{k},\gamma)$. Subsequently, we obtain

$$Z = e^{-\beta C}\sum_{\gamma}\prod_{\mathbf{k}}\prod_{\alpha} e^{-\beta E_\alpha(\mathbf{k})n_\alpha(\mathbf{k},\gamma)}, \tag{3.74}$$

where

$$C = \sum_{\mathbf{k}} \frac{3|\Delta_1|^2}{V} + \frac{\Delta_0^2}{U} + \xi^{(3)}_{-\mathbf{k}}. \tag{3.75}$$

Since the quasiparticles are fermions, the occupation number of each single particle state is either 0 or 1. That is, $\hat{n}_{\alpha\mathbf{k}}|\gamma\rangle = n_\alpha(\mathbf{k},\gamma)|\gamma\rangle$, where $n_\alpha(\mathbf{k},\gamma) \in \{0,1\}$. Consequently, we obtain

$$Z = e^{-\beta C}\prod_{\mathbf{k}}\prod_{\alpha}(1 + e^{-\beta E_\alpha(\mathbf{k})}). \tag{3.76}$$

As shown in Ref. [105], the grand potential

$$\begin{aligned}\Omega &= -\frac{1}{\beta}\ln Z \\ &= C - \frac{1}{\beta}\sum_{\mathbf{k}}\sum_{\alpha}\ln\left(1 + e^{-\beta E_\alpha(\mathbf{k})}\right)\end{aligned} \tag{3.77}$$

with C being defined in Eq. (3.75).

Grand potential Ω at zero temperature

In order to derive Ω at zero temperature, we note that $\beta = 1/(k_{\mathrm{B}}T) \to \infty$ when $T \to 0$. Thus

$$-\frac{1}{\beta}\ln\left(1 + e^{-\beta E_\alpha(\mathbf{k})}\right) \to \begin{cases} 0 & \text{if } E_\alpha(\mathbf{k}) \geq 0 \\ E_\alpha(\mathbf{k}) & \text{if } E_\alpha(\mathbf{k}) < 0. \end{cases} \tag{3.78}$$

Thus, the last term in Eq. (3.77) reduces to sum over negative eigenvalues when $T = 0$. In equation form,

$$\Omega = C + \frac{1}{2}\sum_{\mathbf{k}}\big(E_\alpha(\mathbf{k}) - |E_\alpha(\mathbf{k})|\big). \tag{3.79}$$

when $T = 0$.

3.7.2 Main results of Publication IV

Nowadays long-range interactions between particles, FFLO phase and various other symmetry breaking superfluid phases are attracting significant attention in the cold atom community. Publication IV studies those topics in the context of a spin-dependent honeycomb-triangular lattice, where up-spin particles are free to move in the honeycomb lattice, but down-spin particles are confined to the triangular lattice. Such a geometry has already been proposed in Ref. [1], but we also took into account a nearest-neighbor attraction and formulated it in such a way that spontaneous time-reversal symmetry breaking became possible. Furthermore, we examined whether the system can be found in FFLO phase.

Figure 3.5 shows the phase diagram for $U = 5$ and $V = 3$, and we immediately see that a relatively large area is covered by the FFLO phase. Therefore unconventional superfluidity with spatial symmetry breaking is a significant phenomenon in a honeycomb-triangular lattice.

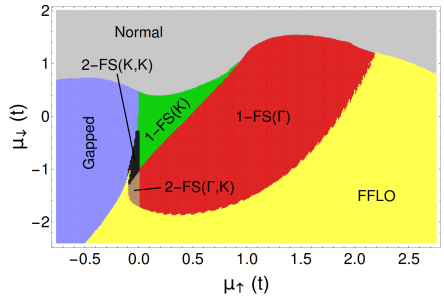

Figure 3.5. (Reprinted with permission from Publication IV.) Zero temperature phase diagram as a function of chemical potentials $\mu_\uparrow$ and $\mu_\downarrow$. The on-site interaction strength $U = 5$ and the NN interaction strength $V = 3$. Gray means normal phase, yellow means FFLO phase, blue means fully paired gapped phase, and the other areas belong to the gapless phase characterized by one or two Fermi surfaces centered at the Brillouin zone points Γ or K [1].

We measured the significance of intersite Cooper pairing with the relative weight of the nearest-neighbor bond, namely $P = |\Delta_1|/(|\Delta_0| + |\Delta_1|)$. We found out that the intersite pairing is a significant phenomenon in the honeycomb-triangular lattice with P being mostly around 0.2 in Fig. 3.5.

The nearest-neighbor interaction term has been formulated in such a way that it accounts for the possibility of spontaneous time-reversal symmetry (TRS) breaking. Loosely speaking, the system breaks TRS if the NN pairing order parameter phase angles θ, ϕ and φ become nonzero (for further details, see Publication IV). Figure 3.6 shows the phase angles θ, ϕ and φ as a function of U and V for $\mu_\uparrow = -1.5$ and $\mu_\downarrow = -2.5$. Indeed, at large V the phase angles become nonzero and thereby the system breaks

TRS.

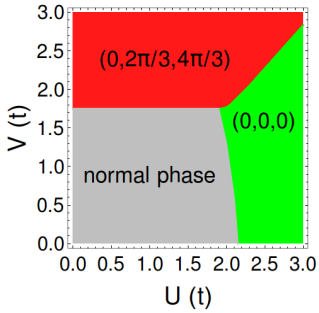

Figure 3.6. (Reprinted with permission from Publication IV.) The phase angles $(\theta \quad \phi \quad \varphi)$ of the NN pairing order parameter as a function of U and V for $(\mu_\uparrow \quad \mu_\downarrow) = (-1.5 \quad -2.5)$.

As pointed out in Publication IV, there are also instances where TRS is broken in the FFLO phase. That is, we managed to find an exotic superfluid phase where spatial and time-reversal symmetries are simultaneously broken.

The breaking of TRS gives rise to topologically nontrivial phases characterized by energy bands having nonzero Chern numbers c_n. On the other hand, when the Fermi energy lies in a gap, the Hall conductivity is given by

$$\sigma_{xy} = -\frac{e^2}{h} \sum_n c_n, \tag{3.80}$$

where the sum is restricted to bands below the Fermi energy [98]. Thus, the TRS breaking also gives rise to nonzero Hall conductivities in the system.

4. Summary

In this thesis, the first topic studied was ultracold Bose gases with the focus on developing a phenomenological model that would explain the excitation spectrum observed in the Bragg scattering experiment of Ref. [63]. In that experiment, Papp et al. measured the excitation spectrum of a ^{85}Rb Bose-Einstein condensate, and by employing Feshbach resonance they were able to push into a regime where existing theoretical models were no more valid. Thus, the experiment was particularly interesting to analyze. In Publication I we first showed that traditionally used effective potentials, such as hardcore potential or contact potential, fail to predict the observed excitation spectrum. We proceeded by constructing spin-independent ad-hoc potentials that could be used within variational many-body theory to calculate the excitation spectrum, and we managed to find a good fit to the experimental results. However, the potentials we had developed did not support any bound states, and therefore there was no way to calculate the energy of the molecular Feshbach resonance state. Since the energy of the molecular Feshbach resonance state can be measured and predicted accurately by full coupled-channels calculations, we needed to improve our model so that it would take into account the presence of the molecular bound state.

In Publications II and III we improved our model by describing the Feshbach resonant system with T-matrix formalism. The T-matrix formalism uses separable potentials to represent the interactions between particles, and we incorporated the scaling property we had introduced in Publication I into these separable potentials. Subsequently, we calculated the scattering phase shift from the T-matrix, and used Marchenko inversion to construct the corresponding local potential. Then we calculated the excitation spectrum by using variational many-body theory and these potentials and managed to obtain a good fit to the experimental results.

Furthermore, we could now calculate the molecular Feshbach resonance state energy, because bound states correspond to poles of the T-matrix. We successfully fitted some binding energies known from experiments or full coupled-channel calculations, but later I discovered that some other binding energies predicted by our model are clearly unphysical (see Section 2.5). The unphysical molecular Feshbach resonance state energies manifest at large scattering lengths, which is the regime where we claimed our phenomenological model to be valid.

As a second topic, I studied ultracold fermions confined to an optical lattice. To be more precise, I studied a novel mixed-geometry setup, where one spin-component is loaded in a honeycomb lattice whereas the other is confined the underlying triangular lattice. Although such a setup might sound complicated at first, similar spin-dependent lattices have already been realized (see, for instance, Ref. [31]). We considered an attractive nearest-neighbor interaction in addition to an on-site interaction, and formulated the NN interaction in such a way that it takes into account the possibility of spontaneous time-reversal symmetry breaking. A particularly feasible way of realizing this model would be to employ the commonly used rubidium-potassium mixture, which is composed of fermionic ^{40}K prepared in the $|F = 9/2, m_F = -7/2\rangle$ and $|F = 9/2, m_F = -9/2\rangle$ Zeeman components of the $F = 9/2$ ground-state hyperfine level and bosonic ^{87}Rb atoms in the $|F = 1, m_F = 1\rangle$ ground state. The on-site and NN interactions could be tuned independently, and various experimental methods should be available to study the nature of the pairing [44, 106].

Firstly, we found a multitude of breached pair type states with different Fermi surface configurations. Secondly, we discovered that Cooper pairing between particles of nonopposite momenta is a significant phenomenon in the mixed-geometry system. In other words, a relatively large area of the system's phase diagram is covered by the FFLO phase. Thus, the system exhibits exotic superfluidity with spatial symmetry breaking. As we have already pointed out in previous sections, realizing the FFLO state has been a major goal since the creation of first Fermi condensates, but definitive evidence is still missing. Nevertheless, several proposals have been made on how one could experimentally detect the FFLO phase [82, 83, 84, 85, 81, 86]. Thus, Publication IV might motivate experimental attempts to realize the FFLO state. If successful, the results would be very interesting on their own, and they could also shed light on a number of open topics, e.g. high temperature superconductivity.

We also discovered that the system spontaneously breaks TRS when the intersite attraction V is large enough. Furthermore, in some instances TRS was broken in the FFLO phase, which means that we managed to find an exotic superfluid phase where spatial and time-reversal symmetries are simultaneously broken. Moreover, the TRS breaking gives rise to topologically nontrivial phases characterized by nonzero Chern numbers and Hall conductivities. Usually, the Chern number c_n for the nth Bloch band is defined as an integral of a gauge independent field strength $F_{12}(\mathbf{k})$ over the Brillouin zone. That is,

$$c_n = \frac{1}{2\pi i} \int_{\mathrm{BZ}} F_{12}(\mathbf{k})\, d\mathbf{k}. \tag{4.1}$$

However, we used the method from Ref. [98] to calculate the Chern numbers. In that method, the Brillouin zone is first covered with a sufficiently dense mesh of discrete points $\mathbf{k}_l$. Subsequently, the Chern number is obtained as a sum

$$c_n = \frac{1}{2\pi i} \sum_l \tilde{F}_{12}(\mathbf{k}_l), \tag{4.2}$$

where the gauge independent field $\tilde{F}_{12}(\mathbf{k})$ is calculated from the nth band Bloch eigenstates. Remarkably, there is also a simple and robust way to measure the field strengths $\tilde{F}_{12}(\mathbf{k}_l)$ by using time-of-flight imaging [107]. Consequently, the topological states predicted in Publication IV could readily be detected with existing experimental methods.

To conclude, in Publication IV we studied a honeycomb-triangular lattice, and found FFLO state and phases with spontaneous time-reversal symmetry breaking. We discussed ways to experimentally realize the lattice setup, and ways to detect the FFLO state and topological states resulting from time-reversal symmetry breaking. If the predictions of this model were experimentally verified, the results would be extremely interesting. Furthermore, properties of chiral superconductors are generally considered useful in nanoscience applications, and therefore the results might also be useful in applied nanoscience [103, 108, 109, 110, 111]. Considering all these possibilities offered by mixed-geometry optical lattices, search for new interesting geometries should be highly lucrative.

Appendices

A. Honeycomb-triangular lattice

In this Appendix, I present analytical calculations related to the honeycomb-triangular lattice of Publication IV.

A.1 Preliminary results

A.1.1 About notation

By writing "S" in front of an equation number, we refer to Ref. [71]. For example, by (S5) we mean Eq. (5) of Ref. [71]. By writing "L" in front of an equation number, we refer to Ref. [105]. For example, by (L16) we mean Eq. (16) of Ref. [105].

A.1.2 Fourier transformation

We define the Fourier transformation as

$$\tilde{f}_{\mathbf{k}\sigma} = \frac{1}{\sqrt{M}} \sum_{m} e^{-i\mathbf{k}\cdot\mathbf{x}_m} \hat{f}_{m\sigma}, \tag{1.1}$$

where $f \in \{a, b\}$ and spin index $\sigma \in \{\downarrow, \uparrow\}$. Furthermore, x_m is the position vector of lattice site m, and M is the total number of sites in either sublattice A or B.

Subsequently, inverse Fourier transformation reads

$$\hat{f}_{n\sigma} = \frac{1}{\sqrt{M}} \sum_{\mathbf{k}} e^{i\mathbf{k}\cdot\mathbf{x}_n} \tilde{f}_{\mathbf{k}\sigma}. \tag{1.2}$$

We can verify that the inverse Fourier transformation has been correctly defined by substituting Eq. (1.1) into Eq. (1.2). Making the substitution,

we obtain

$$\frac{1}{M}\sum_{m}\underbrace{\sum_{\mathbf{k}} e^{i\mathbf{k}\cdot(\mathbf{x}_n-\mathbf{x}_m)}}_{=M\delta_{mn}}\hat{f}_{m\sigma}=\hat{f}_{n\sigma}. \tag{1.3}$$

Thus we have verified the definition of inverse Fourier transformation given in Eq. (1.2).

A.2 Noninteracting Hamiltonian in momentum space

The noninteracting Hamiltonian

$$\begin{aligned}\mathcal{H}_0 &= -t_\uparrow\sum_{\langle i,j\rangle\in\mathcal{L}_\uparrow}(\hat{a}^\dagger_{i\uparrow}\hat{b}_{j\uparrow}+\text{h.c.})-\mu_\uparrow\sum_i(\hat{n}^a_{i\uparrow}+\hat{n}^b_{i\uparrow})\\ &\quad -t_\downarrow\sum_{\langle i,j\rangle\in\mathcal{L}_\downarrow}(\hat{a}^\dagger_{i\downarrow}\hat{a}_{j\downarrow}+\text{h.c.})-(\mu_\downarrow-\epsilon^a_\downarrow)\sum_i\hat{n}^a_{i\downarrow}.\end{aligned} \tag{1.4}$$

Here $\hat{a}^\dagger_{i\sigma}$ and $\hat{a}_{i\sigma}$ are fermionic creation and annihilation operators for spin-σ particle at site i belonging to sublattice A. Similarly, $\hat{b}^\dagger_{j\sigma}$ and $\hat{b}_{j\sigma}$ are fermionic creation and annihilation operators for spin-σ particle at site j belonging to sublattice B.

Fourier transformation of number operator terms
We easily obtain

$$\sum_i n^a_{i\sigma} = \sum_i a^\dagger_{i\sigma}a_{i\sigma}=\sum_{\mathbf{k}}\tilde{a}^\dagger_{\mathbf{k}\sigma}\tilde{a}_{\mathbf{k}\sigma}, \tag{1.5}$$

$$\sum_i n^b_{i\uparrow} = \sum_i b^\dagger_{i\uparrow}b_{i\uparrow}=\sum_{\mathbf{k}}\tilde{b}^\dagger_{\mathbf{k}\uparrow}\tilde{b}_{\mathbf{k}\uparrow}. \tag{1.6}$$

Identifying tight-binding Hamiltonian $\hat{H}_{0\uparrow}$
The tight-binding Hamiltonian for the $\uparrow$-component reads

$$\hat{H}_{0\uparrow}=-t_\uparrow\sum_{\langle i,j\rangle\in\mathcal{L}_\uparrow}a^\dagger_{i\uparrow}b_{j\uparrow}+\text{h.c.} \tag{1.7}$$

By using Eqs. (L16), (L22) and (L23), we obtain

$$\hat{H}_{0\uparrow}=\sum_{\mathbf{k}}\tilde{\Phi}^\dagger_{\mathbf{k}}\begin{pmatrix}0 & t_\uparrow h_\uparrow(\mathbf{k}) & 0\\ t_\uparrow h^*_\uparrow(\mathbf{k}) & 0 & 0\\ 0 & 0 & 0\end{pmatrix}\tilde{\Phi}_{\mathbf{k}}, \tag{1.8}$$

where $\tilde{\Phi}^\dagger_{\mathbf{k}} = \begin{pmatrix} \tilde{a}^\dagger_{\mathbf{k}\uparrow} & \tilde{b}^\dagger_{\mathbf{k}\uparrow} & \tilde{a}^\dagger_{\mathbf{k}\downarrow} \end{pmatrix}$ and

$$h_\uparrow(\mathbf{k}) = -t_\uparrow \left[\exp\left(\frac{ik_x}{\sqrt{3}}\right) + 2\exp\left(\frac{-ik_x}{2\sqrt{3}}\right)\cos\left(\frac{k_y}{2}\right)\right]. \tag{1.9}$$

Identifying the tight-binding Hamiltonian $\hat{H}_{0\downarrow}$

The tight-binding Hamiltonian for the $\downarrow$-component reads

$$\hat{H}_{0\downarrow} = -t_\downarrow \sum_{\langle i,j\rangle \in \mathcal{L}_\downarrow} a^\dagger_{i\downarrow} a_{j\downarrow} + \text{h.c.} \tag{1.10}$$

By using Eqs. (L34) and (L36), we obtain

$$\hat{H}_{0\downarrow} = \sum_{\mathbf{k}} \tilde{\Phi}^\dagger_{\mathbf{k}} \begin{pmatrix} 0 & 0 & 0 \\ 0 & 0 & 0 \\ 0 & 0 & E_\downarrow(\mathbf{k}) \end{pmatrix} \tilde{\Phi}_{\mathbf{k}} \tag{1.11}$$

with

$$E_\downarrow(\mathbf{k}) = -2t_\downarrow \left[\cos k_y + \cos\left(\frac{\sqrt{3}k_x + k_y}{2}\right) + \cos\left(\frac{k_y - \sqrt{3}k_x}{2}\right)\right]. \tag{1.12}$$

Noninteracting part $\mathcal{H}_0$ *in the basis* $\tilde{\Phi}^\dagger_{\mathbf{k}}$

By using Eqs. (1.5), (1.6), (1.7) and (1.10), we obtain

$$\begin{aligned} \mathcal{H}_0 \;=\; & \hat{H}_{0\uparrow} + \hat{H}_{0\downarrow} - \mu_\uparrow \sum_{\mathbf{k}} \left(\tilde{a}^\dagger_{\mathbf{k}\uparrow}\tilde{a}_{\mathbf{k}\uparrow} + \tilde{b}^\dagger_{\mathbf{k}\uparrow}\tilde{b}_{\mathbf{k}\uparrow} \right) \\ & - (\mu_\downarrow - \epsilon^a_\downarrow) \sum_{\mathbf{k}} \sum_{\mathbf{k}} \tilde{a}^\dagger_{\mathbf{k}\downarrow}\tilde{a}_{\mathbf{k}\downarrow}. \end{aligned} \tag{1.13}$$

Following the example of Ref. [1], we set $\epsilon^a_\downarrow = -3$. Subsequently, it is easy to see that

$$\mathcal{H}_0 = \sum_{\mathbf{k}} \tilde{\Phi}^\dagger_{\mathbf{k}} \mathbf{H}^{(0)}_{\mathbf{k}} \tilde{\Phi}_{\mathbf{k}} \tag{1.14}$$

with

$$\mathbf{H}^{(0)}_{\mathbf{k}} = \begin{pmatrix} -\mu_\uparrow & h_\uparrow(\mathbf{k}) & 0 \\ h^*_\uparrow(\mathbf{k}) & -\mu_\uparrow & 0 \\ 0 & 0 & \xi_\downarrow(\mathbf{k}) \end{pmatrix}, \tag{1.15}$$

where

$$\xi_{\downarrow}(\mathbf{k}) = -t_{\downarrow}\left[2\left(\cos k_y + \cos\left(\frac{\sqrt{3}k_x + k_y}{2}\right) + \cos\left(\frac{k_y - \sqrt{3}k_x}{2}\right)\right) + 3\right] - \mu_{\downarrow}. \quad (1.16)$$

In conclusion, we note that we would obtain $\mathbf{H}_{\mathbf{k}}^{(0)}$ from Eq. (5) of Ref. [71] by setting $\tilde{\epsilon} = 0$.

Diagonalizing the matrix $\mathbf{H}_{\mathbf{k}}^{(0)}$

Let us say that $\bar{U}$ is a unitary matrix that diagonalizes $\mathbf{H}_{\mathbf{k}}^{(0)}$. That is,

$$\bar{U}^{\dagger}\mathbf{H}_{\mathbf{k}}^{(0)}\bar{U} = \begin{pmatrix} \lambda_{\mathbf{k}}^{(1)} & 0 & 0 \\ 0 & \lambda_{\mathbf{k}}^{(2)} & 0 \\ 0 & 0 & \lambda_{\mathbf{k}}^{(3)} \end{pmatrix}. \quad (1.17)$$

I have solved the eigenvectors and eigenvalues of $\mathbf{H}_{\mathbf{k}}^{(0)}$ by using Mathematica. The eigenvalues are

$$\lambda_{\mathbf{k}}^{(1)} = |h_{\uparrow}(\mathbf{k})| - \mu_{\uparrow}, \quad (1.18)$$

$$\lambda_{\mathbf{k}}^{(2)} = -|h_{\uparrow}(\mathbf{k})| - \mu_{\uparrow}, \quad (1.19)$$

$$\lambda_{\mathbf{k}}^{(3)} = \xi_{\downarrow}(\mathbf{k}). \quad (1.20)$$

The corresponding eigenvectors are

$$X_1 = \frac{1}{\sqrt{2}}\begin{pmatrix} 1 & \exp(-i\phi_{\mathbf{k}}) & 0 \end{pmatrix}^{\mathbf{T}}, \quad (1.21)$$

$$X_2 = \frac{1}{\sqrt{2}}\begin{pmatrix} 1 & -\exp(-i\phi_{\mathbf{k}}) & 0 \end{pmatrix}^{\mathbf{T}}, \quad (1.22)$$

$$X_3 = \begin{pmatrix} 0 & 0 & 1 \end{pmatrix}^{\mathbf{T}} \quad (1.23)$$

with $\exp(-i\phi_{\mathbf{k}}) = h_{\uparrow}^{*}(\mathbf{k})/|h_{\uparrow}(\mathbf{k})|$. Thus

$$\bar{U} = \begin{pmatrix} 1/\sqrt{2} & 1/\sqrt{2} & 0 \\ \exp(-i\phi_{\mathbf{k}})/\sqrt{2} & -\exp(-i\phi_{\mathbf{k}})/\sqrt{2} & 0 \\ 0 & 0 & 1 \end{pmatrix}. \quad (1.24)$$

The Bogoliubov transformation $\mathcal{H}^0 = \sum_{\mathbf{k}} \tilde{\Phi}_{\mathbf{k}}^{\dagger}\bar{U}\bar{U}^{\dagger}\mathbf{H}_{\mathbf{k}}^{(0)}\bar{U}\bar{U}^{\dagger}\tilde{\Phi}_{\mathbf{k}}$ leads to a new basis $\begin{pmatrix} \hat{c}_{\mathbf{k}}^{(1)} & \hat{c}_{\mathbf{k}}^{(2)} & \hat{c}_{\mathbf{k}}^{(3)} \end{pmatrix}^{\mathbf{T}} = \bar{U}^{\dagger}\tilde{\Phi}_{\mathbf{k}}$. In this new basis,

$$\mathcal{H}^0 = \sum_{\mathbf{k}} \lambda_{\mathbf{k}}^{(1)}\hat{c}_{\mathbf{k}}^{(1)\dagger}\hat{c}_{\mathbf{k}}^{(1)} + \lambda_{\mathbf{k}}^{(2)}\hat{c}_{\mathbf{k}}^{(2)\dagger}\hat{c}_{\mathbf{k}}^{(2)} + \lambda_{\mathbf{k}}^{(3)}\hat{c}_{\mathbf{k}}^{(3)\dagger}\hat{c}_{\mathbf{k}}^{(3)}. \quad (1.25)$$

If $\mathbf{k}_0$ belongs to the k-point grid, then $-\mathbf{k}_0$ belongs to the k-point grid.

Therefore we can write

$$\begin{aligned}\sum_{\mathbf{k}} \lambda_{\mathbf{k}}^{(3)} \hat{c}_{\mathbf{k}}^{(3)\dagger} \hat{c}_{\mathbf{k}}^{(3)} &= \sum_{\mathbf{k}} \lambda_{-\mathbf{k}}^{(3)} \hat{c}_{-\mathbf{k}}^{(3)\dagger} \hat{c}_{-\mathbf{k}}^{(3)} \\ &= \sum_{\mathbf{k}} \lambda_{-\mathbf{k}}^{(3)} - \sum_{\mathbf{k}} \lambda_{-\mathbf{k}}^{(3)} \hat{c}_{-\mathbf{k}}^{(3)} \hat{c}_{-\mathbf{k}}^{(3)\dagger}, \end{aligned} \tag{1.26}$$

where we have also used the anticommutation relation $\{\hat{c}_{\mathbf{k}}^{(3)}, \hat{c}_{\mathbf{k}}^{(3)\dagger}\} = 1$. Substituting Eq. (1.26) into Eq. (1.25), we obtain

$$\mathcal{H}^0 = \sum_{\mathbf{k}} \lambda_{\mathbf{k}}^{(1)} \hat{c}_{\mathbf{k}}^{(1)\dagger} \hat{c}_{\mathbf{k}}^{(1)} + \lambda_{\mathbf{k}}^{(2)} \hat{c}_{\mathbf{k}}^{(2)\dagger} \hat{c}_{\mathbf{k}}^{(2)} - \lambda_{-\mathbf{k}}^{(3)} \hat{c}_{-\mathbf{k}}^{(3)} \hat{c}_{-\mathbf{k}}^{(3)\dagger} + \lambda_{-\mathbf{k}}^{(3)}. \tag{1.27}$$

The summation in Eq. (1.27) goes over the Brillouin zone k-points. Since we say that $\mathbf{q}$ is one of the Brillouin zone k-points, we can make the change $\mathbf{k} \to \mathbf{k} - 2\mathbf{q}$ in the second last term of the summand. Making these changes, we obtain

$$\mathcal{H}^0 = \sum_{\mathbf{k}} \lambda_{\mathbf{k}}^{(1)} \hat{c}_{\mathbf{k}}^{(1)\dagger} \hat{c}_{\mathbf{k}}^{(1)} + \lambda_{\mathbf{k}}^{(2)} \hat{c}_{\mathbf{k}}^{(2)\dagger} \hat{c}_{\mathbf{k}}^{(2)} - \lambda_{2\mathbf{q}-\mathbf{k}}^{(3)} \hat{c}_{2\mathbf{q}-\mathbf{k}}^{(3)} \hat{c}_{2\mathbf{q}-\mathbf{k}}^{(3)\dagger} + \lambda_{-\mathbf{k}}^{(3)}. \tag{1.28}$$

Hence, in the basis $\tilde{\Psi}_{\mathbf{k}} = \begin{pmatrix} \hat{c}_{\mathbf{k}}^{(1)} & \hat{c}_{\mathbf{k}}^{(2)} & \hat{c}_{2\mathbf{q}-\mathbf{k}}^{(3)\dagger} \end{pmatrix}^{\mathrm{T}}$

$$\mathcal{H}_0 = \sum_{\mathbf{k}} \tilde{\Psi}_{\mathbf{k}}^{\dagger} \begin{pmatrix} \lambda_{\mathbf{k}}^{(1)} & 0 & 0 \\ 0 & \lambda_{\mathbf{k}}^{(2)} & 0 \\ 0 & 0 & -\lambda_{2\mathbf{q}-\mathbf{k}}^{(3)} \end{pmatrix} \tilde{\Psi}_{\mathbf{k}} + \lambda_{-\mathbf{k}}^{(3)}. \tag{1.29}$$

A.3 On-site interaction term $\mathcal{H}_{\mathrm{os}}$ in momentum space

The on-site interaction term

$$\mathcal{H}_{\mathrm{os}} = -U \sum_{j} \hat{n}_{j\uparrow}^{a} \hat{n}_{j\downarrow}^{a}. \tag{1.30}$$

On-site interaction term $\mathcal{H}_{os}$ in the mean-field approximation

As we use the definition of number operator and employ fermionic anti-commutation relations, we obtain

$$\begin{aligned}\hat{n}_{j\uparrow}^{a} \hat{n}_{j\downarrow}^{a} &= \hat{a}_{j\uparrow}^{\dagger} \hat{a}_{j\uparrow} \hat{a}_{j\downarrow}^{\dagger} \hat{a}_{j\downarrow} \\ &= \hat{a}_{j\uparrow}^{\dagger} \hat{a}_{j\downarrow}^{\dagger} \hat{a}_{j\downarrow} \hat{a}_{j\uparrow}. \end{aligned} \tag{1.31}$$

By making the mean field approximation, we obtain

$$\hat{n}^a_{j\uparrow}\hat{n}^a_{j\downarrow} = \langle \hat{a}^\dagger_{j\uparrow}\hat{a}^\dagger_{j\downarrow}\rangle \hat{a}_{j\downarrow}\hat{a}_{j\uparrow} + \langle \hat{a}_{j\downarrow}\hat{a}_{j\uparrow}\rangle \hat{a}^\dagger_{j\uparrow}\hat{a}^\dagger_{j\downarrow} - \langle \hat{a}^\dagger_{j\uparrow}\hat{a}^\dagger_{j\downarrow}\rangle\langle \hat{a}_{j\downarrow}\hat{a}_{j\uparrow}\rangle. \tag{1.32}$$

We choose to use the ansatz

$$U\langle \hat{a}_{j\downarrow}\hat{a}_{j\uparrow}\rangle = \Delta_0 e^{2i\mathbf{q}\cdot\mathbf{x}_j}, \tag{1.33}$$

where $\Delta_0 \geq 0$ and $\mathbf{q}$ is the FFLO momentum. We also assume that $\mathbf{q}$ belongs to the Brillouin zone k-point mesh and points to the direction of positive y-axis. Anyway, by using Eqs. (1.32) and (1.33), we cast Eq. (1.30) into the form

$$\mathcal{H}^{\text{MF}}_{\text{os}} = -\sum_j \left(\Delta_0 e^{-2i\mathbf{q}\cdot\mathbf{x}_j}\hat{a}_{j\downarrow}\hat{a}_{j\uparrow} + \text{h.c.}\right) + \sum_j \frac{\Delta_0^2}{U}. \tag{1.34}$$

Employing the inverse Fourier transformation, we obtain

$$\begin{aligned}
\sum_j e^{-2i\mathbf{q}\cdot\mathbf{x}_j}\hat{a}_{j\downarrow}\hat{a}_{j\uparrow} &= \frac{1}{M}\sum_j e^{-2i\mathbf{q}\cdot\mathbf{x}_j}\left(\sum_{\mathbf{k}} e^{i\mathbf{k}\cdot\mathbf{x}_j}\tilde{a}_{\mathbf{k}\downarrow}\right)\left(\sum_{\mathbf{k}'} e^{i\mathbf{k}'\cdot\mathbf{x}_j}\tilde{a}_{\mathbf{k}'\uparrow}\right) \\
&= \frac{1}{M}\sum_{\mathbf{k},\mathbf{k}'}\left(\sum_j e^{i\mathbf{x}_j\cdot(\mathbf{k}+\mathbf{k}'-2\mathbf{q})}\right)\tilde{a}_{\mathbf{k}\downarrow}\tilde{a}_{\mathbf{k}'\uparrow} \\
&= \sum_{\mathbf{k}} \tilde{a}_{2\mathbf{q}-\mathbf{k}\downarrow}\tilde{a}_{\mathbf{k}\uparrow}.
\end{aligned} \tag{1.35}$$

Let us now substitute Eq. (1.35) into Eq. (1.34). Furthermore, let us manipulate the last term at the right-hand side of Eq. (1.34) by using the fact that the number of k-points is equal to the number of sites in sublattice A. Subsequently, we obtain

$$\mathcal{H}^{\text{MF}}_{\text{os}} = -\Delta_0\sum_{\mathbf{k}}\left(\tilde{a}_{2\mathbf{q}-\mathbf{k}\downarrow}\tilde{a}_{\mathbf{k}\uparrow} + \text{h.c.}\right) + \sum_{\mathbf{k}}\frac{\Delta_0^2}{U}. \tag{1.36}$$

Interaction term $\mathcal{H}^{MF}_{os}$ in the basis $\tilde{\Psi}_{\mathbf{k}}$
We recall that $\begin{pmatrix}\hat{c}^{(1)}_{\mathbf{k}} & \hat{c}^{(2)}_{\mathbf{k}} & \hat{c}^{(3)}_{\mathbf{k}}\end{pmatrix}^{\mathbf{T}} = \bar{U}^\dagger\tilde{\Phi}_{\mathbf{k}}$, where $\tilde{\Phi}_{\mathbf{k}} = \begin{pmatrix}\tilde{a}_{\mathbf{k}\uparrow} & \tilde{b}_{\mathbf{k}\uparrow} & \tilde{a}_{\mathbf{k}\downarrow}\end{pmatrix}^{\mathbf{T}}$. Multiplying both sides by $\bar{U}$, we obtain

$$\tilde{a}_{\mathbf{k}\uparrow} = \bar{U}_{11}\hat{c}^{(1)}_{\mathbf{k}} + \bar{U}_{12}\hat{c}^{(2)}_{\mathbf{k}} + \bar{U}_{13}\hat{c}^{(3)}_{\mathbf{k}}, \tag{1.37}$$

$$\tilde{b}_{\mathbf{k}\uparrow} = \bar{U}_{21}\hat{c}^{(1)}_{\mathbf{k}} + \bar{U}_{22}\hat{c}^{(2)}_{\mathbf{k}} + \bar{U}_{23}\hat{c}^{(3)}_{\mathbf{k}}, \tag{1.38}$$

$$\tilde{a}_{\mathbf{k}\downarrow} = \bar{U}_{31}\hat{c}^{(1)}_{\mathbf{k}} + \bar{U}_{32}\hat{c}^{(2)}_{\mathbf{k}} + \bar{U}_{33}\hat{c}^{(3)}_{\mathbf{k}}. \tag{1.39}$$

Using Eq. (1.24), we obtain

$$\tilde{a}_{\mathbf{k}\uparrow} = \frac{1}{\sqrt{2}}\hat{c}^{(1)}_{\mathbf{k}} + \frac{1}{\sqrt{2}}\hat{c}^{(2)}_{\mathbf{k}}, \tag{1.40}$$

$$\tilde{b}_{\mathbf{k}\uparrow} = \frac{\exp(-i\phi_{\mathbf{k}})}{\sqrt{2}}\hat{c}^{(1)}_{\mathbf{k}} - \frac{\exp(-i\phi_{\mathbf{k}})}{\sqrt{2}}\hat{c}^{(2)}_{\mathbf{k}}, \tag{1.41}$$

$$\tilde{a}_{\mathbf{k}\downarrow} = \hat{c}^{(3)}_{\mathbf{k}}. \tag{1.42}$$

By using Eqs. (1.40) and (1.42), we obtain

$$\sum_{\mathbf{k}} \tilde{a}_{2\mathbf{q}-\mathbf{k}\downarrow}\tilde{a}_{\mathbf{k}\uparrow} = \sum_{\mathbf{k}} \frac{1}{\sqrt{2}}\hat{c}^{(3)}_{2\mathbf{q}-\mathbf{k}}\hat{c}^{(1)}_{\mathbf{k}} + \sum_{\mathbf{k}} \frac{1}{\sqrt{2}}\hat{c}^{(3)}_{2\mathbf{q}-\mathbf{k}}\hat{c}^{(2)}_{\mathbf{k}}. \tag{1.43}$$

In order to simplify notation, we define a coupling function

$$g_{\mathbf{k}} = -\frac{\Delta_0}{\sqrt{2}}. \tag{1.44}$$

Let us now multiply both sides of Eq. (1.43) by $-\Delta_0$ and employ Eq. (1.44). We obtain

$$-\Delta_0 \sum_{\mathbf{k}} \tilde{a}_{2\mathbf{q}-\mathbf{k}\downarrow}\tilde{a}_{\mathbf{k}\uparrow} = \sum_{\mathbf{k}} g_{\mathbf{k}}\hat{c}^{(3)}_{2\mathbf{q}-\mathbf{k}}\hat{c}^{(1)}_{\mathbf{k}} + \sum_{\mathbf{k}} g_{\mathbf{k}}\hat{c}^{(3)}_{2\mathbf{q}-\mathbf{k}}\hat{c}^{(2)}_{\mathbf{k}}. \tag{1.45}$$

By using Eq. (1.45) we cast Eq. (1.36) into form

$$\mathcal{H}^{\text{MF}}_{\text{os}} = \sum_{\mathbf{k}} \left(g_{\mathbf{k}}\hat{c}^{(3)}_{2\mathbf{q}-\mathbf{k}}\hat{c}^{(1)}_{\mathbf{k}} + g_{\mathbf{k}}\hat{c}^{(3)}_{2\mathbf{q}-\mathbf{k}}\hat{c}^{(2)}_{\mathbf{k}} + \text{h.c.} + \frac{\Delta_0^2}{U} \right). \tag{1.46}$$

Hence, in the basis $\tilde{\Psi}_{\mathbf{k}} = \begin{pmatrix} \hat{c}^{(1)}_{\mathbf{k}} & \hat{c}^{(2)}_{\mathbf{k}} & \hat{c}^{(3)\dagger}_{2\mathbf{q}-\mathbf{k}} \end{pmatrix}^{\text{T}}$

$$\mathcal{H}^{\text{MF}}_{\text{os}} = \sum_{\mathbf{k}} \tilde{\Psi}^{\dagger}_{\mathbf{k}} \begin{pmatrix} 0 & 0 & g^*_{\mathbf{k}} \\ 0 & 0 & g^*_{\mathbf{k}} \\ g_{\mathbf{k}} & g_{\mathbf{k}} & 0 \end{pmatrix} \tilde{\Psi}_{\mathbf{k}} + \sum_{\mathbf{k}} \frac{\Delta_0^2}{U}. \tag{1.47}$$

A.4 Nearest-neighbor interaction term $\mathcal{H}_{\mathrm{nn}}$

A.4.1 Nearest-neighbor interaction term in the mean-field approximation

In Publication IV we took the nearest-neighbor (NN) interaction term to be

$$\mathcal{H}_{\mathrm{nn}} = -V \sum_{\langle m,n\rangle \in \mathcal{L}_{\downarrow}} \hat{h}^{\dagger}_{mn} \hat{h}_{mn}, \tag{1.48}$$

where

$$\hat{h}^{\dagger}_{mn} = (\hat{a}^{\dagger}_{m\uparrow}\hat{a}^{\dagger}_{n\downarrow} - \hat{a}^{\dagger}_{m\downarrow}\hat{a}^{\dagger}_{n\uparrow})/\sqrt{2}. \tag{1.49}$$

In the mean-field approximation

$$\mathcal{H}^{\mathrm{MF}}_{\mathrm{nn}} = -V \sum_{\langle m,n\rangle \in \mathcal{L}_{\downarrow}} \langle \hat{h}_{mn}\rangle \hat{h}^{\dagger}_{mn} + \langle \hat{h}^{\dagger}_{mn}\rangle \hat{h}_{mn} - |\langle \hat{h}_{mn}\rangle|^2. \tag{1.50}$$

For the sake of comparison, let us consider the nearest-neighbor interaction term

$$H_{\mathrm{nn}} = -V \sum_{\sigma} \sum_{\langle m,n\rangle} a^{\dagger}_{m,\sigma} a_{m,\sigma} a^{\dagger}_{n,-\sigma} a_{n,-\sigma}, \tag{1.51}$$

which has an easy physical interpretation being of a similar form as the contact interaction but now for neighboring lattice sites. Using anticommutation relations, we easily obtain

$$H_{\mathrm{nn}} = -V \sum_{\sigma} \sum_{\langle m,n\rangle} a^{\dagger}_{m,\sigma} a^{\dagger}_{n,-\sigma} a_{n,-\sigma} a_{m,\sigma}. \tag{1.52}$$

In the mean-field approximation

$$H^{\mathrm{MF}}_{\mathrm{nn}} = -V \sum_{\sigma} \sum_{\langle m,n\rangle} \langle a_{n,-\sigma} a_{m,\sigma}\rangle a^{\dagger}_{m,\sigma} a^{\dagger}_{n,-\sigma} + \text{h.c.} - |\langle a_{n,-\sigma} a_{m,\sigma}\rangle|^2. \tag{1.53}$$

Let us follow the example of Ref. [43] and assume that the nearest-neighbor attraction leads to spin-singlet pairing. Accordingly, we say that the order parameter

$$\langle a_{n\uparrow} a_{m\downarrow}\rangle = -\langle a_{n\downarrow} a_{m\uparrow}\rangle. \tag{1.54}$$

To be more precise, we obtain Eq. (1.54) by using fermionic anticommutation relations and switching the site indices m and n. We assume that switching the site indices m and n does not change the value of the expression. Subsequently, we obtain

$$H_{\mathrm{nn}}^{\mathrm{MF}} = -V \sum_{\langle m,n \rangle} \langle a_{n\downarrow} a_{m\uparrow} \rangle (a_{m\uparrow}^{\dagger} a_{n\downarrow}^{\dagger} - a_{m\downarrow}^{\dagger} a_{n\uparrow}^{\dagger}) + \text{h.c.} - 2|\langle a_{n\downarrow} a_{m\uparrow} \rangle|^2. \quad (1.55)$$

With the help of the spin-singlet creation operator $\hat{h}_{mn}^{\dagger}$ defined in Eq. (1.49) we cast Eq. (1.55) into the form

$$H_{\mathrm{nn}}^{\mathrm{MF}} = -V \sum_{\langle m,n \rangle} \sqrt{2} \langle a_{n\downarrow} a_{m\uparrow} \rangle \hat{h}_{mn}^{\dagger} + \sqrt{2} \langle a_{n\downarrow} a_{m\uparrow} \rangle^{*} \hat{h}_{mn} - 2|\langle a_{n\downarrow} a_{m\uparrow} \rangle|^2. \quad (1.56)$$

It is now easy to see that the interaction terms $\mathcal{H}_{\mathrm{nn}}^{\mathrm{MF}}$ and $H_{\mathrm{nn}}^{\mathrm{MF}}$ given by Eqs. (1.50) and (1.56) are the same if we choose the order parameters to be $V\langle \hat{h}_{mn} \rangle$ and $\sqrt{2} V \langle a_{n\downarrow} a_{m\uparrow} \rangle$.

Ansatz for the order parameter $V\langle \hat{h}_{mn} \rangle$

As explained in Ref. [112], there are three different nearest-neighbor bonds in a triangular lattice. Subsequently, I use an ansatz having the same norm $|V\langle \hat{h}_{mn} \rangle| = |\Delta_1|$ along all bonds, but three different phases being allowed along three kinds of bonds. Moreover, I take the center-of-mass momentum of Cooper pairs to be the same as in on-site pairing [cf. Eq. (1.33)]. In equation form, the ansatz reads

$$V\langle \hat{h}_{mn} \rangle = \Delta_1 e^{i\theta_{mn}} e^{i\mathbf{q}\cdot(\mathbf{x}_m + \mathbf{x}_n)}, \quad (1.57)$$

where $\Delta_1 \in \mathbb{R}$ and θ_{mn} is the phase that depends on the direction of the bond between sites m and n. Finally, we note that whatever ansatz one uses for the order parameter $V\langle \hat{h}_{mn} \rangle$, it must be symmetric with respect to the indices m and n because $\hat{h}_{mn}$ is symmetric with respect to m and n.

A.4.2 Mean-field Hamiltonian $\mathcal{H}_{\mathrm{nn}}^{\mathrm{MF}}$ in momentum space

I choose the three different nearest-neighbor bonds to be $\mathbf{a}_2$, $\mathbf{a}_1$ and $\mathbf{a}_1 - \mathbf{a}_2$, and denote the phases θ_{mn} corresponding to those bonds by θ, ϕ, φ, respectively (cf. Fig. 1 in Publication IV). Furthermore, I denote the spin-singlet creation operator corresponding to the bond between $\mathbf{x}_m$ and $\mathbf{x}_m +$

$\mathbf{a}_1$ by $\hat{h}^\dagger_m(\mathbf{a}_1)$. Using similar notation for the other two bonds, we obtain

$$-V\sum_{\langle m,n\rangle}\langle\hat{h}_{mn}\rangle\hat{h}^\dagger_{mn} = -\Delta_1\sum_{m\in\mathcal{L}_\downarrow}\left[e^{i\theta}e^{i\mathbf{q}\cdot(2\mathbf{x}_m+\mathbf{a}_2)}\hat{h}^\dagger_m(\mathbf{a}_2)+e^{i\phi}e^{i\mathbf{q}\cdot(2\mathbf{x}_m+\mathbf{a}_1)}\hat{h}^\dagger_m(\mathbf{a}_1)\right.$$
$$\left.+\,e^{i\varphi}e^{i\mathbf{q}\cdot(2\mathbf{x}_m+\mathbf{a}_1-\mathbf{a}_2)}\hat{h}^\dagger_m(\mathbf{a}_1-\mathbf{a}_2)\right]. \qquad (1.58)$$

Let us first express $\sum_{m\in\mathcal{L}_\downarrow}e^{i\mathbf{q}\cdot(2\mathbf{x}_m+\mathbf{a}_2)}\hat{h}^\dagger_m(\mathbf{a}_2)$ in terms of momentum space operators. Employing inverse Fourier transformation, we obtain

$$\begin{aligned}\sum_{m\in\mathcal{L}_\downarrow}e^{i\mathbf{q}\cdot(2\mathbf{x}_m+\mathbf{a}_2)}\hat{a}^\dagger_\uparrow(\mathbf{x}_m)\hat{a}^\dagger_\downarrow(\mathbf{x}_m+\mathbf{a}_2) &= \frac{1}{M}\sum_{m\in\mathcal{L}_\downarrow}e^{i\mathbf{q}\cdot(2\mathbf{x}_m+\mathbf{a}_2)}\left(\sum_{\mathbf{k}}e^{-i\mathbf{k}\cdot\mathbf{x}_m}\tilde{a}^\dagger_{\mathbf{k}\uparrow}\right)\\ &\quad\times\left(\sum_{\mathbf{k}'}e^{-i\mathbf{k}'\cdot(\mathbf{x}_m+\mathbf{a}_2)}\tilde{a}^\dagger_{\mathbf{k}'\downarrow}\right)\\ &= e^{-i\mathbf{q}\cdot\mathbf{a}_2}\sum_{\mathbf{k}}e^{i\mathbf{k}\cdot\mathbf{a}_2}\tilde{a}^\dagger_{\mathbf{k}\uparrow}\tilde{a}^\dagger_{2\mathbf{q}-\mathbf{k}\downarrow}. \qquad (1.59)\end{aligned}$$

In a similar way, we obtain for the case of $\downarrow\uparrow$ (instead of $\uparrow\downarrow$)

$$\begin{aligned}\sum_{m\in\mathcal{L}_\downarrow}e^{i\mathbf{q}\cdot(2\mathbf{x}_m+\mathbf{a}_2)}\hat{a}^\dagger_\downarrow(\mathbf{x}_m)\hat{a}^\dagger_\uparrow(\mathbf{x}_m+\mathbf{a}_2) &= \frac{1}{M}\sum_{m\in\mathcal{L}_\downarrow}e^{i\mathbf{q}\cdot(2\mathbf{x}_m+\mathbf{a}_2)}\left(\sum_{\mathbf{k}}e^{-i\mathbf{k}\cdot\mathbf{x}_m}\tilde{a}^\dagger_{\mathbf{k}\downarrow}\right)\\ &\quad\times\left(\sum_{\mathbf{k}'}e^{-i\mathbf{k}'\cdot(\mathbf{x}_m+\mathbf{a}_2)}\tilde{a}^\dagger_{\mathbf{k}'\uparrow}\right)\\ &= e^{i\mathbf{q}\cdot\mathbf{a}_2}\sum_{\mathbf{k}'}e^{-i\mathbf{k}'\cdot\mathbf{a}_2}\tilde{a}^\dagger_{2\mathbf{q}-\mathbf{k}'\downarrow}\tilde{a}^\dagger_{\mathbf{k}'\uparrow}\\ &= -e^{i\mathbf{q}\cdot\mathbf{a}_2}\sum_{\mathbf{k}'}e^{-i\mathbf{k}'\cdot\mathbf{a}_2}\tilde{a}^\dagger_{\mathbf{k}'\uparrow}\tilde{a}^\dagger_{2\mathbf{q}-\mathbf{k}'\downarrow}. \qquad (1.60)\end{aligned}$$

By using Eqs. (1.49), (1.59) and (1.60), we obtain

$$\begin{aligned}\sum_{m\in\mathcal{L}_\downarrow}e^{i\mathbf{q}\cdot(2\mathbf{x}_m+\mathbf{a}_2)}\hat{h}^\dagger_m(\mathbf{a}_2) &= \sum_{\mathbf{k}}\frac{e^{-i\mathbf{q}\cdot\mathbf{a}_2}e^{i\mathbf{k}\cdot\mathbf{a}_2}+e^{i\mathbf{q}\cdot\mathbf{a}_2}e^{-i\mathbf{k}\cdot\mathbf{a}_2}}{\sqrt{2}}\tilde{a}^\dagger_{\mathbf{k}\uparrow}\tilde{a}^\dagger_{2\mathbf{q}-\mathbf{k}\downarrow}\\ &= \sum_{\mathbf{k}}\sqrt{2}\cos\left[(\mathbf{k}-\mathbf{q})\cdot\mathbf{a}_2\right]\tilde{a}^\dagger_{\mathbf{k}\uparrow}\tilde{a}^\dagger_{2\mathbf{q}-\mathbf{k}\downarrow}. \qquad (1.61)\end{aligned}$$

Let us define a coupling function

$$\mathcal{W}_{\mathbf{r}}(\mathbf{k}) = \sqrt{2}\cos\left(\mathbf{k}\cdot\mathbf{r}\right). \qquad (1.62)$$

By employing Eq. (1.62), we cast Eq. (1.61) into the form

$$\sum_{m\in\mathcal{L}_\downarrow}e^{i\mathbf{q}\cdot(2\mathbf{x}_m+\mathbf{a}_2)}\hat{h}^\dagger_m(\mathbf{a}_2) = \sum_{\mathbf{k}}\mathcal{W}_{\mathbf{a}_2}(\mathbf{k}-\mathbf{q})\tilde{a}^\dagger_{\mathbf{k}\uparrow}\tilde{a}^\dagger_{2\mathbf{q}-\mathbf{k}\downarrow}. \qquad (1.63)$$

It is easy to see that Eq. (1.63) remains valid if we replace $\mathbf{a}_2$ by $\mathbf{a}_1$ or $\mathbf{a}_1 - \mathbf{a}_2$. Consequently, we can cast Eq. (1.58) into the form

$$-V \sum_{\langle m,n \rangle} \langle \hat{h}_{mn} \rangle \hat{h}^{\dagger}_{mn} = -\Delta_1 \sum_{\mathbf{k}} \big[e^{i\theta} \mathcal{W}_{\mathbf{a}_2}(\mathbf{k}-\mathbf{q}) + e^{i\phi} \mathcal{W}_{\mathbf{a}_1}(\mathbf{k}-\mathbf{q}) + e^{i\varphi} \mathcal{W}_{\mathbf{a}_1-\mathbf{a}_2}(\mathbf{k}-\mathbf{q}) \big] \tilde{a}^{\dagger}_{\mathbf{k}\uparrow} \tilde{a}^{\dagger}_{2\mathbf{q}-\mathbf{k}\downarrow}. \quad (1.64)$$

Taking Hermitian adjoint of both sides, we obtain

$$-V \sum_{\langle m,n \rangle} \langle \hat{h}_{mn} \rangle^{*} \hat{h}_{mn} = -\Delta_1 \sum_{\mathbf{k}} \big[e^{-i\theta} \mathcal{W}_{\mathbf{a}_2}(\mathbf{k}-\mathbf{q}) + e^{-i\phi} \mathcal{W}_{\mathbf{a}_1}(\mathbf{k}-\mathbf{q}) + e^{-i\varphi} \mathcal{W}_{\mathbf{a}_1-\mathbf{a}_2}(\mathbf{k}-\mathbf{q}) \big] \tilde{a}_{2\mathbf{q}-\mathbf{k}\downarrow} \tilde{a}_{\mathbf{k}\uparrow}. \quad (1.65)$$

Nearest-neighbor interaction term in the basis $\tilde{\Psi}_{\mathbf{k}}$

By using Eqs. (1.40) and (1.42), we obtain

$$\tilde{a}_{2\mathbf{q}-\mathbf{k}\downarrow} \tilde{a}_{\mathbf{k}\uparrow} = \frac{1}{\sqrt{2}} \hat{c}^{(3)}_{2\mathbf{q}-\mathbf{k}} \hat{c}^{(1)}_{\mathbf{k}} + \frac{1}{\sqrt{2}} \hat{c}^{(3)}_{2\mathbf{q}-\mathbf{k}} \hat{c}^{(2)}_{\mathbf{k}}. \quad (1.66)$$

In order to simplify notation, we define a coupling function

$$\mathcal{G}_{\mathbf{k},\mathbf{q}} = -\frac{\Delta_1}{\sqrt{2}} \big[e^{-i\theta} \mathcal{W}_{\mathbf{a}_2}(\mathbf{k}-\mathbf{q}) + e^{-i\phi} \mathcal{W}_{\mathbf{a}_1}(\mathbf{k}-\mathbf{q}) + e^{-i\varphi} \mathcal{W}_{\mathbf{a}_1-\mathbf{a}_2}(\mathbf{k}-\mathbf{q}) \big]. \quad (1.67)$$

By using Eqs. (1.66) and (1.67), we cast Eq. (1.65) into the form

$$-V \sum_{\langle m,n \rangle} \langle \hat{h}_{mn} \rangle^{*} \hat{h}_{mn} = \sum_{\mathbf{k}} \mathcal{G}_{\mathbf{k},\mathbf{q}} \hat{c}^{(3)}_{2\mathbf{q}-\mathbf{k}} \hat{c}^{(1)}_{\mathbf{k}} + \mathcal{G}_{\mathbf{k},\mathbf{q}} \hat{c}^{(3)}_{2\mathbf{q}-\mathbf{k}} \hat{c}^{(2)}_{\mathbf{k}}. \quad (1.68)$$

By using Eqs. (1.57) and (1.68), we write Eq. (1.50) into the form

$$\mathcal{H}^{\text{MF}}_{\text{nn}} = \sum_{\mathbf{k}} \left(\mathcal{G}_{\mathbf{k},\mathbf{q}} \hat{c}^{(3)}_{2\mathbf{q}-\mathbf{k}} \hat{c}^{(1)}_{\mathbf{k}} + \mathcal{G}_{\mathbf{k},\mathbf{q}} \hat{c}^{(3)}_{2\mathbf{q}-\mathbf{k}} \hat{c}^{(2)}_{\mathbf{k}} + \text{h.c.} + \frac{3|\Delta_1|^2}{V} \right). \quad (1.69)$$

Hence, in the basis $\tilde{\Psi}_{\mathbf{k}} = \begin{pmatrix} \hat{c}^{(1)}_{\mathbf{k}} & \hat{c}^{(2)}_{\mathbf{k}} & \hat{c}^{(3)\dagger}_{2\mathbf{q}-\mathbf{k}} \end{pmatrix}^{\mathbf{T}}$

$$\mathcal{H}^{\text{MF}}_{\text{nn}} = \sum_{\mathbf{k}} \tilde{\Psi}^{\dagger}_{\mathbf{k}} \begin{pmatrix} 0 & 0 & \mathcal{G}^{*}_{\mathbf{k},\mathbf{q}} \\ 0 & 0 & \mathcal{G}^{*}_{\mathbf{k},\mathbf{q}} \\ \mathcal{G}_{\mathbf{k},\mathbf{q}} & \mathcal{G}_{\mathbf{k},\mathbf{q}} & 0 \end{pmatrix} \tilde{\Psi}_{\mathbf{k}} + \sum_{\mathbf{k}} \frac{3|\Delta_1|^2}{V}. \quad (1.70)$$

A.5 Full mean-field Hamiltonian in the basis $\tilde{\Psi}_{\mathbf{k}}$

The mean-field Hamiltonian without nearest-neighbor interaction term is given by Eqs. (1.29) and (1.47). By using Eq. (1.70) in addition to them, we can write down the full mean-field Hamiltonian $\mathcal{H}^{\text{MF}} = \mathcal{H}_0 + \mathcal{H}^{\text{MF}}_{\text{os}} + \mathcal{H}^{\text{MF}}_{\text{nn}}$. It reads

$$\mathcal{H}^{\text{MF}} = \sum_{\mathbf{k}} \tilde{\Psi}^{\dagger}_{\mathbf{k}} H_{\mathbf{k}} \tilde{\Psi}_{\mathbf{k}} + \frac{3|\Delta_1|^2}{V} + \frac{\Delta_0^2}{U_0} + \lambda^{(3)}_{-\mathbf{k}}, \tag{1.71}$$

where

$$H_{\mathbf{k}} = \begin{pmatrix} \lambda^{(1)}_{\mathbf{k}} & 0 & g^*_{\mathbf{k}} + \mathcal{G}^*_{\mathbf{k},\mathbf{q}} \\ 0 & \lambda^{(2)}_{\mathbf{k}} & g^*_{\mathbf{k}} + \mathcal{G}^*_{\mathbf{k},\mathbf{q}} \\ g_{\mathbf{k}} + \mathcal{G}_{\mathbf{k},\mathbf{q}} & g_{\mathbf{k}} + \mathcal{G}_{\mathbf{k},\mathbf{q}} & -\lambda^{(3)}_{2\mathbf{q}-\mathbf{k}} \end{pmatrix}. \tag{1.72}$$

B. Triangular lattice

In this Appendix, I present analytical calculations related to the triangular lattice of Publication IV.

B.1 Preliminary results

By writing "S" in front of an equation number, we refer to Ref. [71]. For example, by (S5) we mean Eq. (5) of Ref. [71]. By writing "L" in front of an equation number, we refer to Ref. [105]. For example, by (L16) we mean Eq. (16) of Ref. [105]. Moreover, we will use the same Fourier transformation as in Appendix A.

B.1.1 Defining the full Hamiltonian

We take the noninteracting part of the Hamiltonian to be

$$\begin{aligned}\mathcal{H}_0 &= -t_\uparrow \sum_{\langle i,j\rangle} (\hat{a}^\dagger_{i\uparrow}\hat{a}_{j\uparrow} + \text{H.c.}) - t_\downarrow \sum_{\langle i,j\rangle} (\hat{a}^\dagger_{i\downarrow}\hat{a}_{j\downarrow} + \text{H.c.}) - \mu_\uparrow \sum_i \hat{n}^a_{i\uparrow} \\ &\quad - \mu_\downarrow \sum_i \hat{n}^a_{i\downarrow}, \end{aligned} \tag{2.1}$$

where $\sum_{\langle i,j\rangle}$ means summation over distinct nearest-neighbor pairs. On the other hand, we represent the on-site interaction with the term

$$\mathcal{H}_{\text{os}} = -U \sum_i \hat{n}^a_{i\uparrow}\hat{n}^a_{i\downarrow}. \tag{2.2}$$

The nearest-neighbor interaction is taken into account with the term

$$\mathcal{H}_{\text{nn}} = -V \sum_{\langle m,n\rangle} \hat{h}^\dagger_{mn}\hat{h}_{mn}, \tag{2.3}$$

where $\hat{h}^\dagger_{mn} = (\hat{a}^\dagger_{m\uparrow}\hat{a}^\dagger_{n\downarrow} - \hat{a}^\dagger_{m\downarrow}\hat{a}^\dagger_{n\uparrow})/\sqrt{2}$ is the spin-singlet creation operator. The full Hamiltonian

$$\mathcal{H} = \mathcal{H}_0 + \mathcal{H}_{\rm os} + \mathcal{H}_{\rm nn}. \tag{2.4}$$

B.2 Noninteracting Hamiltonian $\mathcal{H}_0$ in momentum space

Fourier transformation of number operator terms
We easily obtain

$$\sum_i n^a_{i\sigma} \;\; = \;\; \sum_i a^\dagger_{i\sigma} a_{i\sigma} = \sum_{\mathbf{k}} \tilde{a}^\dagger_{\mathbf{k}\sigma}\tilde{a}_{\mathbf{k}\sigma}, \tag{2.5}$$

where the spin-index $\sigma \in \{\uparrow, \downarrow\}$.

Identifying the tight-binding Hamiltonians $\hat{H}_{0\downarrow}$ and $\hat{H}_{0\uparrow}$
Tight-binding Hamiltonian for the $\downarrow$-component reads

$$\hat{H}_{0\downarrow} = -t_\downarrow \sum_{\langle i,j\rangle} a^\dagger_{i\downarrow} a_{j\downarrow} + \text{H.c.} \tag{2.6}$$

By using Eqs. (L34) and (L36), we obtain

$$\hat{H}_{0\downarrow} = \sum_{\mathbf{k}} \tilde{\Phi}^\dagger_{\mathbf{k}} \begin{pmatrix} 0 & 0 \\ 0 & E_\downarrow(\mathbf{k}) \end{pmatrix} \tilde{\Phi}_{\mathbf{k}}, \tag{2.7}$$

where

$$\tilde{\Phi}_{\mathbf{k}} = \begin{pmatrix} \tilde{a}_{\mathbf{k}\uparrow} & \tilde{a}_{\mathbf{k}\downarrow} \end{pmatrix}^{\rm T} \tag{2.8}$$

and

$$E_\downarrow(\mathbf{k}) = -2t_\downarrow \left[\cos k_y + \cos\left(\frac{\sqrt{3}k_x + k_y}{2} \right) + \cos\left(\frac{k_y - \sqrt{3}k_x}{2} \right) \right]. \tag{2.9}$$

The tight-binding Hamiltonian for the $\uparrow$-component reads

$$\hat{H}_{0\uparrow} = -t_\uparrow \sum_{\langle i,j\rangle} a^\dagger_{i\uparrow} a_{j\uparrow} + \text{H.c.} \tag{2.10}$$

From Eqs. (2.6) and (2.10) we see that the tight-binding Hamiltonians for the $\downarrow$-spin and $\uparrow$-spin components are the same. Thus we immediately

obtain

$$\hat{H}_{0\uparrow} = \sum_{\mathbf{k}} \tilde{\Phi}^{\dagger}_{\mathbf{k}} \begin{pmatrix} E_{\downarrow}(\mathbf{k}) & 0 \\ 0 & 0 \end{pmatrix} \tilde{\Phi}_{\mathbf{k}}. \tag{2.11}$$

Noninteracting part $\mathcal{H}_0$ in a new basis $\tilde{\Psi}_{\mathbf{k}}$

By using Eqs. (2.5), (2.6) and (2.10), we cast Eq. (2.1) into the form

$$\mathcal{H}_0 = \hat{H}_{0\uparrow} + \hat{H}_{0\downarrow} - \mu_{\uparrow} \sum_{\mathbf{k}} \tilde{a}^{\dagger}_{\mathbf{k}\uparrow} \tilde{a}_{\mathbf{k}\uparrow} - \mu_{\downarrow} \sum_{\mathbf{k}} \tilde{a}^{\dagger}_{\mathbf{k}\downarrow} \tilde{a}_{\mathbf{k}\downarrow}. \tag{2.12}$$

By using Eqs. (2.7) and (2.11), Eq. (2.12) becomes

$$\mathcal{H}_0 = \sum_{\mathbf{k}} (E_{\downarrow}(\mathbf{k}) - \mu_{\uparrow}) \tilde{a}^{\dagger}_{\mathbf{k}\uparrow} \tilde{a}_{\mathbf{k}\uparrow} + \sum_{\mathbf{k}} (E_{\downarrow}(\mathbf{k}) - \mu_{\downarrow}) \tilde{a}^{\dagger}_{\mathbf{k}\downarrow} \tilde{a}_{\mathbf{k}\downarrow}. \tag{2.13}$$

In order to simplify notation, we define

$$\lambda^{(1)}_{\mathbf{k}} = E_{\downarrow}(\mathbf{k}) - \mu_{\uparrow} \tag{2.14}$$

$$\lambda^{(2)}_{\mathbf{k}} = E_{\downarrow}(\mathbf{k}) - \mu_{\downarrow}. \tag{2.15}$$

Subsequently, we obtain

$$\mathcal{H}_0 = \sum_{\mathbf{k}} \lambda^{(1)}_{\mathbf{k}} \tilde{a}^{\dagger}_{\mathbf{k}\uparrow} \tilde{a}_{\mathbf{k}\uparrow} + \sum_{\mathbf{k}} \lambda^{(2)}_{\mathbf{k}} \tilde{a}^{\dagger}_{\mathbf{k}\downarrow} \tilde{a}_{\mathbf{k}\downarrow}. \tag{2.16}$$

Let us now employ a fermionic anticommutation relation and thereby switch the order of operators in the last term. Furthermore, let us assume that $\mathbf{q}$ belongs to the Brillouin zone k-point mesh and make the change of variables $\mathbf{k} \to 2\mathbf{q} - \mathbf{k}$ in the last summation. Subsequently, we obtain

$$\mathcal{H}_0 = \sum_{\mathbf{k}} \lambda^{(1)}_{\mathbf{k}} \tilde{a}^{\dagger}_{\mathbf{k}\uparrow} \tilde{a}_{\mathbf{k}\uparrow} - \sum_{\mathbf{k}} \lambda^{(2)}_{2\mathbf{q}-\mathbf{k}} \tilde{a}_{2\mathbf{q}-\mathbf{k},\downarrow} \tilde{a}^{\dagger}_{2\mathbf{q}-\mathbf{k},\downarrow} + \sum_{\mathbf{k}} \lambda^{(2)}_{\mathbf{k}}. \tag{2.17}$$

Let us define a new basis

$$\tilde{\Psi}_{\mathbf{k}} = \begin{pmatrix} \tilde{a}_{\mathbf{k}\uparrow} & \tilde{a}^{\dagger}_{2\mathbf{q}-\mathbf{k},\downarrow} \end{pmatrix}^{\mathrm{T}}. \tag{2.18}$$

Subsequently, it is easy to see that

$$\mathcal{H}_0 = \sum_{\mathbf{k}} \tilde{\Psi}^{\dagger}_{\mathbf{k}} \mathbf{H}^{(0)}_{\mathbf{k}} \tilde{\Psi}_{\mathbf{k}} + \sum_{\mathbf{k}} \lambda^{(2)}_{\mathbf{k}} \tag{2.19}$$

with

$$\mathbf{H}_{\mathbf{k}}^{(0)} = \begin{pmatrix} \lambda_{\mathbf{k}}^{(1)} & 0 \\ 0 & -\lambda_{2\mathbf{q}-\mathbf{k}}^{(2)} \end{pmatrix}. \tag{2.20}$$

We conclude by noting that $E_{\downarrow}(\mathbf{k}) - \mu_{\downarrow} = \xi_{\downarrow}(\mathbf{k}) + 3$, where $\xi_{\downarrow}(\mathbf{k})$ is defined as in Ref. [71].

B.3 On-site interaction term $\mathcal{H}_{\text{os}}$ in momentum space

As in the case of honeycomb-triangular lattice (see Appendix A), we obtain

$$\mathcal{H}_{\text{os}}^{\text{MF}} = -\Delta_0 \sum_{\mathbf{k}} (\tilde{a}_{2\mathbf{q}-\mathbf{k}\downarrow}\tilde{a}_{\mathbf{k}\uparrow} + \text{H.c.}) + \sum_{\mathbf{k}} \frac{\Delta_0^2}{U}. \tag{2.21}$$

With the help of the definition $\tilde{\Psi}_{\mathbf{k}} = \begin{pmatrix} \tilde{a}_{\mathbf{k}\uparrow} & \tilde{a}_{2\mathbf{q}-\mathbf{k},\downarrow}^{\dagger} \end{pmatrix}^{\text{T}}$ made in Eq. (2.18), we obtain

$$\mathcal{H}_{\text{os}}^{\text{MF}} = \Psi_{\mathbf{k}}^{\dagger}\mathbf{H}_{\mathbf{k}}^{(1)}\Psi_{\mathbf{k}} + \sum_{\mathbf{k}} \frac{\Delta_0^2}{U}. \tag{2.22}$$

with

$$\mathbf{H}_{\mathbf{k}}^{(1)} = \begin{pmatrix} 0 & -\Delta_0^* \\ -\Delta_0 & 0 \end{pmatrix}. \tag{2.23}$$

B.4 Nearest-neighbor interaction term $\mathcal{H}_{\text{nn}}$ in momentum space

As in the case of honeycomb-triangular lattice (Appendix A), we obtain

$$\begin{aligned} -V \sum_{\langle m,n \rangle} \langle \hat{h}_{mn} \rangle^* \hat{h}_{mn} \;=\; -\Delta_1 \sum_{\mathbf{k}} \big[& e^{-i\theta}\mathcal{W}_{\mathbf{a}_2}(\mathbf{k}-\mathbf{q}) + e^{-i\phi}\mathcal{W}_{\mathbf{a}_1}(\mathbf{k}-\mathbf{q}) \\ & + e^{-i\varphi}\mathcal{W}_{\mathbf{a}_1-\mathbf{a}_2}(\mathbf{k}-\mathbf{q}) \big] \tilde{a}_{2\mathbf{q}-\mathbf{k}\downarrow}\tilde{a}_{\mathbf{k}\uparrow}. \end{aligned} \tag{2.24}$$

In order to simplify notation, we define a coupling function

$$G_{\mathbf{k},\mathbf{q}} = -\Delta_1 \big[e^{-i\theta}\mathcal{W}_{\mathbf{a}_2}(\mathbf{k}-\mathbf{q}) + e^{-i\phi}\mathcal{W}_{\mathbf{a}_1}(\mathbf{k}-\mathbf{q}) + e^{-i\varphi}\mathcal{W}_{\mathbf{a}_1-\mathbf{a}_2}(\mathbf{k}-\mathbf{q}) \big]. \tag{2.25}$$

By substituting Eq. (2.25) into Eq. (2.24), we obtain

$$-V \sum_{\langle m,n \rangle} \langle \hat{h}_{mn} \rangle^* \hat{h}_{mn} = \sum_{\mathbf{k}} G_{\mathbf{k},\mathbf{q}} \tilde{a}_{2\mathbf{q}-\mathbf{k}\downarrow}\tilde{a}_{\mathbf{k}\uparrow}. \tag{2.26}$$

With the help of Eq. (2.26) we obtain (cf. Appendix A)

$$\mathcal{H}_{\text{nn}}^{\text{MF}} = \sum_{\mathbf{k}} G_{\mathbf{k},\mathbf{q}} \tilde{a}_{2\mathbf{q}-\mathbf{k}\downarrow} \tilde{a}_{\mathbf{k}\uparrow} + \text{H.c.} + \frac{3|\Delta_1|^2}{V}. \tag{2.27}$$

Recalling the definition $\tilde{\Psi}_{\mathbf{k}} = \begin{pmatrix} \tilde{a}_{\mathbf{k}\uparrow} & \tilde{a}^{\dagger}_{2\mathbf{q}-\mathbf{k},\downarrow} \end{pmatrix}^{\text{T}}$ made in Eq. (2.18), we obtain

$$\mathcal{H}_{\text{nn}}^{\text{MF}} = \sum_{\mathbf{k}} \tilde{\Psi}^{\dagger}_{\mathbf{k}} \mathbf{H}^{(2)}_{\mathbf{k}} \tilde{\Psi}_{\mathbf{k}} + \sum_{\mathbf{k}} \frac{3|\Delta_1|^2}{V} \tag{2.28}$$

with

$$\mathbf{H}^{(2)}_{\mathbf{k}} = \begin{pmatrix} 0 & G^{*}_{\mathbf{k},\mathbf{q}} \\ G_{\mathbf{k},\mathbf{q}} & 0 \end{pmatrix}. \tag{2.29}$$

B.5 Full mean-field Hamiltonian in momentum space

The mean-field Hamiltonian without nearest-neighbor interaction term is given by Eqs. (2.19) and (2.22). By using Eq. (2.28) in addition to them, we can write down the mean-field Hamiltonian that includes the nearest-neighbor interaction term. It reads

$$\mathcal{H}^{\text{MF}} = \sum_{\mathbf{k}} \tilde{\Psi}^{\dagger}_{\mathbf{k}} H_{\mathbf{k}} \tilde{\Psi}_{\mathbf{k}} + \frac{3|\Delta_1|^2}{V} + \frac{|\Delta_0|^2}{U} + \lambda^{(2)}_{\mathbf{k}}, \tag{2.30}$$

where

$$H_{\mathbf{k}} = \begin{pmatrix} \lambda^{(1)}_{\mathbf{k}} & -\Delta_0^{*} + G^{*}_{\mathbf{k},\mathbf{q}} \\ -\Delta_0 + G_{\mathbf{k},\mathbf{q}} & -\lambda^{(2)}_{2\mathbf{q}-\mathbf{k}} \end{pmatrix}. \tag{2.31}$$

B.6 Deriving the grand potential $\Omega(\Delta_0, \Delta_1, \mathbf{q})$ and particle numbers $N_\uparrow$ and $N_\downarrow$

B.6.1 Deriving the grand potential $\Omega(\Delta_0, \Delta_1, \mathbf{q})$

Let us say that matrix $\bar{U}$ has the normalized eigenvectors of $H_\mathbf{k}$ as its columns. Subsequently,

$$\bar{U}^\dagger H_\mathbf{k} \bar{U} = \begin{pmatrix} E_1(\mathbf{k}) & 0 \\ 0 & E_2(\mathbf{k}) \end{pmatrix}, \tag{2.32}$$

where $E_1(\mathbf{k})$ and $E_2(\mathbf{k})$ are the eigenvalues of $H_\mathbf{k}$. The quasiparticle operators are

$$\begin{pmatrix} \hat{\gamma}_{1\mathbf{k}} \\ \hat{\gamma}_{2\mathbf{k}} \end{pmatrix} = \bar{U}^\dagger \tilde{\Psi}_\mathbf{k} = \bar{U}^\dagger \begin{pmatrix} \tilde{a}_{\mathbf{k}\uparrow} \\ \tilde{a}^\dagger_{2\mathbf{q}-\mathbf{k}\downarrow} \end{pmatrix}. \tag{2.33}$$

Hence, with a Bogoliubov transformation we obtain

$$\mathcal{H}_{\mathrm{MF}} = \sum_\mathbf{k} \sum_{i=1}^{2} E_i(\mathbf{k}) \hat{\gamma}^\dagger_{i\mathbf{k}} \hat{\gamma}_{i\mathbf{k}} + \frac{3|\Delta_1|^2}{V} + \frac{|\Delta_0|^2}{U} + \lambda^{(2)}_\mathbf{k}. \tag{2.34}$$

Subsequently, we can calculate the grand potential $\Omega = \Omega(\Delta_0, \Delta_1, \mathbf{q})$ by following the discussion on p. 22 of Ref. [105]. It is easy to see that

$$\Omega = \sum_\mathbf{k} \frac{3|\Delta_1|^2}{V} + \frac{|\Delta_0|^2}{U} + \lambda^{(2)}_\mathbf{k} - \frac{1}{\beta} \sum_{i=1}^{2} \ln\left(1 + e^{-\beta E_i(\mathbf{k})}\right). \tag{2.35}$$

At the zero temperature limit

$$\Omega = \sum_\mathbf{k} \lambda^{(2)}_\mathbf{k} + \frac{3|\Delta_1|^2}{V} + \frac{|\Delta_0|^2}{U} + \sum_{i=1}^{2} E_i(\mathbf{k}) \theta\left(-E_i(\mathbf{k})\right), \tag{2.36}$$

where

$$\theta(x) = \begin{cases} 0 & \text{when } x \leq 0 \\ 1 & \text{when } x > 0 \end{cases}. \tag{2.37}$$

B.6.2 Equations for the particle numbers $N_\downarrow$ and $N_\uparrow$

Preliminary results

Let us say that $f(\cdot)$ is the Fermi function with chemical potential $\mu = 0$. That is,

$$f(E) = \frac{1}{e^{E/(k_\mathrm{B}T)} + 1}. \tag{2.38}$$

Direct calculation yields

$$\begin{aligned} 1 - f(E) &= 1 - \frac{1}{e^{E/(k_\mathrm{B}T)} + 1} \\ &= \frac{e^{E/(k_\mathrm{B}T)}}{e^{E/(k_\mathrm{B}T)} + 1} \\ &= \frac{1}{e^{-E/(k_\mathrm{B}T)} + 1} \\ &= f(-E). \end{aligned} \tag{2.39}$$

With the help of Eq. (2.39) we obtain

$$\begin{aligned} \langle \hat{\gamma}_{i\mathbf{k}} \hat{\gamma}_{i\mathbf{k}}^\dagger \rangle &= 1 - \langle \hat{\gamma}_{i\mathbf{k}}^\dagger \hat{\gamma}_{i\mathbf{k}} \rangle \\ &= 1 - f(E_i(\mathbf{k})) \\ &= f(-E_i(\mathbf{k})). \end{aligned} \tag{2.40}$$

Deriving the particle number equations

Multiplying both sides of Eq. (2.33) by $\bar{U}$, we obtain

$$\tilde{a}_{\mathbf{k}\uparrow} = \bar{U}_{11} \hat{\gamma}_{1\mathbf{k}} + \bar{U}_{12} \hat{\gamma}_{2\mathbf{k}}, \tag{2.41}$$

$$\tilde{a}_{2\mathbf{q}-\mathbf{k}\downarrow}^\dagger = \bar{U}_{21} \hat{\gamma}_{1\mathbf{k}} + \bar{U}_{22} \hat{\gamma}_{2\mathbf{k}}. \tag{2.42}$$

Let us next calculate the number of down-spin atoms $N_\downarrow$. With the help of Eq. (2.5) we obtain

$$\begin{aligned} N_\downarrow &= \left\langle \sum_i \hat{a}_{i\downarrow}^\dagger \hat{a}_{i\downarrow} \right\rangle \\ &= \left\langle \sum_{\mathbf{k}} \tilde{a}_{\mathbf{k}\downarrow}^\dagger \tilde{a}_{\mathbf{k}\downarrow} \right\rangle \\ &= \left\langle \sum_{\mathbf{k}} \tilde{a}_{2\mathbf{q}-\mathbf{k}}^\dagger \tilde{a}_{2\mathbf{q}-\mathbf{k}} \right\rangle, \end{aligned} \tag{2.43}$$

where the last equality follows by using periodic boundary conditions. By using Eqs. (2.42) and (2.40), we obtain

$$\begin{aligned} N_\downarrow &= \sum_{\mathbf{k}} |\bar{U}_{21}|^2 \langle \hat{\gamma}_{1\mathbf{k}} \hat{\gamma}_{1\mathbf{k}}^\dagger \rangle + |\bar{U}_{22}|^2 \langle \hat{\gamma}_{2\mathbf{k}} \hat{\gamma}_{2\mathbf{k}}^\dagger \rangle \\ &= \sum_{\mathbf{k}} |\bar{U}_{21}|^2 f\left(-E_1(\mathbf{k})\right) + |\bar{U}_{22}|^2 f\left(-E_2(\mathbf{k})\right). \end{aligned} \tag{2.44}$$

Let us next calculate the number of up-spin atoms $N_\uparrow$. Employing Eq. (2.5), we obtain

$$\begin{aligned} N_\uparrow &= \left\langle \sum_i \hat{a}_{i\uparrow}^\dagger \hat{a}_{i\uparrow} \right\rangle \\ &= \left\langle \sum_{\mathbf{k}} \tilde{a}_{\mathbf{k}\uparrow}^\dagger \tilde{a}_{\mathbf{k}\uparrow} \right\rangle. \end{aligned} \tag{2.45}$$

Using Eq. (2.41), we obtain

$$\begin{aligned} N_\uparrow &= \left\langle \sum_{\mathbf{k}} \tilde{a}_{\mathbf{k}\uparrow}^\dagger \tilde{a}_{\mathbf{k}\uparrow} \right\rangle \\ &= \left\langle \sum_{\mathbf{k}} |\bar{U}_{11}|^2 \hat{\gamma}_{1\mathbf{k}}^\dagger \hat{\gamma}_{1\mathbf{k}} + |\bar{U}_{12}|^2 \hat{\gamma}_{2\mathbf{k}}^\dagger \hat{\gamma}_{2\mathbf{k}} \right\rangle \\ &= \sum_{\mathbf{k}} |\bar{U}_{11}|^2 f(E_1(\mathbf{k})) + |\bar{U}_{12}|^2 f(E_2(\mathbf{k})). \end{aligned} \tag{2.46}$$

Bibliography

[1] D.-H. Kim, J.S.J. Lehikoinen, and P. Törmä. Topological Transitions of Gapless Paired States in Mixed-Geometry Lattices. *Phys. Rev. Lett.*, 110:055301, 2013.

[2] L. E. Ballentine. *Quantum Mechanics: A Modern Development*. World Scientific, 1998.

[3] M. Fierz. Über die relativistische Theorie kräftefreier teilchen mit beliebigem spin. *Helv. Phys. Acta*, 12:3–37, 1939.

[4] W. Pauli. The Connection Between Spin and Statistics. *Phys. Rev.*, 58:716, 1940.

[5] A. Kitaev. Anyons in an exactly solved model and beyond. *Ann. Phys.*, 321:2, 2006.

[6] L.D. Landau and E.M. Lifshitz. *Statistical Physics, 3rd Edition, Part 1*. Elsevier, 1980.

[7] R.H. Swendsen. *An Introduction to Statistical Mechanics and Thermodynamics*. Oxford University Press, 2012.

[8] K. Huang. *Introduction to Statistical Physics*. Taylor & Francis, 2001.

[9] C.J. Pethick and H. Smith. *Bose-Einstein Condensation in Dilute Gases*. Cambridge University Press, 2002.

[10] K. Huang. *Statistical Mechanics*. John Wiley & Sons, 1987.

[11] P. Windpassinger and K. Sengstock. Engineering novel optical lattices. *Rep. Prog. Phys.*, 76:086401, 2013.

[12] P. Barmettler and C. Kollath. Quantum gases in optical lattices. In P. Törmä and K. Sengstock, editors, *Quantum Gas Experiments*, volume 3 of *Cold Atoms*. Imperial College Press, 2014.

[13] M.H. Anderson, J.R. Ensher, M.R. Matthews, C.E. Wieman, and E.A. Cornell. Observation of Bose-Einstein condensation in dilute atomic vapor. *Science*, 269:198–201, 1995.

[14] C.C. Bradley, C.A. Sacket, J.J. Tollet, and R.G. Hulet. Evidence of Bose-Einstein condensation in an atomic gas with attractive interactions. *Phys. Rev. Lett*, 75:1687–1690, 1995.

[15] K.B. Davis, M.O. Mewes, M.R. Andrews, N.J. van Druten, D.S. Durfee, D.M. Kurn, and W. Ketterle. Bose-Einstein condensation in a gas of sodium atoms. *Phys. Rev. Lett*, 75:3969–3973, 1995.

[16] M.R. Andrews, C.G. Townsend, H.-J. Miesner, D.S. Durfee, D.M. Kurn, and W. Ketterle. Observation of Interference Between Two Bose Condensates. *Science*, 275:637–641, 1997.

[17] P. Engels, I. Coddington, P.C. Haljan, V. Schweikhard, and E.A. Cornell. Observation of long-lived vortex aggregates in rapidly rotating Bose-Einstein condensates. *Phys. Rev. Lett*, 90:170405, 2003.

[18] P.C. Haljan, I. Coddington, P. Engels, and E.A. Cornell. Driving Bose-Einstein-Condensate Vorticity with a Rotating Normal Cloud. *Phys. Rev. Lett.*, 87:210403, 2001.

[19] M. Greiner, O. Mandel, T. Esslinger, T.W. Hänsch, and I. Bloch. Quantum phase transition from a superfluid to a Mott insulator in a gas of ultracold atoms. *Nature*, 415:39–44, 2002.

[20] M.P.A. Fisher, P.B. Weichman, G. Grinstein, and D.S. Fisher. Boson localization and the superfluid-insulator transition. *Phys. Rev. B*, 40:546, 1989.

[21] B. DeMarco and D.S. Jin. Onset of Fermi degeneracy in a trapped atomic gas. *Science*, 285:1703–1706, 1999.

[22] A.G. Truscott, K.E. Strecker, W.I. McAlexander, G.B. Partridge, and R.G. Hulet. Observation of Fermi pressure in a gas of trapped atoms. *Science*, 291:2570–2572, 2001.

[23] F. Schreck, L. Khaykovich, K.L. Corwin, G. Ferrari, T. Bourdel, J. Cubizolles, and C. Salomon. Quasipure Bose-Einstein Condensate Immersed in a Fermi sea. *Phys. Rev. Lett.*, 87:080403, 2001.

[24] G. Ferrari, M. Inguscio, W. Jastrzebski, G. Modugno, G. Roati, and A. Simoni. Collisional properties of ultracold K-Rb mixtures. *Phys. Rev. Lett.*, 89:053202, 2002.

[25] C. Ospelkaus, S. Ospelkaus, K. Sengstock, and K. Bongs. Interaction-driven dynamics of ^{40}K-^{87}Rb fermion-boson gas mixtures in the large-particle-number limit. *Phys. Rev. Lett.*, 96:020401, 2006.

[26] K. Góral, L. Santos, and M. Lewenstein. Quantum Phases of Dipolar Bosons in Optical Lattices. *Phys. Rev. Lett.*, 88:170406, 2002.

[27] T. Volz, N. Syassen, D.M. Bauer, E. Hansis, S. Dürr, and G. Rempe. Preparation of a quantum state with one molecule at each site of an optical lattice. *Nature Phys.*, 2:692–695, 2006.

[28] T. Esslinger. Fermi-Hubbard Physics with Atoms in an Optical Lattice. *Annu. Rev. Condens. Matter Phys.*, 1:129–152, 2010.

[29] L. J. LeBlanc and J. H. Thywissen. Species-specific optical lattices. *Phys. Rev. A*, 75:053612, 2007.

[30] G. Lamporesi, J. Catani, G. Barontini, Y. Nishida, M. Inguscio, and F. Minardi. Scattering in Mixed Dimensions with Ultracold Gases. *Phys. Rev. Lett.*, 104:153202, 2010.

[31] P. Soltan-Panahi, J. Struck, P. Hauke, A. Bick, W. Plenkers, G. Meineke, C. Becker, P. Windpassinger, M. Lewenstein, and K. Sengstock. Multi-component quantum gases in spin-dependent hexagonal lattices. *Nature Phys.*, 7:434, 2011.

[32] K.-K. Ni, S. Ospelkaus, M. H. G. de Miranda, A. Pe'er, B. Neyenhuis, J. J. Zirbel, S. Kotochigova, P. S. Julienne, D. S. Jin, and J. Ye. A High Phase-Space-Density Gas of Polar Molecules. *Science*, 322:231–235, 2008.

[33] K.-K. Ni, S. Ospelkaus, D. Wang, G. Quéméner, B. Neyenhuis, M. H. G. de Miranda, J. L. Bohn, J. Ye, and D. S. Jin. Dipolar collisions of polar molecules in the quantum regime. *Nature*, 464:1324–1328, 2010.

[34] B. Yan, S. A. Moses, B. Gadway, J. P. Covey, K. R. A. Hazzard, A. M. Rey, D. S. Jin, and J. Ye. Observation of dipolar spin-exchange interactions with lattice-confined polar molecules. *Nature*, 501:521–525, 2013.

[35] C. Salomon, G.V. Shlyapnikov, and L.F. Cugliandolo. *Many-Body Physics with Ultracold Gases*. Oxford University Press, 2010.

[36] L. He and W. Hofstetter. Supersolid phase of cold fermionic polar molecules in two-dimensional optical lattices. *Phys. Rev. A*, 83:053629, 2011.

[37] A. V. Gorshkov, S. R. Manmana, G. Chen, J. Ye, E. Demler, M. D. Lukin, and A. M. Rey. Tunable Superfluidity and Quantum Magnetism with Ultracold Polar Molecules. *Phys. Rev. Lett.*, 107:115301, 2011.

[38] S. G. Bhongale, L. Mathey, S.-W. Tsai, C. W. Clark, and E. Zhao. Bond Order Solid of Two-Dimensional Dipolar Fermions. *Phys. Rev. Lett.*, 108:145301, 2012.

[39] M. L. Kiesel, C. Platt, and R. Thomale. Unconventional Fermi Surface Instabilities in the Kagome Hubbard Model. *Phys. Rev. Lett.*, 110:126405, 2013.

[40] W.-M. Huang, C.-Y. Lai, C. Shi, and S.-W. Tsai. Unconventional superconducting phases for the two-dimensional extended Hubbard model on a square lattice. *Phys. Rev. B*, 88:054504, 2013.

[41] S. Inouye, J. Goldwin, M.L. Olsen, C. Ticknor, J.L. Bohn, and D.S. Jin. Observation of Heteronuclear Feshbach Resonances in a Mixture of Bosons and Fermions. *Phys. Rev. Lett.*, 93:183201, 2004.

[42] S. Ospelkaus, C. Ospelkaus, L. Humbert, K. Sengstock, and K. Bongs. Tuning of Heteronuclear Interactions in a Degenerate Fermi-Bose Mixture. *Phys. Rev. Lett.*, 97:120403, 2006.

[43] L.-K Lim, A. Lazarides, A. Hemmerich, and C. Morais Smith. Strongly interacting two-dimensional Dirac fermions. *Europhys. Lett.*, 88:36001, 2009.

[44] L.-K Lim, A. Lazarides, A. Hemmerich, and C. Morais Smith. Competing pairing states for ultracold fermions in optical lattices with an artificial staggered magnetic field. *Phys. Rev. A*, 82:013616, 2010.

[45] K.B. Gubbels H.T.C. Stoof and D.B.M Dickerscheid. *Ultracold Quantum Fields*. Springer, 2008.

[46] F.H. Mies, E. Tiesinga, and P.S. Julienne. Manipulation of Feshbach resonances in ultracold atomic collisions using time-dependent magnetic fields. *Phys. Rev. A*, 61:022721, 2000.

[47] T. Köhler and K. Góral. Production of cold molecules via magnetically tunable Feshbach resonances. *Rev. Mod. Phys.*, 78:1311, 2006.

[48] E. Feenberg. *Theory of Quantum Fluids*. Academic Press, 1969.

[49] M. Saarela. Elementary Excitations and Dynamic Structure of Quantum Fluids. In A. Fabrocini, S. Fantoni, and E. Krotscheck, editors, *Introduction to Modern Methods of Quantum Many-Body Theory and Their Applications*, volume 7 of *Series on Advances in Quantum Many-Body Theory*. World Scientific, 2002.

[50] E. A. Cornell and C. E. Wieman. Nobel Lecture: Bose-Einstein condensation in a dilute gas, the first 70 years and some recent experiments. *Rev. Mod. Phys.*, 74:875, 2002.

[51] S. Kokkelmans. Feshbach Resonance in Ultracold Gases. In P. Törmä and K. Sengstock, editors, *Quantum Gas Experiments*, volume 3 of *Cold Atoms*. Imperial College Press, 2014.

[52] G.E. Brown and A.D. Jackson. *The Nucleon-Nucleon Interaction*. North-Holland Pub. Co., 1976.

[53] S.J.J.M.F. Kokkelmans, J.N. Milstein, M.L. Chiofalo, R. Walser, and M.J. Holland. Resonance superfluidity: Renormalization of resonance scattering theory. *Phys. Rev. A*, 65:053617, 2002.

[54] J.N. Milstein. From Cooper Pairs to Molecules: Effective field theories for ultra-cold atomic gases near Feshbach resonances. PhD thesis, University of Colorado, Boulder, 2004.

[55] F. Mazzanti, A. Polls, and A. Fabrocini. Energy and structure of dilute hard- and soft-sphere gases. *Phys. Rev. A*, 67:063615, 2003.

[56] C.C. Chang and C.E. Campbell. Energy and structure of the ground state of liquid ^{4}He. *Phys. Rev. B*, 15:4238, 1977.

[57] E. Krotscheck. Inhomogeneous quantum liquids: Statics, dynamics, and thermodynamics. In J. Navarro and A. Polls, editors, *Microscopic Quantum Many-Body Theories and their Applications*, volume 510 of *Lecture Notes in Physics*, pages 187–250. Springer-Verlag, 1998.

[58] R.P. Feynman. Atomic Theory of the Two-Fluid Model of Liquid Helium. *Phys. Rev*, 94:262, 1954.

[59] N. Levinson. *Kgl. Danske Videnskab Selskab Mat.-fys Medd.*, 25, 1949.

[60] R. Jost and W. Kohn. Construction of a Potential from a Phase Shift. *Phys. Rev.*, 87:977, 1952.

[61] Th. Kirst, K. Amos, L. Berge, M. Coz, and H.V. von Geramb. Nucleon-nucleon potentials from Gel'fand-Levitan and Marchenko inversions. *Phys. Rev. C*, 40:912, 1989.

[62] K. Chadan and P.C. Sabatier. *Inverse Problems in Quantum Scattering Theory*. Springer, 2nd edition, 1989.

[63] S.B. Papp, J.M. Pino, R.J. Wild, S. Ronen, C.E. Wieman, D.S. Jin, and E.A. Cornell. Bragg Spectroscopy of a Strongly Interacting ^{85}Rb Bose-Einstein Condensate. *Phys. Rev. Lett.*, 101:135301, 2008.

[64] A. Polls and F. Mazzanti. Microscopic description of quantum liquids. In A. Fabrocini, S. Fantoni, and E. Krotscheck, editors, *Introduction to Modern Methods of Quantum Many-Body Theory and Their Applications*, volume 7 of *Series on Advances in Quantum Many-Body Theory*. World Scientific, 2002.

[65] E.A. Donley, N.R. Claussen, S.T. Thompson, and C.E. Wieman. Atom–molecule coherence in a Bose–Einstein condensate. *Nature*, 417:529, 2002.

[66] S.J.J.M.F. Kokkelmans and M.J. Holland. Ramsey Fringes in a Bose-Einstein Condensate between Atoms and Molecules. *Phys. Rev. Lett.*, 89:180401, 2002.

[67] M. Jona-Lasinio and L. Pricoupenko. Three Resonant Ultracold Bosons: Off-Resonance Effects. *Phys. Rev. Lett.*, 104:023201, 2010.

[68] K. Góral, T. Köhler, S.A. Gardiner, E. Tiesinga, and P.S. Julienne. Adiabatic association of ultracold molecules via magnetic field tunable interaction. *J. Phys. B*, 37:3457, 2004.

[69] T. Esslinger. Fermi-Hubbard Physics with Atoms in an Optical Lattice. *Annu. Rev. Condens. Matter Phys.*, 1:129–152, 2010.

[70] D. Jaksch, C. Bruder, J.I. Cirac, C.W. Gardiner, and P. Zoller. Cold Bosonic Atoms in Optical Lattices. *Phys. Rev. Lett.*, 81:3108–3112, 1998.

[71] D.-H. Kim, J.S.J. Lehikoinen, and P. Törmä. Supplemental material for Topological Transitions of Gapless Paired States in Mixed-Geometry Lattices. *Phys. Rev. Lett.* 110, 055301, 2013.

[72] G. Baskaran. Resonating-valence-bond contribution to superconductivity in MgB_2. *Phys. Rev. B*, 65:212505, 2002.

[73] L.N. Cooper J. Bardeen and J.R. Schrieffer. Theory of Superconductivity. *Phys. Rev.*, 108:1175, 1957.

[74] J. Kajala. Expansion Dynamics in Fermionic Quantum Gases. PhD thesis, Aalto University, 2011.

[75] P. Fulde and R. A. Ferrell. Superconductivity in a Strong Spin-Exchange Field. *Phys. Rev.*, 135:A550, 1964.

[76] A. I. Larkin and Y. N. Ovchinnikov. Inhomogeneous state of superconductors. *Sov. Phys. JETP*, 20:762, 1965.

[77] H.A. Radovan, N.A. Fortune, T.P. Murphy, S.T. Hannahs, E.C. Palm, S.W. Tozer, and D. Hall. Magnetic enhancement of superconductivity from electron spin domains. *Nature*, 425:51–55, 2003.

[78] A. Bianchi, R. Movshovich, C. Capan, P.G. Pagliuso, and J.L. Sarrao. Possible Fulde-Ferrell-Larkin-Ovchinnikov Superconducting State in $CeCoIn_5$. *Phys. Rev. Lett.*, 91:187004, 2003.

[79] R. Lortz, Y. Wang, A. Demuer, P.H.M. Böttger, B. Bergk, G. Zwicknagl, Y. Nakazawa, and J. Wosnitza. Calorimetric Evidence for a Fulde-Ferrell-Larkin-Ovchinnikov Superconducting State in the Layered Organic Superconductor κ-$(BEDT\text{-}TTF)_2Cu(NCS)_2$. *Phys. Rev. Lett.*, 99:187002, 2007.

[80] S. Yonezawa, S. Kusaba, Y. Maeno, P. Auban-Senzier, C. Pasquier, K. Bechgaard, and D. Jérome. Anomalous In-Plane Anisotropy of the Onset of Superconductivity in $(TMTSF)_2ClO_4$. *Phys. Rev. Lett.*, 100:117002, 2008.

[81] Z. Zheng, M. Gong, X. Zou, C. Zhang, and G. Guo. Route to observable Fulde-Ferrell-Larkin-Ovchinnikov phases in three dimensional spin-orbit coupled degenerate Fermi gases. *Phys. Rev. A*, 87:031602, 2013.

[82] M. Bakhtiari, M. Leskinen, and P. Törmä. Spectral signatures of the Fulde-Ferrell-Larkin-Ovchinnikov order parameter in one-dimensional optical lattices. *Phys. Rev. Lett.*, 101:120404, 2008.

[83] A. Korolyuk, F. Massel, and P. Törmä. Probing the Fulde-Ferrel-Larkin-Ovchinnikov phase by double occupancy modulation spectroscopy. *Phys. Rev. Lett.*, 104:236402, 2010.

[84] Y. Liao, A.S.C. Rittner, T. Paprotta, W. Li, G.B. Partridge, R.G. Hulet, S.K. Baur, and E.J. Mueller. Spin-imbalance in a one-dimensional Fermi gas. *Nature*, 467:567–569, 2010.

[85] J. Kajala, F. Massel, and P. Törmä. Expansion dynamics of the Fulde-Ferrell-Larkin-Ovchinnikov state. *Phys. Rev. A*, 84:041601, 2011.

[86] Z. Zheng, M. Gong, Y. Zhang, X. Zou, C. Zhang, and G. Guo. FFLO Superfluids in 2D Spin-Orbit Coupled Fermi Gases. *Sci. Rep.*, 4:6535, 2014.

[87] M. P. Marder. *Condensed Matter Physics*. Wiley, 2nd edition, 2010.

[88] P.M. Chaikin and T.C. Lubensky. *Principles of Condensed Matter Physics*. Cambridge University Press, 2000.

[89] N.W. Ashcroft and N.D. Mermin. *Solid State Physics*. Saunders College Publishing, 1976.

[90] M. Mecklenburg and B.C. Regan. Spin and the Honeycomb Lattice: Lessons from Graphene. *Phys. Rev. Lett.*, 106:116803, 2011.

[91] S. Kobayashi, N. Tarantino, and M. Ueda. Topological influence and backaction between topological excitations. *Phys. Rev. A*, 89:033603, 2014.

[92] B. van Heck, M. Burrello, A. Yacoby, and A.R. Akhmerov. Topological Blockade and Measurement of Topological Charge. *Phys. Rev. Lett.*, 110:086803, 2013.

[93] X.-L. Qi, E. Witten, and S.-C. Zhang. Axion topological field theory of topological superconductors. *Phys. Rev. B*, 87:134519, 2013.

[94] C. Nayak, S.H. Simon, A. Stern, M. Freedman, and S.D. Sarma. Non-Abelian anyons and topological quantum computation. *Rev. Mod. Phys.*, 80:1083, 2008.

[95] X.-L. Qi and S.-C. Zhang. Topological insulators and superconductors. *Rev. Mod. Phys.*, 83:1057, 2011.

[96] D. J. Thouless, M. Kohmoto, M. P. Nightingale, and M. den Nijs. Quantized Hall Conductance in a Two-Dimensional Periodic Potential. *Phys. Rev. Lett.*, 49:405, 1982.

[97] M. V. Berry. Quantal Phase Factors Accompanying Adiabatic Changes. *Proc. R. Soc. London, Ser. A*, 392:45–57, 1984.

[98] T. Fukui, Y. Hatsugai, and H. Suzuki. Chern numbers in Discretized Brillouin Zone: Efficient Method of Computing (Spin) Hall Conductances. *J. Phys. Soc. Jpn.*, 74:1674–1677, 2005.

[99] B. A. Bernevig and T. L. Hughes. *Topological Insulators and Topological Superconductors*. Princeton University Press, 2013.

[100] F.D.M. Haldane. Model for a Quantum Hall Effect without Landau Levels: Condensed-Matter Realization of the "Parity Anomaly". *Phys. Rev. Lett.*, 61:2015–2018, 1988.

[101] G. Jotzu, M. Messer, R. Desbuquois, M. Lebrat, T. Uehlinger, D. Greif, and T. Esslinger. Experimental realisation of the topological Haldane model with ultracold fermions. *Nature*, 515:237–240, 2014.

[102] E. Anisimovas, F. Gerbier, T. Andrijauskas, and N. Goldman. Design of laser-coupled honeycomb optical lattices supporting Chern insulators. *Phys. Rev. A*, 89:013632, 2014.

[103] R. Nandkishore, L. S. Levitov, and A. V. Chubukov. Chiral superconductivity from repulsive interactions in doped graphene. *Nature Phys.*, 8:158–163, 2012.

[104] F. Schwabl. *Advanced Quantum Mechanics*. Springer, 2005.

[105] J. Lehikoinen. Mean Field Studies of Pairing in Mixed Geometries. MSc thesis, Aalto University, 2012.

[106] P. Törmä and K. Sengstock, editors. *Quantum Gas Experiments - Exploring Many-Body States*, volume 3 of *Cold Atoms*. Imperial College Press, 2014.

[107] D.-L. Deng, S.-T. Wang, and L.-M. Duan. Direct probe of topological order for cold atoms. *Phys. Rev. A*, 90:041601, 2014.

[108] G. E. Volovik. Quantized hall effect in superfluid helium-3 film. *Phys. Lett. A*, 128:277–279, 1988.

[109] M. Sigrist and K. Ueda. Phenomenological theory of unconventional superconductivity. *Rev. Mod. Phys.*, 63:239–311, 1991.

[110] M. Vojta, Y. Zhang, and S. Sachdev. Quantum phase transitions in d-wave superconductors. *Phys. Rev. Lett.*, 85:4940–4943, 2000.

[111] A. M. Black-Schaffer, W. Wu, and K. L. Hur. Chiral d-wave superconductivity on the honeycomb lattice close to the mott state. *arXiv:1407.2914*, page , 2014.

[112] B. Kumar and B. S. Shastry. Superconductivity in CoO_2 layers and the resonating valence bond mean-field theory of the triangular lattice t-J model. *Phys. Rev. B*, 68:104508, 2003.

Aalto-DD 34/2015

ISBN 978-952-60-6121-4 (printed)
ISBN 978-952-60-6122-1 (pdf)
ISSN-L 1799-4934
ISSN 1799-4934 (printed)
ISSN 1799-4942 (pdf)

Aalto University
School of Science
Department of Applied Physics
www.aalto.fi

BUSINESS + ECONOMY

ART + DESIGN + ARCHITECTURE

SCIENCE + TECHNOLOGY

CROSSOVER

DOCTORAL DISSERTATIONS